

Wan Ahmad Kamil, Wan Maryam (2013) The study of THz vertical cavity SASER devices. PhD thesis, University of Nottingham.

**Access from the University of Nottingham repository:**

[http://eprints.nottingham.ac.uk/13374/1/Study\\_of\\_THz\\_vertical\\_cavity\\_SASER\\_devices\\_The\\_sis.pdf](http://eprints.nottingham.ac.uk/13374/1/Study_of_THz_vertical_cavity_SASER_devices_The_sis.pdf)

**Copyright and reuse:**

The Nottingham ePrints service makes this work by researchers of the University of Nottingham available open access under the following conditions.

This article is made available under the University of Nottingham End User licence and may be reused according to the conditions of the licence. For more details see: [http://eprints.nottingham.ac.uk/end\\_user\\_agreement.pdf](http://eprints.nottingham.ac.uk/end_user_agreement.pdf)

**A note on versions:**

The version presented here may differ from the published version or from the version of record. If you wish to cite this item you are advised to consult the publisher's version. Please see the repository url above for details on accessing the published version and note that access may require a subscription.

For more information, please contact [eprints@nottingham.ac.uk](mailto:eprints@nottingham.ac.uk)

# The Study of THz Vertical Cavity SASER Devices

**Wan Maryam Wan Ahmad Kamil, BSc.**

Thesis submitted to the University of Nottingham

for the degree of Doctor of Philosophy

June 2013

## **Abstract**

In this thesis, experimental evidence of sustained phonon oscillations, from an electrically pumped vertical-cavity SASER device, working in the THz frequency domain is presented. Experimental investigation of injection seeding of phonons at a particular frequency, by optical excitation, is also presented.

The experimental evidence of phonon oscillation through SASER action consists of a non-linear increase in the initial rising edge of the ballistically propagating LA phonons signal and an increased directionality of emission, once threshold gain is exceeded. The build-up of phonon oscillation fitted well with the theoretical model, also discussed in this thesis, enabling other attributes of the SASER device such as the gain coefficient, maximum acoustic power and device efficiency to be obtained.

The cavity was investigated by means of pump-probe reflectivity measurements. Good quantitative agreement is obtained for the cavity mode frequencies, compared to the calculated reflectance of the cavity modes. Good quantitative agreement of the phonon scattering losses, within the cavity, was also obtained, when compared with theoretical predictions.

Also provided is experimental evidence of injection seeding in the SASER devices under different conditions. The SASER device yields analogous characteristics to a seeded laser in that it acts as a phonon amplifier, due to SASER action, for the injected modes.

The results contribute not only towards understanding the fundamental principles of achieving SASER oscillations but also towards the possibility of achieving a practical SASER device in the future.

## List of Publications

1. R. Beardsley, A.V. Akimov, B.A. Glavin, W. Maryam, M. Henini, A.J. Kent. *Optical detection of folded mini-zone-edge coherent acoustic modes in a doped GaAs/AlAs superlattice*. Physical Review B, 2010. **82**(4): p. 041302.
2. W. Maryam, A.V. Akimov, R.P. Champion, A.J. Kent. *Dynamics of a vertical-cavity quantum cascade phonon laser (saser)*. (Submitted – Nature Communications)
3. W. Maryam, A.V. Akimov, R. Champion and A.J. Kent. *Dynamics of a SASER oscillator*, July 2012 (Oral presentation at *International Conference on Phonon Scattering in Condensed Matter (PHONONS)*)

# Acknowledgements

My first thanks goes to Tony Kent for his continued support and endless guidance throughout my PhD, especially in writing up this thesis. Special thanks to everyone at Dortmund University, especially Jeorge, for allowing us to use the Raman setup.

I would also like to extend my thanks to Andrey, Ryan, Joe and Tom Foxon for helpful discussions, advice and encouragement throughout completing my PhD.

Thanks to Richard and Mo for growing the samples used throughout this thesis. Thanks also to the School of Physics and Astronomy technical staff, especially Chris and Dave Holt for often providing liquid helium at short notice. To Mike for all my computer problems and, Jas and Dave Taylor for the help and advice with device fabrication.

Finally, thank you to all my friends and family who have supported me through the process of my PhD, especially:

To Anna for her lovely tea in times of stress. To Eric, Lucy, kak Su and kak Hanna for lending your ears during tough times. And to the 'surau and lunch' mates: Thanks for the time and friendship.

To ayah, ummi, Mat, Musa, Fiya, Sarah, Ucop, adik and nenek: Thank you for the endless support from back home. To mummy, Tony, Aron and nanna: Thank you for the support and encouragement especially whilst I'm here in England.

To Aririe, my love, who has always been there; without you I wouldn't have been able to reach my dreams.

And to my adorable little Alfateh: Mama loves you so much!

# Table of Contents

Abstract .....	i
List of Publications.....	ii
Acknowledgements .....	iii
Table of Contents .....	iv
List of Figures:.....	viii
List of Tables .....	xvii
CHAPTER 1 .....	1
1.1 Motivation .....	2
1.2 A Historical View of the SASER .....	4
1.3 SASER in a biased GaAs/AlAs Superlattice.....	15
1.4 Thesis outline .....	18
CHAPTER 2 .....	21
2.1 Cavity Created by SL Bragg Mirrors.....	22
2.1.1 Overlapping of Modes inside the Cavity.....	28
2.2 A “Cold” Cavity .....	29
2.3 The Threshold Condition .....	32
2.4 Scattering and Estimation of Threshold Gain .....	33
2.4.1 Isotope Scattering .....	35
2.4.2 Scattering by Si Donors .....	36
2.4.3 Phonon-Electron Scattering from the Contact Layers ..	36
2.4.4 Phonon-phonon Scattering .....	38

2.4.5	Interface Scattering.....	38
2.4.6	Estimation of Threshold Gain.....	39
2.5	The Cavity Lifetime and Q Factor.....	40
2.6	Build-up of SASER Oscillation.....	41
2.7	Estimation of Initial Intensity.....	44
2.8	Estimation of SASER Output.....	45
2.9	Theoretical behaviour of the phonon intensity build up .....	46
2.10	Conclusion .....	48
CHAPTER 3 .....		49
3.1	Device Structure.....	49
3.1.1	NU 2694.....	50
3.1.2	MN 685 & MN 652 .....	51
3.2	Specific Experimental Apparatus.....	52
3.2.1	Bath Cryostat.....	53
3.2.2	Continuous flow cryostat.....	56
3.2.3	Laser.....	57
3.3	Device Fabrication Procedures .....	58
3.3.1	Photolithography and Wet etching .....	58
3.3.2	Contacts metallisation and Annealing.....	59
3.4	Characterisation Techniques.....	60
3.4.1	Current-Voltage Measurements.....	61
3.4.2	Photoluminescence (PL) Measurements .....	63
3.5	Time-Resolved Pump-Probe Experiment .....	64
3.5.1	Optical Arrangement.....	65
3.5.2	The Electronics.....	67

3.6	Bolometric Detection .....	70
3.6.1	Bolometer fabrication .....	70
3.6.2	Principle of Operation .....	72
3.7	Conclusion.....	76
CHAPTER 4 .....		77
4.1	Optical (electron-hole) resonance of the SLs .....	77
4.2	SASER Cavity Characteristics Determined by Pump – Probe Measurements .....	81
4.2.1	Generation and Detection .....	82
4.2.2	Results and Discussion.....	86
4.2.3	Other Properties of the MN 685 SASER Device .....	93
4.3	The SASER cavity of NU2694.....	95
4.4	Conclusion.....	96
CHAPTER 5 .....		98
5.1	Transport measurement of the devices .....	99
5.2	Bolometric detection of the phonon flux .....	102
5.3	Results from the NU 2694 SASER device.....	105
5.4	Results from the MN 685 SASER Device.....	112
5.5	Evidence and Analysis of the Phonon Build Up.....	116
5.5.1	SASER Gain .....	122
5.5.2	Estimates of the Output Power .....	125
5.5.3	SASER Device Efficiency .....	127
5.6	‘Sidelight fluorescence’.....	129
5.7	Conclusion.....	130



CHAPTER 6 .....	132
6.1 Current-Voltage characteristics under light illumination....	135
6.2 Injection Seeding with Modes of the Cavity – Case Study for the NU 2694 SASER device .....	137
6.2.1 Phonon Generation mechanism .....	137
6.2.2 Results from the NU 2694 device .....	140
6.2.3 Signals Associated with Bolometer Sensitivity .....	147
6.3 Injection Seeding in a Low Q Cavity – Case Study of the MN 685 SASER Device .....	149
6.3.1 Results from the MN 685 device .....	149
6.3.2 The optical (luminescence) and TA phonon power ....	152
6.4 Overall conclusion .....	153
 CHAPTER 7 .....	 155
7.1 Conclusions.....	155
7.1.1 THz SASER Oscillations:.....	156
7.1.2 Injection Seeding.....	156
7.2 Future Work.....	158
7.2.1 SASER Device as a Driving Source for Electromagnetic (EM) Radiation .....	158
7.2.2 Coherent Detection of Acoustic Emission .....	159
7.2.3 Improvements on SASER Gain Medium .....	160
7.2.4 Silicon Based SLs as Potential SASER Devices.....	161
References .....	163

# List of Figures:

Figure 1.1: (a) Experimental setup for the observation of 9.3 GHz phonon amplification using Ruby [8]. The ruby rod was pumped with a 23.3 GHz microwave frequency alongside with an applied magnetic field of 0.37 T applied at an angle 56 degrees to the C-axis of the ruby rod. (b) The energy level diagram of the system under ‘push-pull’ microwave pumping. By pumping at energy of  $\hbar\Omega$ , population inversion is achieved between energy levels 3 and 2, giving rise to the emission of phonons with energy  $\hbar\omega$ ..... 5

Figure 1.2: A representation of the SASER process described in [11], where the  $E(^2E)$  metastable doublet state and the  $^4A_2$  ground quartet of the  $Cr^{3+}$  is split by the application of a magnetic field. The  $E(^2E)$  two-level system is fully inverted by selective pulse optical excitation. .... 6

Figure 1.3: The step increase in spin population at E level for multiple phonon round trip times resembled by the increase provided by the phonon avalanches. This provided evidence of stimulated emission. Figure taken from [12]. .... 8

Figure 1.4: The scheme of operation in the case of observing the motion of a single trapped ion interacting with incoming laser beams tuned above and below resonance, as described in [16]. The optical transition has frequency  $\omega_0$  and linewidth  $\gamma$ ..... 10

Figure 1.5: The two-level pumping diagram for the ‘phonon laser’ action using coupled microtoroids as described in [18]. .... 11

Figure 1.6: The potential profile and energy levels under the conditions for resonant tunnelling for the SASER action described in [21]. .... 13

Figure 1.7: Illustration of the phonon generation process between a pair of GaAs wells under vertical electron transport under a strong electric field. Stimulated phonon emission is achieved when the Stark splitting energy,  $\Delta$ , matches the incident phonon energy as described in [32]. .... 16

*Figure 2.1: Reflectance graph and dispersion curve for a 50 period GaAs/AlAs SL with a period of 10 nm. In this case, the first Bragg reflection occurs around a centre frequency of 260 GHz and the next Bragg reflection occurs at the zone centre frequency of 520 GHz... 27*

*Figure 2.2: The reflectance against the number of periods of a particular SL having the width of the well and barrier 4 nm thick. As the number of periods reaches 20, the reflectance is almost 100 %. ..... 28*

*Figure 2.3: Cavity formed by a pair of acoustic mirrors, where phonons may bounce back and forth inside the cavity as they are reflected by the mirrors. .... 30*

*Figure 2.4: The theoretical model for the build-up of phonon intensity inside a 2  $\mu\text{m}$  SASER cavity device for 620 GHz phonon modes. The build up time for different steady state intensities is compared. .... 47*

*Figure 3.1: Schematic diagram of sample NU 2694. The undoped SLs acts as cavity mirrors while the doped SL situated in the centre of the structure is the gain medium. .... 51*

*Figure 3.2: Schematic representation of sample MN 685. This structure is a regrowth of NU 2694 with slight modifications to the doping profile of the gain medium and the period of the cavity mirror SLs (8 nm). .... 52*

*Figure 3.3: Diagram of the Optistat bath cryostat (taken from OXFORD Research Instrument manual). A temperature as low as 1.5 K was achieved by lowering the pressure in the sample space containing liquid helium using a vacuum pump. .... 54*

*Figure 3.4: The sample holder used for the Optistat cryostat comprised of a copper clad PCB. Gaps between the copper plates were intended to isolate individual electrical circuits. The outermost copper plate was grounded. .... 55*

*Figure 3.5: Diagram of the continuous flow cryostat taken from the Oxford Instruments manual. The heat exchange combined with a heater and a sensor provides accurate control of the temperature using PID feedback algorithm. .... 56*

*Figure 3.6: The devices on the chip before bonding the contacts. The horseshoe-shaped contact was connected to a contact pad on the sample holder with a bond wire, and the grid is bonded to ground. .... 60*

*Figure 3.7: The IV setup to measure the current flowing through the gain medium SL structure for both samples. The device was biased, using a Digital Voltage Source (DVS) and the corresponding voltage drop across the 10  $\Omega$  resistor was measured by the Digital Multi Meter, DMM. .... 61*

*Figure 3.8: Typical IV characteristics of a SL under vertical electron transport, obtained from [33]. As the SL undergoes hopping transport, the current increases linearly with bias until negative differential conductance occur in the structure. .... 62*

*Figure 3.9: Schematic diagram of the PL setup. Near UV light was used to excite the sample (350nm). The light entered a periscope, for appropriate height adjustments, and deflected on a prism before reaching the sample. The luminescence from the sample was collected using a lens and analysed with a CCD spectrometer. .... 63*

*Figure 3.10: Schematic diagram of the experimental setup for pump - probe measurements. .... 66*

*Figure 3.11: Flow chart of the Visual Basic program for experimental control..... 69*

*Figure 3.12: Representation of the bolometer where the sensitive detection region has a length to width ratio of 10:1. The bolometer comes in pairs; however, only one bolometer was needed to be aligned to the active device. .... 72*

*Figure 3.13: Graph representing the superconducting transition for a typical bolometer. The dotted line indicates the bottom of the transition curve which is the ideal temperature for conducting the experiment. The solid black line indicates the position of a second transition, also observed under experimental conditions. .... 74*

*Figure 3.14: The setup for bolometer measurements conducted at around 2 K. Electrical pulses were sent to the active device from a pulse generator and the signal obtained at the bolometer was amplified and recorded using the DPO oscilloscope. A constant (small)*

current was sent to the bolometer by means of a 10 K $\Omega$  resistor inside the preamplifier box. .... 75

Figure 4.1: Photoluminescence from the different SL structures was observed by optically exciting the SL structure(s). For sample NU 2694, the first mirror SL structure was completely removed, by means of chemical etching, to allow direct photo excitation in each SL structure of interest..... 78

Figure 4.2: The process of photoluminescence for a type I SL where the incident photons excite the electrons into the conduction band and the emitted photon luminescence provided a measure of the interband energy gap..... 79

Figure 4.3: The luminescence spectrum for sample NU 2694. The mirror SL had an optical resonance centred at 663 nm whilst the gain medium SL peaked at 758 nm..... 80

Figure 4.4: The optical resonance of sample MN 685, using laser light with a wavelength of 690 nm. The first interband transition for the mirror SL was centred at 718 nm and for the middle SL centred at 759 nm..... 81

Figure 4.5: The folded dispersion curve for LA phonon modes of the mirror SLs in sample MN 685 and MN 652. The  $2k_{laser}$  red line at 594 GHz and 694 GHz, represented by the red circles whilst the blue square corresponded to the zone centre phonon mode at 640 GHz. Brillouin oscillations may also be detected, as marked by the black circle. .... 83

Figure 4.6: The reflectance for the cavity mirrors in MN 685 and MN 652. The zone centre phonon modes reflect 36 % and 90 % for the 15 period and 40 period mirror SL respectively. .... 84

Figure 4.7: Pump-probe technique employed for measuring the characteristics of the SASER cavity. The pump beam was tuned to the optical resonance of the mirror SL structure and a probe beam, with intensity roughly an order of magnitude lower, measures the change in reflectance caused by the phonons generated. .... 85

Figure 4.8: The temporal change in reflectivity measured by the probe pulse. The phonon spectrum related to each box is also presented..... 87

Figure 4.9: (a) Coherent phonon oscillation in a 130 ps time window after the arrival of the pump pulse. Beating effects, observed, may be due to the interaction of the zone centre modes and the  $2k_{laser}$  modes. The strong low frequency oscillations are possibly related to Brillouin oscillations. (b) The high frequency oscillations were detected for the second time from 893 ps, indicating the phonon mode that was able to complete a round trip inside the cavity. .... 88

Figure 4.10: The frequency spectrum of the phonon modes detected by the probe pulse at different time delays for sample MN 652. Peaks at 33 ps delay corresponded to phonons at the zone centre ( $q = 0$ ) and  $2k_{laser}$  whereas only the zone centre phonon mode was present 950 ps later. .... 89

Figure 4.11: Pump - probe reflectivity in a 55 ps window acquired by the DPO oscilloscope, enabling large averaging to provide high signal to noise ratio. .... 91

Figure 4.12: Fourier transform of the change in reflectivity in sample MN 685 at an excitation wavelength of 714 nm. The blue solid line represent the frequency of the phonon modes 33 ps after the arrival of the pump pulse and the dotted red line represent the frequency of the phonon oscillations 950 ps later. The height ratio of the zone centre phonon mode at the two time delays is 0.17. .... 92

Figure 4.13: Reflectance of the mirror SLs in sample NU 2694. The zone edge modes centred at 650 GHz is 97 % reflected by the 15 period SL and near 100 % from the 40 period SL. .... 96

Figure 5.1: IV characteristics for NU 2694 SASER device. Due to the low doping in the SL, the resistance of this device was relatively high (in the k $\Omega$  range). The IV shows characteristics of a typical biased SL. .... 99

Figure 5.2: IV characteristics of the MN 685 SASER device. A linear region from zero, followed by regions of NDC are typical characteristics of a biased SL. .... 101

Figure 5.3: Schematic diagram of the experiment performed on the device for both SASER devices. An electrical pump pulse was sent to the device to provide bias through the gain medium SL. Phonons generated in the gain medium travels through the substrate and the superconducting bolometer provides a response as soon as any phonons arrived. .... 103

Figure 5.4: Clear limiting of the maximum signal was observed for the bolometric response at pump amplitudes above 212 mV, as shown by the circles. The squares represent the bolometric signal for pump amplitude of 189 mV, where the signal is not saturated, for comparison. .... 105

Figure 5.5: Phonon signal obtained from a superconducting Al bolometer directly opposite the NU 2694 SASER where a 300 ns pump pulse, at 316 mV, was applied to the device. The zero time indicated the time at which the electrical bias pulse turned on and the LA phonons were detected 50 ns later (solid arrow), followed by the TA phonons travelling at a slower sound velocity (dashed arrow). The shaded region represents an integrated portion of the bolometer signal across 5 ns. .... 106

Figure 5.6: The normalised phonon power for a range of pump amplitudes for the NU 2694 SASER device. An increase in phonon power was observed at small pump amplitudes due to a capacitive coupling effect and at longer times, a distinct peak was observed at around 345 mV. The height of the peak no longer increases after 185 ns, indicating the phonons has reached steady state intensity for 345 mV pump amplitude. .... 108

Figure 5.7: Representation of the capacitive coupling effect from the contacts as an electrical pulse was applied to the device. Charge builds up in the contact regions at the rising and falling edge of the pump pulse, generating LA and TA phonons as a burst of current flowed through the device. .... 111

Figure 5.8: The bolometer trace taken at 23 dB (corresponding to pump amplitude of 135 mV) shows the LA phonons arriving at zero time followed by the TA phonons 20 ns later. After 300 ns, the bolometer detects the LA and TA phonons for the second time as the pulse ends. .... 112

Figure 5.9: The bolometric responses for several different pulse durations at pump amplitude of 190 mV. The zero time indicates the arrival of the LA phonons followed by the TA phonons 50 ns later, represented by the dotted line. As a much longer pulse was applied, the intensity of the LA phonons kept growing even after the TA phonons arrived. .... 113

Figure 5.10: The normalised LA phonon signal plotted against pump amplitude revealed a pronounced peak centred at 125 mV at steady state intensity. The LA phonons take 120 ns to reach this steady state intensity. .... 115

Figure 5.11: Comparison between the (simulated) accumulations of phonon signal with the actual phonon signal obtained from the bolometer for pump amplitudes of 190 mV and 53 mV respectively. The difference between the two traces, at different pump amplitudes, is attributed to the build up of LA phonons in the cavity, which is clearly observed for the data at 190 mV pump amplitude. .... 116

Figure 5.12: The zero time indicated the arrival of the TA phonons. The blue circles represent the 20 ns data points at pump amplitude of 106 mV whilst the red curve represents the fit. A simulation of the curve for pulse durations of 100 ns and 230 ns were obtained using Equation 5.5 and are represented by the blue and pink dotted lines respectively. The actual data for a 230 ns pulse (also at 167 mV) is shown by the black triangles for comparison. .... 118

Figure 5.13: The time for the signal to reach 90 % of the steady state level across a range of pump amplitudes. The signal accumulates much faster between 90 mV and 170 mV, indicating an increase in phonon population. .... 119

Figure 5.14: Theoretical fit to the rising edge of the bolometer trace for several different pump amplitudes with zero time indicating the arrival of the LA phonons. A good fit was obtained between 200 mV and 106 mV. .... 120

Figure 5.15: The gain profile estimated from the net gain. The gain coefficient is slightly increasing with increasing pump amplitudes and starts to decrease from 170 mV. The average gain coefficient is  $376 \pm 40 \text{ cm}^{-1}$ . Error bars are included but are typically smaller than the size of the data points. .... 122

Figure 5.16: A simulation of the gain profile for the gain medium of the MN 685 SASER device. The gain is plotted against Stark splitting energy,  $\Delta$ , for a fixed phonon energy of,  $\hbar\omega = 1.34 \text{ meV}$  (at frequency of 325 GHz). .... 124



Figure 5.17: Output power of the MN 685 SASER device for a range of pump amplitudes. A broad peak was observed between 119 mV and 186 mV indicating an increase in phonon power. .... 126

Figure 5.18: The efficiency of the MN 685 SASER device as a function of pump amplitude. The maximum efficiency is between 120 mV and 145 mV, as shown by the distinct peak in the graph..... 128

Figure 5.19: The circles represent the normalised phonon power from bolometer 1 when steady state was established whereas the triangles on the other hand represent the normalised phonon power detected by bolometer 2. The dashed line is provided as a guide to the eye. .... 130

Figure 6.1: Schematic diagram of the mode of operation where the laser is used to excite the phonon modes from the high reflector SL. A bolometer was used to detect the LA phonons escaping the cavity as a function of time for all DC biases applied to the device. .... 134

Figure 6.2: The current-voltage (IV) characteristics of the MN 685 SASER device under investigation. There is no critical change to the IV characteristics of the device under illumination by the laser, at wavelength of 750 nm, compared to when in the dark. .... 136

Figure 6.3: Dispersion curve of the 40 period (mirror) SL structure of sample NU 2694. The zone edge gap is between 616 GHz and 686 GHz. The  $2k_{laser}$  intercepts at 1.23 THz and 1.34 THz as indicated by the red crosses..... 138

Figure 6.4: Raman spectrum of NU 2694 at room temperature obtained for two different polarisations of the pump and probe beams where  $z(x,x)z'$  means that the pump and probe beams are parallel to each other and  $z(y,x)z'$  is when the pump and probe beams are perpendicular to each other. Peaks associated to Raman shifts of  $42.73\text{ cm}^{-1}$  and  $46.19\text{ cm}^{-1}$  correspond to the backscattering modes, whereas peaks at  $16.07\text{ cm}^{-1}$  and  $20.51\text{ cm}^{-1}$  correspond to 486 GHz and 620 GHz respectively. .... 139

Figure 6.5: The bolometer signal for excitation wavelength of 720 nm and a dc bias of 400 mV. The zero time indicates the arrival of the direct optical pulse (luminescence) followed by the arrival of the LA and TA phonons as indicated. .... 141

*Figure 6.6: The LA phonon power against the voltage across the device for excitation wavelengths of 720 nm and 750 nm. The device threshold of 200 mV has been removed for clarity. .... 142*

*Figure 6.7: A comparison of the normalised phonon power at steady state (200 ns data) obtained by purely electrically pumping the gain SL, with the LA phonon power obtained when additional cavity modes were seeded into the electrically pumped SASER device (at 720 nm). .... 143*

*Figure 6.8: The threshold gain for the NU 2694 device, on a logarithmic scale, across a range of Stark splitting energies. The red and grey vertical dashed lines represent the Stark splitting energies corresponding to voltages of 140 mV and 165 mV dropped across the gain SL respectively. Based on an estimated value of gain for 620 GHz phonons obtained from [34], represented by the horizontal black dotted line, phonon build up is theoretically possible between 2.49 meV and 2.84 meV. .... 146*

*Figure 6.9: The optical (luminescence) and TA phonon power as a function of voltage dropped across the gain SL. The TA phonon power is following the trend of the optical power and the shape indicates the change in bolometer sensitivity as a function of the bias. .... 148*

*Figure 6.10: The different components of the heat pulse arriving at the bolometer where the zero time indicates the arrival of the optical pulse, followed by the arrival of the LA phonons 81 ns later. The TA phonons then appear at 105 ns after the arrival of the optical pulse. .... 150*

*Figure 6.11: The LA phonon power for five different excitation wavelengths, as indicated by the legends, plotted as a function of the voltage across the SL. Maximum phonon power was obtained for excitation wavelengths of 712 nm and 713 nm, as the power starts to rise from 110 mV and peaks at 155 mV. .... 151*

*Figure 6.12: The optical and TA phonon power obtained as a function of the voltage across the SL. By 160 mV the power for both components fall at the same rate, indicating a change in bolometer sensitivity due to a larger background heat. .... 153*

*Figure 7.1: Experimental scheme of a correlation technique using a p-i-n diode as an optically gated detector. .... 160*

## List of Tables

*Table 4.1: Summary of the parameters of each SASER device, for different operating frequencies. .... 97*

*Table 5.1: Parameters obtained from a theoretical fit to the leading edge of the 230 ns bolometer traces for pump amplitudes between 106 mV and 200 mV. From these parameters, other attributes such as the gain of the gain medium, the output power and the efficiency of the SASER device may be deduced. .... 121*

# CHAPTER 1

## INTRODUCTION

This thesis is mainly concerned about the conditions to sustain oscillations of high frequency phonons inside an acoustic cavity; where the acoustic intensity inside the cavity grows from initial spontaneous emission noise that is amplified by means of stimulated emission, leading to establishing SASER oscillations. The word SASER is an acronym for **S**ound **A**mplification by **S**timulated **E**mission of (acoustic) **R**adiation and is analogous to the function of a laser. As this thesis mainly deals with phonons, a brief, general, discussion regarding the physics of phonons will be presented below before going into the motivation for creating a SASER device and the history of the SASER.

A crystal consists of a periodic arrangement of atoms and molecules that vibrate around the equilibrium point at finite temperatures, due to their thermal motion [1]. Phonons are the quanta of these vibrations having energy of  $\hbar\omega$ , where  $\omega$  is the angular frequency of a normal mode. The normal modes of vibration in the crystal structure are shown in a dispersion curve where, in the limit of  $\lambda \ll a$  where  $a$  is the lattice constant, the wave vector,  $q$ , is directly proportional to  $\omega$ .

This thesis deals with phonons propagating through a superlattice (SL) structure, where alternating layers of materials with different acoustic impedances are stacked on top of each other. As these phonons travel through the SL structure, they are partly reflected and partly transmitted at each interface. The reflectance of a SL structure used in the work described here will be revisited in Chapter 2 with much more detail.

Like photons, phonons are bosons, i.e. elementary particles with integer spin, and they can be created and/or annihilated in collisions with other particles [2]. Anharmonicity or phonon-phonon interactions and electron-phonon interactions, disturb the precise regularity of the lattice, giving rise to either additional phonon losses or increased phonon population depending on the interaction. These interactions will be discussed, individually, in much detail in Section 2.4.

However, in the case of a semiconductor SL, an incoming electron may also deform the lattice structure such that it provides a shift in the semiconductor band edges which couples the electrons and phonons in that particular semiconductor layer. The magnitude of this interaction is defined as the deformation potential in [3] as

$$\delta U(r) = E_1 \Delta(r), \quad (1.1)$$

where  $E_1 \Delta$  represents the shift in the band edges.

The mobility of electrons and holes in the semiconductor are determined by this interaction as well as scattering by impurities or other lattice defects. Therefore, in the concept governing SASER action described in this thesis, the electron–phonon interaction via the deformation potential mechanism, which is the dominant coupling mechanism in the SL structure under investigation, is taken into account when calculating the probabilities of the phonon assisted processes [4].

## 1.1 Motivation

Owing to the physical similarities shared between photons and phonons, i.e. both are bosons, the concept of a SASER or a ‘phonon

laser' has become a growing interest in the phonon physics research community. The primary goal of this work is to determine the feasibility of a practical electrically pumped THz SASER device.

The potential applications of these intense coherent phonons in the THz frequency range are:

- The possibility of non-disruptive probing of embedded nano structures. Two-dimensional images at sub-micron resolution of a buried nano scale pattern have been reported by means of ultrafast acoustic techniques [5]. By probing at THz frequencies, nanometre resolution of these nano structures is possible. As this technique is non-invasive, it would be most beneficial in fields of medical and bio-molecular imaging as well as in characterising embedded nano structures [5].
- A mechanism for converting acoustic phonons to electromagnetic radiation, as recently demonstrated by [6]. A source of an intense acoustic beam such as a SASER device may provide as a driving source for the generation of electromagnetic (EM) radiation. THz frequency EM radiation has been used in applications of molecular and material excitations [7], charge transfer [8], imaging [9], as well as plasma physics [10].
- High demands to create devices working at THz frequencies in recent years have pushed researchers and engineers to finding ways of achieving this. Creating an acoustic analogue of the laser, as proposed in this thesis, in the technologically important THz frequency range would not only provide advances in device engineering, but also aid in understanding fundamental principles within the field of THz acoustics.

The concept of SASER action in SLs, relating to this work, will be discussed in Section 1.3. In the following section, however, a brief review of SASER action in various systems will be presented; providing a background to SASER development.

## 1.2 A Historical View of the SASER

Shortly following the first demonstration of the Ruby laser in 1960 [11], the first observation of sound amplification at 9.3 GHz with a gain coefficient of  $0.12 \text{ cm}^{-1}$  [12, 13] using a four-level pumping system of  $\text{C}_r^{3+}$  in Ruby was reported [14]. The experimental configuration, as described in [12], is shown in Figure 1.1 (a) operating at a temperature of 1.5 K. Also shown is the energy diagram of the system in (b).

A magnetic field was applied at approximately 56 degrees to the rod C-axis to provide appropriate value of the spin splitting energy in  $\text{C}_r^{3+}$ . The transitions of the spins are between the spin-split levels induced by the magnetic field. By optically exciting the ruby rod with energy  $\hbar\Omega$ , as shown in Figure 1.1(b), the spins are promoted from level 4 to level 2 and from level 3 to level 1, with level 1 being the highest energy level. After saturation, level 2 is more populated than level 3 and population inversion is achieved.

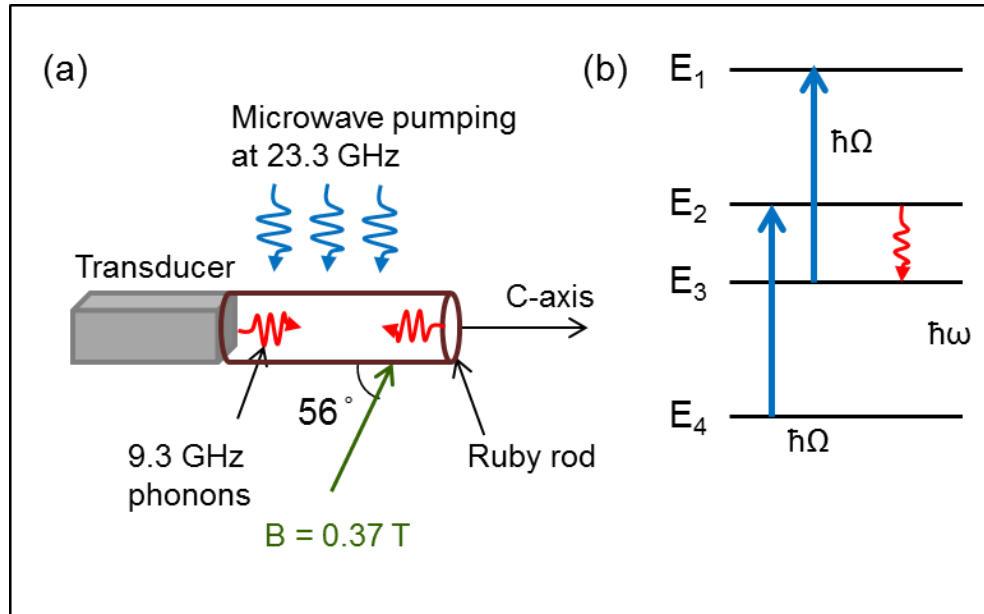


Figure 1.1: (a) Experimental setup for the observation of 9.3 GHz phonon amplification using Ruby [12]. The ruby rod was pumped with a 23.3 GHz microwave frequency alongside with an applied magnetic field of 0.37 T applied at an angle 56 degrees to the C-axis of the ruby rod. (b) The energy level diagram of the system under 'push-pull' microwave pumping. By pumping at energy of  $\hbar\Omega$ , population inversion is achieved between energy levels 3 and 2, giving rise to the emission of phonons with energy  $\hbar\omega$ .

Phonons were generated and measured by a quartz transducer as illustrated in Figure 1.1 (a). As the perturbed system relaxes, phonons with energy  $\hbar\omega$  are emitted via stimulated emission. These phonons, with a frequency of 9.3 GHz, then travel back and forth inside the ruby rod, reflected from its ends.

The author reported a significant decrease in attenuation with each phonon round trip when pumping was applied and a total of 18 echoes were observed. Taking into account the phonon losses from the ruby cavity, continuous SASER oscillation may be possible. However, no experimental evidence of this has been reported to date.



Following on from the first ‘phonon maser’ described above, extended studies of phonon amplification in ruby have been pursued in various ways. For example, in [15, 16] SASER action was observed from the phonon avalanches that are in resonance with the optically inverted Zeeman split  $\bar{E}(^2E)$  doublet of  $\text{Cr}^{3+}$ . Figure 1.2 shows the associated spin energy levels of the system obtained from [15]. This scheme exploits the metastable  $\bar{E}(^2E)$  doublet state whereby the splitting of the states is coupled by a one-phonon transition when an external magnetic field is applied.

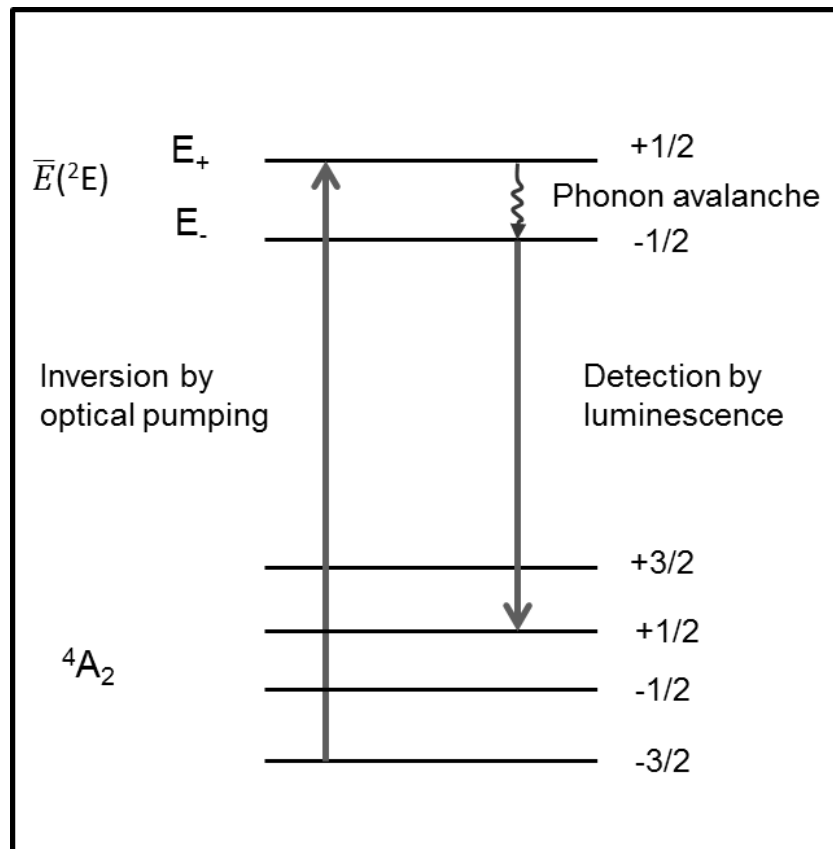


Figure 1.2: A representation of the SASER process described in [15], where the  $\bar{E}(^2E)$  metastable doublet state and the  $^4A_2$  ground quartet of the  $\text{Cr}^{3+}$  is split by the application of a magnetic field. The  $\bar{E}(^2E)$  two-level system is fully inverted by selective pulse optical excitation.

The upper level of  $\bar{E}(^2E)$  may be populated by selective optical pumping of the ruby crystal with a dilute concentration of  $\text{Cr}^{3+}$  to achieve population inversion. By applying 3.48 T of magnetic field at  $60^\circ$  to the c-axis of the ruby rod, the frequency of the transverse phonons generated in the transition is 50.4 GHz. The rate of phonon emission is monitored by the strength of the luminescence associated with the transition from the lower energy state of the doublet to the ground state, as shown by the energy diagram in Figure 1.2.

The authors concluded that stimulated emission was shown by the increased level of phonon avalanches separated by the time it takes for the phonons to complete a round trip of the Ruby rod. This is represented by the observed step population increase in the  $E^-$  level with each phonon pass, as shown in Figure 1.3. However, for this system to work in the THz frequency range, a magnetic field of at least 50 T is required, which is currently unachievable with standard laboratory setups. The cavity is also very large ( $6.60 \times 4.63 \times 1.91 \text{ mm}^3$ ), leading to high phonon attenuation and scattering rates. Therefore, this system is not practical for a THz SASER device.

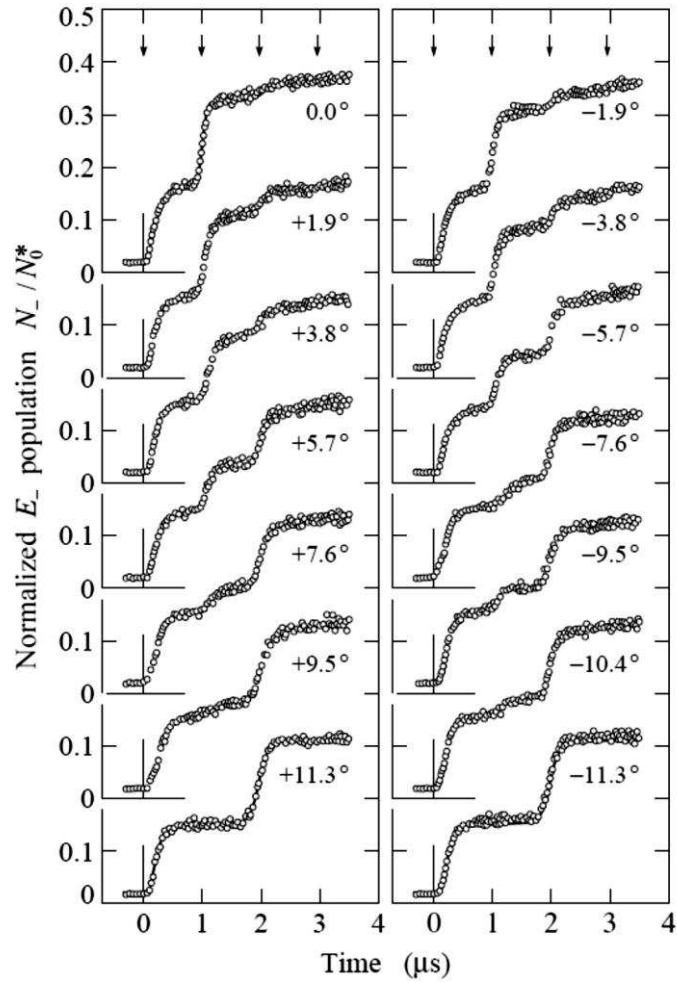


Figure 1.3: The step increase in spin population at E level for multiple phonon round trip times resembled by the increase provided by the phonon avalanches. This provided evidence of stimulated emission. Figure taken from [16].

Evidence of stimulated phonon emission was also reported in different transition metal ion systems. For example, by inversion of a three-level electronic system of diluted  $V^{4+}$  ions in  $Al_2O_3$  as described in [17]. Population inversion in the  ${}^1E_{1/2} - {}^2E_{1/2}$  transition levels in  $V^{4+}$  was achieved by pumping the system with infrared light. The authors noted an increase in the ballistic phonon emission, when pumped above the threshold level for the inversion, with a frequency of 740 GHz detected using a superconducting bolometer. However, the authors were unable to measure and provide further evidence

regarding the forward directionality of the phonon signal. Furthermore, no further investigations of SASER action in this system have been reported so far.

Stimulated phonon emission has also been reported in other systems. For example, in a two-level system (TLS) of a Tetrasil glass rod as discussed in [18]. The authors described the TLS as a fictitious spin  $\frac{1}{2}$  system in a fictitious magnetic field. A comparison was drawn to the approach in [12] where real spins and magnetic fields were used. 340 MHz acoustic pulses were generated using two transducers attached at each end of the glass rod, where from one end the pump pulse was launched and from the other end a probe pulse at minimum intensity. A 'rapid adiabatic passage' technique was employed to achieve the inversion where the frequency of an off-resonance acoustic field was varied through the resonant frequency of the TLS. The 'fictitious' spin precesses around this effective acoustic field, rotating as the frequency is changed and the pseudo-magnetisation was rotated through ' $\pi$ ' radians to invert the population. The samples were kept at below 20 mK in order for the phonon relaxation times become longer than the time needed for the 'adiabatic' pumping.

The authors reported a maximum gain of 2 dB. However, due to the amorphous nature of the glass, high scattering rates and acoustic attenuation in the THz frequency range [19] causes fundamental difficulties in creating THz SASER devices. Also, the cavity is relatively large ( $20 \times 4.5 \times 4.5 \text{ mm}^3$ ) which makes it even harder to observe round trip phonon amplification as the losses due to scattering and phonon attenuation are likely to dominate.

From a different perspective, a possible phonon laser was reported from the observation of a single  $\text{Mg}^+$  ion in a linear radiofrequency trap [20]. The authors observed the interaction of the trapped ion with blue and red shifted laser beams and attributed the results to

phonon amplification due to stimulated emission. Figure 1.4 shows an illustration of the coherent motion of the ion and the physical origin of stimulated emission in this case.

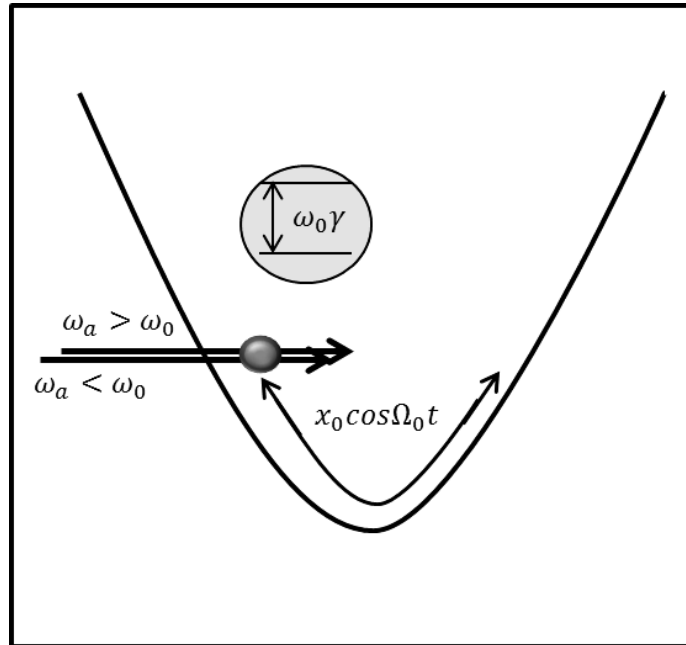


Figure 1.4: The scheme of operation in the case of observing the motion of a single trapped ion interacting with incoming laser beams tuned above and below resonance, as described in [20]. The optical transition has frequency  $\omega_0$  and linewidth  $\gamma$ .

The red shifted laser beam attenuates the ion motion whilst the blue detuned laser beam provided gain by amplifying an existing motion of the trapped ion. Periodic Doppler shifts induced by the ion motion grew, at first, exponentially with time until saturation conditions occurred. Following on from this work, injection locking of optically excited mechanical oscillations in this single trapped ion ‘phonon laser’, was also demonstrated [21]. Possible application in measuring nuclear magnetic moment of single atoms or molecules was also suggested. However, this work involves the cooling of the ion motion; hence, the feasibility of creating an electronically compatible THz SASER device, using this method, is impractical.

‘Phonon laser’ action has also been demonstrated in a compound microcavity system with close analogy to a two-level laser system in producing phonon gain [22]. Two microtoroids, acting as optical resonators, were coupled through an evanescent field. One of them was also coupled to a tapered optical fibre to optically pump the system as well as to monitor the coherent mechanical motion of the system as the laser was scanned through the optical resonances. A schematic of the process is shown in Figure 1.5.

The authors observed phonon amplification between 40 to 400 MHz with a pump threshold of 6  $\mu\text{W}$ . In addition, tuning of the amplified frequency was also possible by adjusting the resonator coupling (the air gap between the resonators). However, efficient detection of the phonons in this work requires the rate of optical damping to be much faster than the rate of the mechanical damping; which may limit the observation of phonon amplification at high frequencies. Furthermore, additional coupling structures are required to link the system to a phonon source.

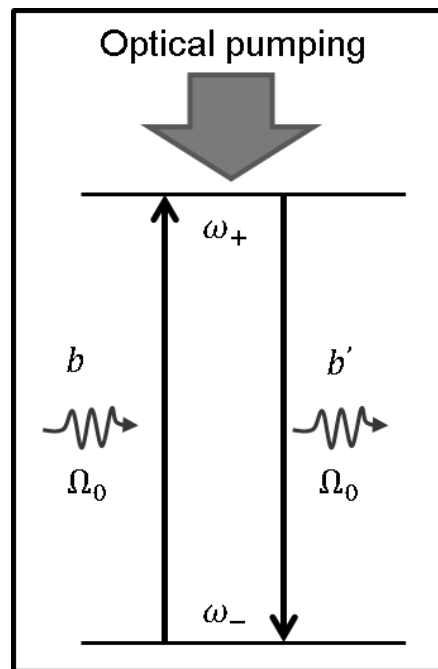


Figure 1.5: The two-level pumping diagram for the ‘phonon laser’ action using coupled microtoroids as described in [22].

So far, all the 'phonon lasers' mentioned above involve optical pumping of the system. Implementing these kinds of SASER devices would require a considerable investment in the laser system and an adequate amount of space to accommodate it. Therefore, producing an electrically driven THz SASER device is much more desirable as it is more versatile, low cost and may easily be incorporated into any modern electronics or devices.

The wavelengths of a few hundred GHz phonon modes in many commonly used semiconductor materials are in the order of tens of nanometres. With advances in high technology growth using Molecular Beam Epitaxy (MBE), introduced in 1975 [23], it is possible to grow high quality thin semiconductor materials leading to the creation of a broad range of low dimensional structures. These structures have been appealing in studying high frequency phonons and provide possibility of creating a practical SASER device in the THz range. Methods of obtaining SASER action in the THz regime with phonons generated by means of electrical excitation are presented below.

One possible method was proposed in [24-26], using a GaAs/AlGaAs double barrier heterostructure, which comprises of a single GaAs well between two AlGaAs barriers, as illustrated in Figure 1.6. The authors predicted acoustic phonon amplification by stimulated emission, via the decay of confined longitudinal optical (LO) phonons into pairs of secondary LO phonons and transverse acoustic (TA) phonons. The structure was designed to have the energy difference between the first excited state level,  $\epsilon_1$ , and the ground state,  $\epsilon_0$ , of the order of the LO phonon energy,  $\hbar\omega$ . An external bias was used to resonantly tunnel the electrons into the conduction band of  $\epsilon_1$  and at a particular bias, when the resonant condition is achieved ( $\Delta\epsilon \approx \hbar\omega$ ); the electrons begin to decay into the

ground state by emitting primary LO phonons before tunnelling out of the structure. The LO phonons then decay into the LO-TA pairs.

By taking into account the electron-phonon and phonon-phonon interactions inside the well alongside with the estimated current flowing through the structure, the authors were able to theoretically estimate the electron and phonon populations in the system. The coherence of the amplified acoustic phonon emission by this device is mentioned by the authors in [27]. However, prior experimental investigations of acoustic phonon decay in GaAs/AlGaAs resonant tunnelling structures have indicated that spatial inhomogeneity of collector carrier concentration dominates in the observed LO phonon decay in [28]. Therefore, to put this theory into practice, experimental issues such as these must be addressed. To date, no experimental evidence of SASER using the proposed theory has been convincingly conveyed.

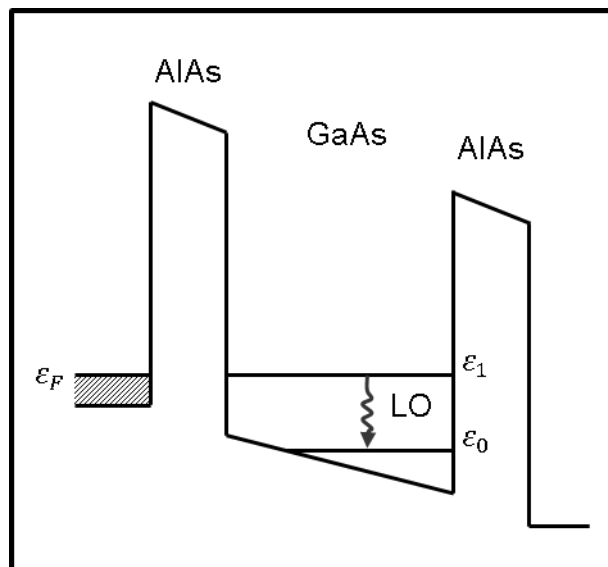


Figure 1.6: The potential profile and energy levels under the conditions for resonant tunnelling for the SASER action described in [25].

Another method of achieving SASER action in the THz and sub-THz regime via phonon emission by electrons drifting at a speed greater



than the speed of sound (analogous to the Cerenkov effect) [29]. Generally, in low dimensional structures, drifting electrons generate both bulk like and confined acoustic phonons. The Cerenkov-like effect then holds for all phonons when the carrier drift velocity exceeds the phonons' velocity. However only confined phonon modes within the structure would manifest strong electron-phonon coupling. Hence, theoretical calculations by the authors revealed phonon amplification to only occur with confined phonon modes despite the dominant density of states of the bulk like modes. The authors described amplification of confined TA phonon modes in various quantum well structures with a prediction of phonon gain between  $100 \text{ cm}^{-1}$  and  $1000 \text{ cm}^{-1}$ . This behaviour has also been postulated in SLs, indicating possibilities of using a SL as a high frequency sound generator [30]. However, no convincing experimental evidenced supporting this claim has been shown to date.

THz phonon amplification in a biased superlattice (SL) was considered theoretically in [31, 32]. The authors described phonon generation in the SL structure under vertical electron transport. The quasi-population inversion is achieved when operating in the Wannier-Stark ladder regime where phonon amplification due stimulated emission occurs when the Stark splitting energy matches the incoming phonon energy ( $\Delta \approx \hbar\omega$ ). The SASER device presented throughout this thesis is based upon this theory. To this effect, a theoretical background of an electrically pumped SASER gain medium made from SLs is discussed in the following section. Also included is a review on recent works pertaining to SASER action observed in this structure.

### 1.3 SASER in a biased GaAs/AIAs Superlattice

A superlattice (SL) consisting of alternating thin semiconductor layers (nominally in the order of few nm thicknesses) of different semiconducting materials, was originally proposed in 1970 [33]. The periodic modulation of the electronic structure gives rise to many interesting effects and has been the centre of attention for many research areas. Thus, SLs are now fairly well understood both in terms of their growth and their electronic properties. The properties of SLs relating to the SASER are the acoustic impedance mismatch at the interface between each layer for phonon propagation [34] and the electronic transport through the structure [35]. The authors in [32] theoretically calculated the possibility of SASER action in a GaAs/AIAs SL using a Wannier–Stark ladder of states where electron conduction occurs via phonon–assisted hopping [35], as illustrated in Figure 1.7.

Two conditions of the electrically biased SL were considered. Firstly, the applied electric field across the SL, with an energy drop of  $\Delta = eFd_{SL}$  ( $F$  being the electric field and  $d_{SL}$  being the period of the SL), considerably exceeds the miniband width of the SL. Here, the electron minibands are ‘broken’ into Wannier-Stark ladder of states, of which are strongly localised in each individual quantum wells (QWs). Secondly, a quasi-population inversion is achieved in the electron subsystem from phonon-assisted indirect electron transitions where the energy shift between the adjacent GaAs wells is equal to  $\Delta$ . As shown in the energy diagram of Figure 1.7, the population of the final electron states is less than that of the initial states when  $\Delta \geq \hbar\omega$ , and population inversion is achieved. Conversely, phonon attenuation occurs when  $\Delta < \hbar\omega$  as the final states have the higher population. The increase of phonon

population, when  $\Delta \geq \hbar\omega$ , creates instability in the phonon subsystem; an analogous effect to photons in lasers.

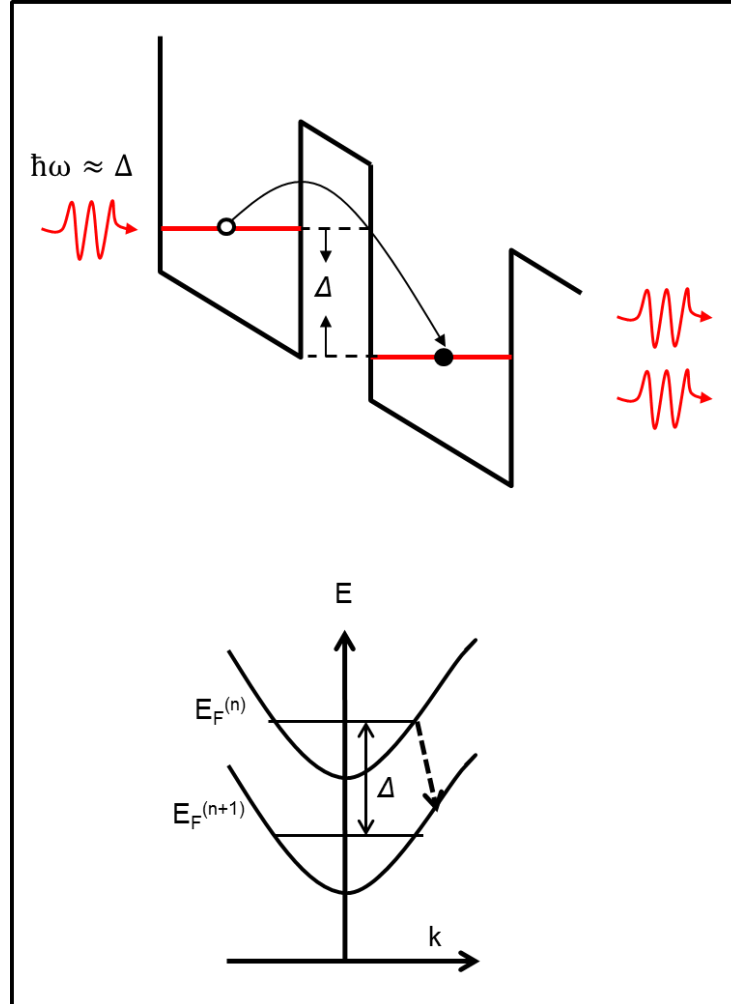


Figure 1.7: Illustration of the phonon generation process between a pair of GaAs wells under vertical electron transport under a strong electric field. Stimulated phonon emission is achieved when the Stark splitting energy,  $\Delta$ , matches the incident phonon energy as described in [36].

The rate of change of phonon population can be written as,

$$\frac{dN_{\omega, q_{\parallel}}}{dt} = P_{\omega, q_{\parallel}}^{(em)} (N_{\omega, q_{\parallel}} + 1) - P_{\omega, q_{\parallel}}^{(ab)} N_{\omega, q_{\parallel}} - \beta_{\omega, q_{\parallel}} N_{\omega, q_{\parallel}}, \quad (1.2)$$

where  $N_{\omega, q_{\parallel}}$  is the number of phonons in the mode,  $P_{\omega, q_{\parallel}}^{(em)}$  and  $P_{\omega, q_{\parallel}}^{(ab)}$  are the probabilities of electron conduction assisted by phonon emission and absorption respectively and  $\beta_{\omega, q_{\parallel}}$  describes the losses due to scattering, decay, etc.

The phonon increment was defined as

$$\gamma_{\omega, q_{\parallel}} = P_{\omega, q_{\parallel}}^{(em)} - P_{\omega, q_{\parallel}}^{(ab)}, \quad (1.3)$$

where  $\gamma$  represents the increment for a phonon mode with frequency  $\omega$  and in-plane wave-vector  $q_{\parallel}$ . The physical significance of Equation 1.3 is that for a given phonon mode, the population may increase with time if the phonon increment is greater than the losses ( $\gamma_{\omega, q_{\parallel}} > \beta_{\omega, q_{\parallel}}$ ). Otherwise the phonon population will simply decay with time.

The phonon increment was analysed further by considering other important parameters such as the electron temperature, the electron concentrations in each QW and the quasi-Fermi energy of the system, with the consideration that only inter-well transitions are taking place. A positive increment, indicating gain, is predicted when  $\hbar\omega < \Delta$  and that the increment increases, as  $q_{\parallel}$  decreases. The energy range for phonon gain, however, falls rapidly with decreasing  $q_{\parallel}$ . Therefore, narrow band phonon amplification is favourable for phonons propagating close to the SL growth axis.

In 2006, experimental observation of high frequency phonon generation in the perpendicular hopping transport regime relating to the above theoretical model was reported [36]. The authors attributed the increase in phonon emission parallel to the SL growth axis to phonon amplification by stimulated emission. The SL itself was also used as a phonon distributed feedback cavity, which

resulted in efficient phonon generation. Recent studies of the SL structure proposed in Ref [36] include observation of coherent amplification and spectral line narrowing [37].

A gain coefficient of  $3600 \text{ cm}^{-1}$  was determined experimentally for 620 GHz phonons making a single pass through the phonon amplifier [38] using the same SL structure as in [37]. By taking into account the phonon mean free path in GaAs, 0.8 mm, as reported by the authors in [39], the threshold condition for SASER oscillation (for 620 GHz phonons) is achievable if  $R_1 R_2 \geq 0.34$ , where  $R_1 R_2$  are the reflectance of the cavity mirrors. Hence, by incorporating this gain medium SL into a low loss ( $<$  gain) acoustic cavity, sustainable oscillations of the amplified phonons, just like the case for photons in a laser medium, is possible. Evidence of efficient phonon micro cavities using SL acoustic Bragg mirrors [40, 41] suggests the potential of a SASER cavity. A thorough discussion into the choice of a practical SASER cavity will be discussed in chapter 2.

Current work involves incorporating a GaAs/AlAs SL gain medium inside an acoustic cavity, and will be discussed throughout the rest of this thesis. This will include a theoretical analysis of the phonon dynamics in such a SASER device, the fabrication processes involved, experimental and characterisation methods employed and the main results obtained.

## 1.4 Thesis outline

The ultimate aims of this thesis are:

1. To present evidence of possible SASER oscillations in a proposed SASER device and discuss the similarities in the

characteristics of the SASER device with the fundamental principles of a typical laser.

2. To show the versatility of the SASER device by investigating the effects of seeding the SASER devices under different conditions. The possibility of tuning the SASER device to amplify at the frequency of the seeded phonons indicates the flexibility of using the device for different frequencies.

This chapter has been dedicated to provide a historical background to the concepts of SASER in different systems and to provide an insight into topics which will be presented in greater detail throughout the rest of this thesis. The theory regarding the gain medium used in this work was also included, alongside highlighting the significance of placing the gain medium within an acoustic cavity. The outline of the remainder of this thesis is as follows.

Chapter 2 provides a description of the theoretical aspects regarding SASER oscillations and the essential elements of a SASER cavity, including the choice of a vital component of the device, the acoustic cavity mirrors, created using semiconductor SLs. A discussion regarding theoretical estimates of the threshold gain, initial (noise) and steady state intensities, as well as the losses experienced by the phonons inside the cavity is also presented.

The next chapter, Chapter 3, initially describes the samples that were used to create the SASER devices. This is followed by a description of the fabrication processes involved in making these devices. The experimental apparatus and techniques are then presented, including the methods used to characterise the devices and how a bolometer was used as a phonon detector.

Chapter 4 is concerned with characteristics of the SASER cavity, especially in determining the round trip time. By observing the Fourier transforms of the intensity of phonons that have completed a round trip, the portion of the phonon intensity that is reflected is compared with the calculated reflectance of the cavity mirrors, as well as taking into account the estimated losses due to scattering events.

Chapter 5 is dedicated to the study of phonon intensity build up, due to SASER action, occurring inside the SASER device. Observation of sustained phonon oscillations inside the cavity, under steady state conditions, is discussed in detail. Further evidence of phonon intensity build up was obtained by fitting the theoretical model, derived in Chapter 2, to the experimental data. Other attributes of the SASER device such as the value of the gain, the output power and the efficiency of the SASER device were also obtained from the fits. A discussion with regards to a reduction of the phonon intensity observed at an angle from the normal incidence of the device axis is also included.

Another characteristic of the SASER device, which is also commonly observed in lasers, is a phenomenon termed injection seeding and is presented in Chapter 6. The results pertaining to seeding phonons, at a fixed frequency, into the SASER device under two different conditions is discussed.

Finally, Chapter 7 summarises all the above observations and recalls the important discussions from previous chapters. Suggestions of potential future work is presented with an emphasis on potential application of the SASER device as a source of electromagnetic radiation as well as suggestions for further work regarding limitations to the current experimental setup.

## **CHAPTER 2**

# **THEORETICAL DESCRIPTION OF THE CAVITY**

Sustainable coherent acoustic oscillations in a THz SASER device have yet to be successfully demonstrated. Analogous to a laser, where coherent light oscillation is achieved by increasing the effective optical path length in a gain medium by placing it in a cavity, SASER oscillation could be made feasible by incorporating an acoustic gain medium inside an acoustic cavity.

In the simplest case, an optical cavity is created by a pair of mirrors, carefully aligned at each end of the laser gain medium so that the photons may bounce back and forth between them with minimal loss. If the net laser amplification exceeds the losses in the system, then coherent optical oscillations will build up in the cavity, eventually reaching a steady state intensity, providing an output beam that is both highly directional and highly monochromatic [42].

The losses, provided by the output coupler or by scattering, are compensated by the gain. Similarly, a practical SASER may be achieved by placing an acoustic gain medium, where the phonon occupation is increased by stimulated emission, inside an acoustic cavity. By making one of the cavity mirrors partially transmitting, a coherent beam of sound may be coupled out of the cavity.

A theoretical background with regards to the SASER gain medium chosen in this work has been presented in Chapter 1. Experimental evidence of phonon amplification, using this gain medium, was also discussed. In this chapter, a fundamental description of the acoustic cavity, including its lifetime and, how the cavity may further enhance



SASER action with the presence of the SASER gain medium is addressed. The conditions for phonon oscillation inside such a cavity are discussed, taking into account the losses that may arise, followed by a theoretical approach for the temporal build-up of SASER oscillation inside the proposed cavity.

## 2.1 Cavity Created by SL Bragg Mirrors

The cavity mirrors, making up the SASER device, must be carefully designed so that they reflect the phonons of interest (where SASER action occurs), and maintain a reasonably small loss so that the gain medium is able to provide enough gain to compensate the losses. Efficient nanocavities formed by SLs acting as Bragg mirrors have been reported in numerous papers [41, 43-45], suggesting SL mirrors are good candidates for a SASER device.

A brief introduction to SLs was presented in Chapter 1. One fundamental property of these SLs is the difference in acoustic impedance between the two semiconductor layers making up the SL. The period of the SL is defined as

$$d_{SL} = d_A + d_B , \quad (2.1)$$

where  $d_A$  and  $d_B$  are the thickness of material A and B respectively. For this work, material A is AlAs and material B is GaAs. As a result of the impedance mismatch at the interface between the two different layers making up the SL, the incident phonon wave will be partially reflected and partially transmitted at the interface. The reflectance at individual interfaces will be small ( $\sim 0.08\%$ ). However, when the reflected waves at each interface are in phase with one another,

Bragg reflection may occur. At normal incidence, the condition for Bragg reflection occurs when

$$m\lambda = 2d_{SL}, \quad (2.2)$$

where  $m$  is an integer and  $\lambda$  is the wavelength of the incident sound. Band gaps at the zone centre and boundary of the folded Brillouin zone open up as a result of Bragg reflection [46]. Therefore, by appropriately choosing the SL period, Bragg reflection may be obtained for the appropriate frequency.

Phonon dispersion for an infinite SL was calculated analytically [47], indicating the frequencies, centred at the stop bands that satisfy the conditions for Bragg reflection. A numerical technique for obtaining the reflectance of the SL Bragg mirrors in a finite SL is by using a transfer matrix technique as described in [34]. Here, the authors considered the phonons travelling from the substrate (will be denoted as S), through N periods of this SL and reaching a detector layer (will be denoted as D).

In each SL layer, the lattice displacement of a given mode,  $U_x$  is

$$U_x(z) = a_x^t e^{ik_x z} + a_x^r e^{-ik_x z} \quad (2.3)$$

where  $a_x$  is the displacement amplitudes for each layer,  $x$  (A or B), with  $r$  and  $t$  representing the reflected and transmitted waves respectively and  $k_x$  is the wave vector ( $= \omega/c_S$ , where  $c_S$  is the sound velocity).

On the other hand, the stress in each layer is

$$S_x = \mu_x \left( \frac{\partial U_x}{\partial z} \right) \quad (2.4)$$

where  $\mu_x$  is the elastic constant for each layer,  $x$  (A or B).

Both stress and displacement fields must satisfy the continuity condition at the interface. For phonon propagation perpendicular to the interface the continuity condition is

$$f_A(z) = f_B(z), \quad (2.5)$$

where  $f_x$  represents the displacement and the stress fields at an interface  $z$  and  $A$  represents the AIAs layer while  $B$  represents the GaAs layer as previously defined.

To calculate the amplitude of the transmitted and reflected waves, it is convenient to express the displacement and stress fields using a  $2 \times 2$  h-matrix where

$$h_x(z) = \begin{bmatrix} e^{ik_x z} & e^{-ik_x z} \\ \mu_x k_x e^{ik_x z} & -\mu_x k_x e^{-ik_x z} \end{bmatrix}. \quad (2.6)$$

The amplitude of the transmitted and reflected wave at an interface is thus

$$\begin{bmatrix} a_{n+1}^r \\ a_{n+1}^t \end{bmatrix} = \begin{bmatrix} e^{ik_x z} & e^{-ik_x z} \\ \mu_x k_x e^{ik_x z} & -\mu_x k_x e^{-ik_x z} \end{bmatrix} \begin{bmatrix} a_n^r \\ a_n^t \end{bmatrix} \quad (2.7)$$

where  $n$  denotes the interface number ordered from  $n = 0$  to  $n = 2N + 1$  ( $2N+1$  interfaces).

Therefore, the continuity condition at the interfaces is

$$h_S(0)w_0 = h_A(0)w_1 \quad (2.8)$$

for the first interface where

$$w_n = \begin{bmatrix} a_n^r \\ a_n^t \end{bmatrix}. \quad (2.9)$$

For the next interface,

$$h_A(d_A)w_1 = h_B(d_A)w_2. \quad (2.10)$$

This is repeated until the phonons reach the detector layer where

$$h_B(ND)w_{2N} = h_D(ND)w_{2N+1}. \quad (2.11)$$

The continuity condition for all interfaces may be summarised as

$$w_D = Tw_S, \quad (2.12)$$

where the substrate phonon wave amplitudes,  $w_S = w_0$ , the detector layer phonon wave amplitudes,  $w_D = w_{2N+1}$ , and T is a transfer matrix, that accounts for the intermediate vectors,  $w_1 - w_{2N}$ , as expressed below:

$$T = [h_D(ND)]^{-1}h_B(ND)[h_B(ND - d_B)]^{-1}h_A(ND - d_B) \dots [h_A(0)]^{-1}h_S(0). \quad (2.13)$$

So Equation 2.12 becomes

$$\begin{bmatrix} 0 \\ a_{2N+1}^t \end{bmatrix} = T \begin{bmatrix} a_0^r \\ 1 \end{bmatrix}. \quad (2.14)$$

The assumption made here is that  $a_{2N+1}^r = 0$  for the detector layer (assuming 100 % transmission to the detector) and  $a_0^t = 1$  for the substrate (assuming 100 % transmission from the substrate).

The transmission rate is defined as the energy ratio of the transmitted phonon flux over the incident phonon flux. Since in this case, the detector and the substrate layer are both GaAs, the transmission rate is just  $|a_{2N+1}^t|^2$ . The transmission rates are calculated numerically and the corresponding reflectance (in percentage) for LA phonons with the appropriate parameters for the structure are obtained. An example of a typical reflectance graph is shown in Figure 2.1.

Bragg reflection is almost 100 % for the first zone centre and first zone edge modes as shown in Figure 2.1, for a 50 period GaAs/AlAs SL. The reflectance peaks at frequencies in the LA stop bands and satisfy the Bragg reflection condition governed by Equation 2.2. Taking into account, the reciprocal SL vector,  $|G_0| = \frac{2\pi}{d_{SL}}$  and the phonon wave vector,  $q = \frac{2\pi}{\lambda}$ , an equivalent of the Bragg condition is

$$2q = mG_0 . \quad (2.15)$$

This means that the LA phonons having  $q = mG_0/2$ , may not travel through the SL and are Bragg reflected. There is also an increase in the number of minor oscillations in the reflectance with increasing period, as seen between the major reflectance peaks in Figure 2.1, which is due to the interference of the transmitted and reflected waves [34]. However, this reflectance is small compared to the Bragg reflection and would not affect the phonons that are Bragg reflected inside the cavity.

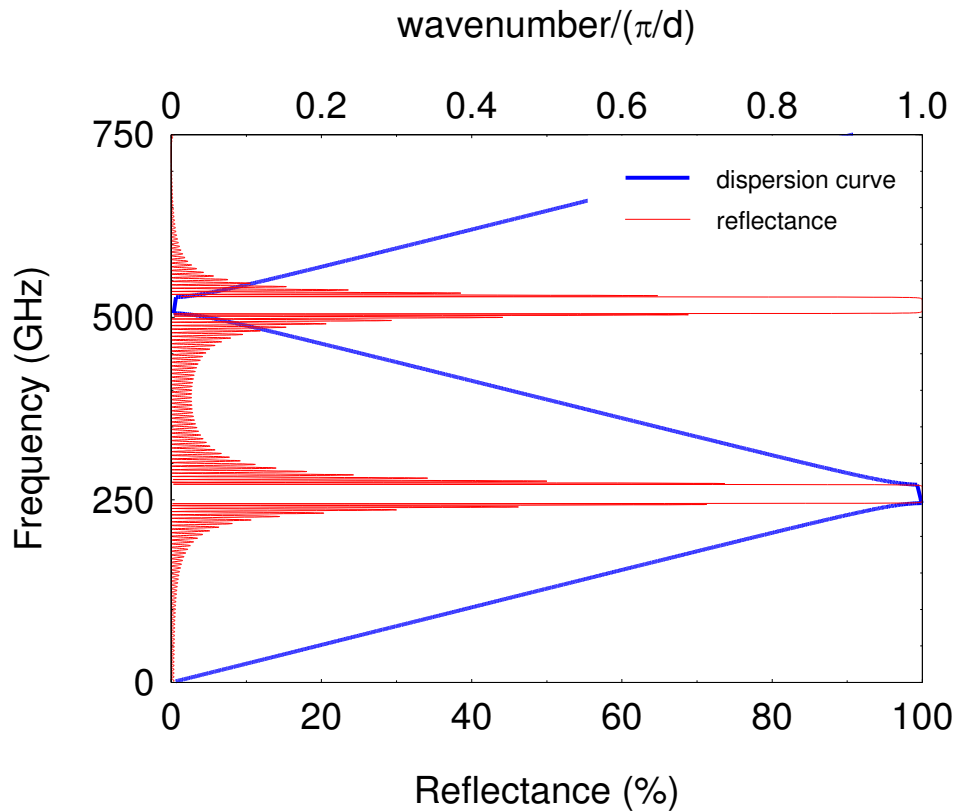


Figure 2.1: Reflectance graph and dispersion curve for a 50 period GaAs/AlAs SL with a period of 10 nm. In this case, the first Bragg reflection occurs around a centre frequency of 260 GHz and the next Bragg reflection occurs at the zone centre frequency of 520 GHz.

As previously discussed, Bragg reflection is achieved in SLs by the reflected waves that add up in phase; implying better reflections with increasing the number of SL periods,  $N$ . Figure 2.2 shows the dependence of the reflection (as a percentage of the incident intensity) to the number of periods for a SL with GaAs and AlAs widths of 4 nm.

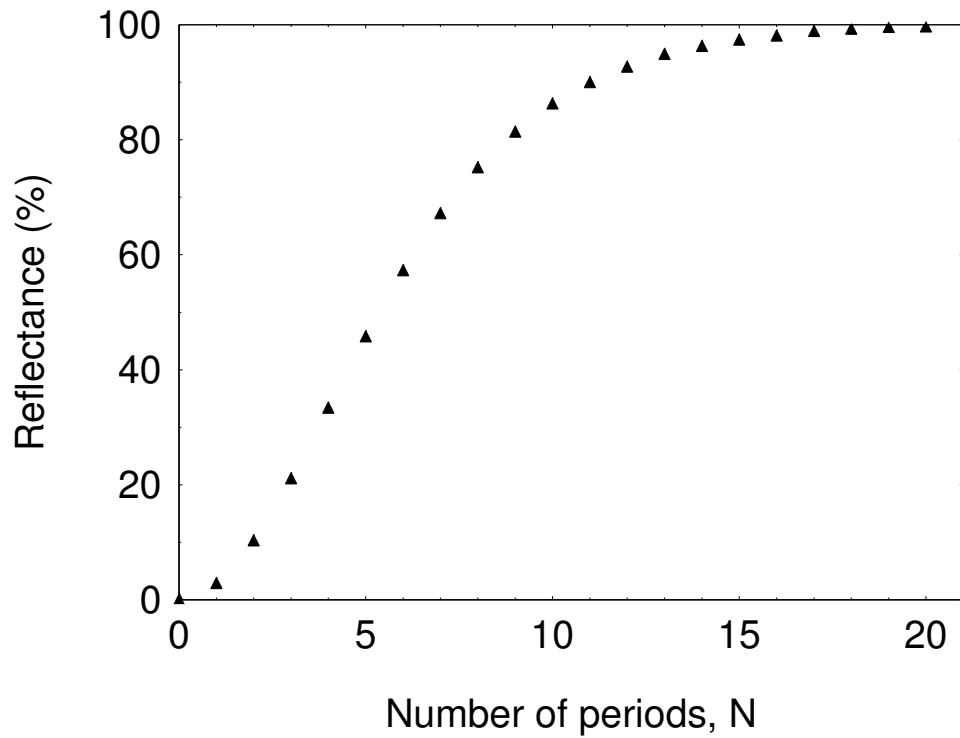


Figure 2.2: The reflectance against the number of periods of a particular SL having the width of the well and barrier 4 nm thick. As the number of periods reaches 20, the reflectance is almost 100 %.

The cavity mirrors may be designed to have nearly 100 % reflection at one end of the cavity and conversely the SL mirror at the other end may be made slightly transmitting by reducing the number of periods. As shown in Figure 2.2, the reflection is almost 100 % by 20 periods. The SASER cavity may be designed to have 15 periods on one end of the mirror SL in order to achieve a reasonable output of 3 % of the phonon intensity inside the cavity.

### 2.1.1 Overlapping of Modes inside the Cavity

The gain medium, as discussed in [37], is formed by a SL. Therefore, just like the cavity mirrors, the gain medium may confine several

modes. Furthermore, the gain medium itself may give distributed feedback oscillations at the frequency of the stop bands [36]. The condition for Bragg reflection depends on the SL period, as indicated by Equation 2.2. Hence, by opting for a mirror SL with different periods to that of the gain medium SL, coherent phonons with frequencies at the stop band for the cavity mirrors may travel through the gain medium as these frequencies are not be confined inside the gain medium SL. Conversely, phonons with frequencies that are confined by the gain medium are not able to be Bragg reflected by the cavity mirrors. Therefore, by having different frequencies for Bragg reflection between the gain medium and the cavity mirrors, phonon oscillations due to the presence of the cavity may be distinguished.

To understand the cavity device that was used throughout the experiments, let's first consider the case where phonons are injected externally into a 'cold' cavity – a cavity without the presence of a gain medium.

## 2.2 A "Cold" Cavity

An acoustic cavity formed by a pair of acoustic mirrors with no gain medium between them is shown in Figure 2.3. Phonons that are injected into the cavity are Bragg reflected by the mirrors and bounce back and forth inside the cavity. In an ideal case, where the phonons experience no losses in the cavity, the phonons would just oscillate inside the cavity indefinitely.



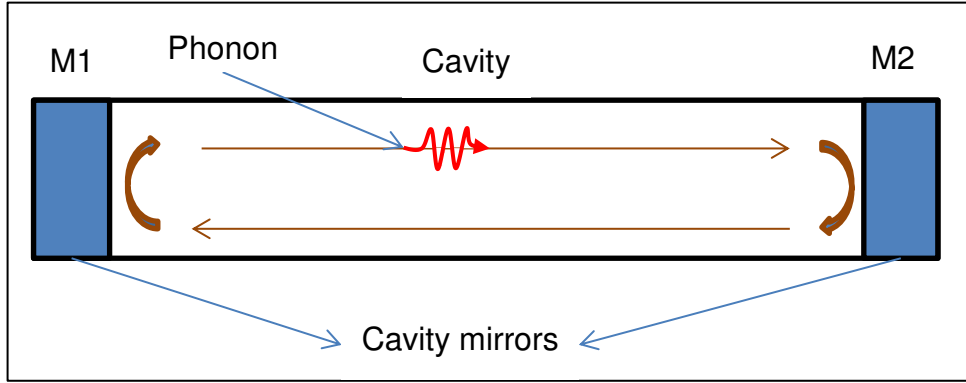


Figure 2.3: Cavity formed by a pair of acoustic mirrors, where phonons may bounce back and forth inside the cavity as they are reflected by the mirrors.

Under steady-state conditions, the amplitude of the right-going wave at the surface of  $M_1$  may be expressed as

$$a_+(0, \omega) = t_1 a_{in}(0, \omega) + r_1 e^{i\varphi_1} a_-(0, \omega), \quad (2.16)$$

where  $a_+(0, \omega)$  are the amplitudes of the right-going beams and  $a_-(0, \omega)$  are the amplitudes of the left-going beams at  $M_1$ ,  $t_1$  is the transmission coefficient of  $M_1$ ,  $a_{in}(0, \omega)$  is the amplitude of the injected phonon beam just outside the cavity and  $r_1 e^{i\varphi_1}$  is the reflection coefficient of  $M_1$  with  $\varphi_1$  as the phase shift upon reflection [48].

The wave then propagates and gets reflected by the cavity mirror,  $M_2$ . The right-going wave will experience a phase shift  $(\delta_{rt} - \varphi_1)$  where  $\delta_{rt}$  is the round trip phase change experienced by the wave – including the phase shifts at the cavity mirrors. The amplitude of the left-going wave may be related to the right-going wave as follows:

$$a_-(0, \omega) = a_+(0, \omega) \times r_2 e^{i(\delta_{rt} - \varphi_1)} \quad (2.17)$$

and Equation 2.16 becomes

$$a_+(0, \omega) = \frac{t_1 a_{in}(0, \omega)}{1 - r_1 r_2 e^{i\delta_{rt}}} \quad (2.18)$$

The intensity is proportional to  $[a_+(0, \omega)]^2$  and hence the ratio of intensities may be written as

$$\frac{I_+(0, \omega)}{I_{in}(0, \omega)} = \frac{T_1}{1 - 2r_1 r_2 e^{i\delta_{rt}} + (r_1 r_2)^2 e^{2i\delta_{rt}}} \quad (2.19)$$

In order to obtain an output from this cavity, just like in a laser cavity, one of the cavity mirrors must be able to partially transmit the phonons. This implies that one of the mirrors would suffer additional loss in the reflectance. Therefore, to maintain phonon oscillations inside the cavity, the phonons must acquire gain to compensate the losses provided by the mirrors, and in a realistic model this should also include any scattering events occurring in the cavity. By placing a gain medium inside the cavity, phonon amplification may be achieved each time the phonons pass through the gain medium. If the gain is high enough to overcome the losses in the cavity, phonons may build up inside the cavity and reach a steady state oscillation intensity.

## 2.3 The Threshold Condition

If phonons are injected into an acoustic cavity containing a medium that provides acoustic gain (a gain medium), then the phonon round trip intensity needs to include the round trip acoustic gain and losses. A modification to Equation 2.17 is then

$$a_-(0, \omega) = a_+(0, \omega) \times r_2 e^{i(\delta_{rt} - \phi_1)} \times e^{\gamma_0(\omega)l_g} e^{-k(\omega)L_s}, \quad (2.20)$$

where  $\gamma_0$  is the small signal gain coefficient,  $l_g$  is the length of the gain medium, and  $e^{-k(\omega)L_s}$  represents the attenuation of the acoustic beam from scattering or other losses in the system where  $k(\omega)$  is the inverse of the scattering length and  $L_s$  is the length of the scattered medium.

The term  $\gamma_0$  is chosen as the small signal gain coefficient, compared to other text books that describe it as the saturated gain coefficient, since close to threshold condition, the gain in the proposed system would be small and the gain medium would need some finite time to reach saturation.

The intensity of the right-going wave is then

$$I_+(0, \omega) = \frac{T_1 I_{in}(0, \omega)}{(1 - r_1 r_2 e^{i\delta_{rt}} e^{\gamma_0(\omega)l_g} e^{-k(\omega)L_s})^2}. \quad (2.21)$$

By introducing a gain medium inside the cavity, phonon oscillation inside the cavity is possible subject to a sufficient phonon population. The threshold condition for these oscillations to occur is achieved by setting the denominator in equation 2.21 to be equal to 0, providing a solution of:

$$R_1 R_2 e^{i2\delta_{rt}} e^{2\gamma_0(\omega)l_g} e^{-2k(\omega)L_s} = 1. \quad (2.22)$$

where  $R_1 (= r_1^2)$  and  $R_2 (= r_2^2)$  are the power reflectance of the mirrors.

This threshold gain condition determines the threshold value of the gain,  $\gamma_{th}$ , that needs to be achieved in the gain medium for the intensity of the oscillation to grow inside the cavity. Taking the real part of equation 2.22 yields the threshold condition for one round trip as:

$$R_1 R_2 \exp[2\gamma^{th}l_g - 2kL_s] = 1. \quad (2.23)$$

The real part of  $e^{i2\delta_{rt}}$  is  $\cos(2\delta_{rt})$ , however, the round trip phase change must be a factor of  $2\pi$  in order to maintain the coherence inside the cavity. Thus  $\cos(2\delta_{rt})$  is 1 and the remaining part of the equation is as described by Equation 2.23.

A direct interpretation of Equation 2.23 is that the gain must balance the losses from the cavity in order for the phonons to oscillate inside the cavity. If  $e^{2kL_s} > e^{2\gamma^{th}l_g}$  then  $R_1 R_2 \exp[2\gamma^{th}l_g - 2kL_s] < 1$ , hence the phonon beam will decay in intensity exponentially with each round trip. On the other hand if the net gain overcomes the losses in the system, then  $R_1 R_2 \exp[2\gamma^{th}l_g - 2kL_s] > 1$  and the beam grows exponentially with each round trip.

## 2.4 Scattering and Estimation of Threshold Gain

In ideal situations, where the cavity is assumed to have no loss, then  $e^{-2kL_s} \sim 1$ , i.e. almost 100 % of the phonons are reflected after completing a round trip. If the phonons inside the cavity incur any scattering events, the phonon intensity would decrease with each round trip as shown in Equation 2.23 where the loss term,  $k$ , is the inverse of the phonon mean free path. By obtaining an estimate of the phonon mean free path (where possible), the significance of the  $e^{-2kL_s}$  term may be deduced.

An estimate of the scattering length may be provided by considering an acoustic cavity incorporated with the gain medium described in [37], consisting of a 50 period GaAs/AlAs SL with a carrier concentration of  $\sim 10^{16} \text{ cm}^{-3}$ . Scattering events occurring inside the biased gain medium has already been accounted for in the theory for acoustic amplification in a GaAs/AlAs SL. However, at each end of the gain medium, there are 0.5  $\mu\text{m}$  thick GaAs contact regions, doped with Si atoms to  $2 \times 10^{18} \text{ cm}^{-3}$ . Here, phonons may scatter from the ionized silicon donor atoms and the free electrons. Undoped GaAs spacers that may be present in the cavity could also give rise to isotope scattering. In addition, interface roughness between each layer of the SL may also be of importance.

At low temperatures, these scattering events may be minimal, and the phonon mean free path, the average distance that phonons may travel ballistically through the material, may be very much larger than the length of the cavity itself. However, a thorough investigation into the phonon scattering processes would confirm whether the loss term,  $k$  is significant. Acoustic gain was observed at a frequency of 620 GHz when the gain medium in [37] was used as a phonon amplifier [38]. Therefore, estimates of the phonon mean free path in this chapter shall be based on this frequency. As scattering generally increases strongly with frequency, at the lower frequencies the scattering will be less than the estimates.

### 2.4.1 Isotope Scattering

At helium temperatures, the longitudinal acoustic (LA) phonon scattering in good quality GaAs is limited by phonons scattering with randomly occurring isotopes in the GaAs layers [49]. The elements of Al and As are isotopically pure [50], therefore it is the mass difference between the  $^{69}\text{Ga}$  and  $^{71}\text{Ga}$  atoms that contributes to the elastic scattering event. Isotope scattering for phonons in GaAs was considered in [51] by considering it as a mass-defect scattering event for the Ga atoms where the scattering rate is calculated as

$$\tau_s^{-1} = A_0 v^4 = \frac{4\pi^3 V_0 g}{c_s^3} \times v^4, \quad (2.24)$$

where  $V_0$  is the unit-cell volume of GaAs ( $= 1.81 \times 10^{-28} \text{ m}^3$  [52]),  $c_s$  is the speed of sound (for LA phonons) in GaAs in the [100] direction ( $= 4730 \text{ ms}^{-1}$  [52]),  $v$  is the frequency of the LA phonon mode and  $g$  is the value of the mass density fluctuation which is defined as

$$g = f \frac{(\bar{M} - M_i)^2}{\bar{M}^2}, \quad (2.25)$$

where  $f$  is the fraction of the isotope in the GaAs layer,  $\bar{M}$  is the average mass of the Ga atoms in the crystal and  $M_i$  is the mass of the isotope atom.

The relative abundances of the  $^{69}\text{Ga}$  and  $^{71}\text{Ga}$  atoms are 0.601 and 0.399 respectively [50], providing an average mass,  $\bar{M}$ , to be 69.8 amu, therefore,  $g = 1.187 \times 10^{-4}$ . The isotope scattering rate, as expressed in Equation 2.24 for LA phonons at 620 GHz, is  $\tau_s^{-1} = 3.72$

$\times 10^6 \text{ s}^{-1}$ . Hence the mean free path for isotope scattering,  $l_i = c_s/\tau_s^{-1}$ , is 1.27 mm which is large, in comparison to the typical cavity length of a few  $\mu\text{m}$ .

### 2.4.2 Scattering by Si Donors

The phonons may also scatter off the ionized impurity Si donors that are introduced in the GaAs contact layers. This situation may also be treated as mass defect scattering, where the mass defect is taken into account by the value of the mass density fluctuation,  $g$  as expressed in Equation 2.25.

There is one Ga atom per unit cell leading to a concentration of  $5.54 \times 10^{21} \text{ cm}^{-3}$ . The fraction of Si replacing the Ga atoms is  $3.61 \times 10^{-4}$  for a doping concentration of  $2 \times 10^{18} \text{ cm}^{-3}$ . The mass of Si is 28.09 amu; hence, using Equation 2.25,  $g = 1.29 \times 10^{-4}$ . Using the same parameters for the speed of sound and unit cell volume, the scattering rate is  $\tau_{Si}^{-1} = 4.06 \times 10^6 \text{ s}^{-1}$ . This corresponds to a scattering length,  $l_{Si} = 1.16 \text{ mm}$ , which is also very much larger than the typical cavity length.

### 2.4.3 Phonon-Electron Scattering from the Contact Layers

By doping the GaAs contact layers with Si, free carriers are introduced in the contact layers which could give rise to an elastic scattering event with the available electrons. The phonon-electron

scattering rate for LA phonons may be calculated as described by [53-55]

$$\tau_{EP}^{-1} = \frac{m^{*3} \Xi^2 c_S}{4\pi \hbar^4 \rho} \left\{ \frac{k_B T}{\frac{1}{2} m^* c_S^2} \right\} \left\{ \frac{\hbar \omega}{k_B T} \right. \\ \left. - \ln \frac{1 + \exp \left[ \frac{\left( \frac{1}{2} m^* c_S^2 - E_F \right)}{k_B T} + \frac{\hbar^2 \omega^2}{8 m^* c_S^2 k_B T} + \hbar \omega / 2 k_B T \right]}{1 + \exp \left[ \frac{\left( \frac{1}{2} m^* c_S^2 - E_F \right)}{k_B T} + \frac{\hbar^2 \omega^2}{8 m^* c_S^2 k_B T} - \hbar \omega / 2 k_B T \right]} \right\}, \quad (2.26)$$

where  $\Xi$  is the deformation potential for GaAs ( = - 8.8 eV [56]),  $E_F$  is the electron Fermi energy,  $k_B$  is the Boltzmann constant,  $T$  is the temperature,  $\hbar$  is the Planck's constant,  $\rho$  is the mass density ( = 5.32 g cm<sup>-3</sup> for GaAs [52] ),  $c_S$  is the sound velocity as previously defined and  $m^*$  is the effective mass of an electron.

The Fermi energy is given by

$$E_F = \frac{\hbar^2}{2m^*} (3\pi^2 n)^{2/3}. \quad (2.27)$$

The Fermi energy of the carriers in this case is  $E_F = 1.38 \times 10^{-20}$  J. However, as  $E_F \gg \frac{1}{2} m^* c_S^2$ , Equation 2.26 becomes

$$\tau_{EP}^{-1} = \frac{m^{*2} \Xi^2 f}{\hbar^3 \rho c}. \quad (2.28)$$

By using the appropriate values for GaAs, the scattering time for phonon-electron scattering is calculated to be 6.43 ns. The



corresponding scattering length is then 30.4  $\mu\text{m}$ , which is only 10 times the typical cavity length.

#### 2.4.4 Phonon-phonon Scattering

At low temperatures the Umklapp process is no longer applicable [57], however, phonon–phonon scattering may still occur in anharmonic materials, such as GaAs. The simplest anharmonicity process is the spontaneous decay of the LA phonons into two transverse phonons of lower frequency [49]. In the low frequency limit, the decay rate described in [58, 59] has a frequency dependence of

$$\tau_{pp}^{-1} = \beta\omega^5 \quad (2.29)$$

The spontaneous decay rate of the LA phonons in GaAs, using the isotropic model, is of the order of  $10^6 \text{ s}^{-1}$  for 1 THz phonons [60]. Therefore, for 620 GHz phonons, the decay rate is greatly reduced, by a factor of  $(1.6)^5$ . The mean free path for phonon-phonon scattering at this frequency is then 49.6 mm. So this scattering event can be safely ignored.

#### 2.4.5 Interface Scattering

The multiple layers inside the cavity, grown by MBE may be subject to interface roughness even under the best growth conditions [61, 62]. This roughness at the interface may provide a means for the phonons of interest to scatter off these interfaces. Numerous studies on acoustic nanocavities created using SL Bragg mirrors have reported a broadening of the spectral width due to interface roughness, however, the phonon modes that were confined in the

cavity remain unchanged [45, 63]. The roughness was estimated to be around 1 monolayer (0.28 nm) of either the GaAs or AlAs layer [45, 64]. The gain medium has well widths of 6 nm, providing an estimated roughness of 4.7 % of the well width. Therefore, the confined phonon modes may scatter slightly giving rise to a spectral line broadening.

#### 2.4.6 Estimation of Threshold Gain

Taking into account the losses by scattering events, an appropriate estimate of the value of threshold gain, in order for phonon oscillations to occur inside the cavity, may now be obtained. Calculations with regard to the actual cavities used throughout this thesis will be presented in chapter 4, but as an example, phonon losses from the 620 GHz in a cavity of 2  $\mu\text{m}$  long (a rough estimate taking into account the length of the gain medium and contacts) may be considered.

For one round trip (1  $\mu\text{m}$  thick of contacts region each way), scattering with isotopes, Si atoms and phonons contributes to less than 1 %. For phonon–electron scattering, however, the fraction of the phonons propagating through the structure in one round trip is  $e^{-2kL_s} = e^{-2(\frac{2}{30.4})} = 0.88$ . Therefore, phonon–electron scattering is the dominant scattering mechanism, providing an additional 12 % to the total loss in the cavity device. Rearranging equation 2.23, and equating the gain as a function of the cavity length, L, an estimate of the threshold gain for one round trip is

$$\gamma_{th} = \frac{\ln\left(\frac{1}{R_1 R_2 e^{-2kL_s}}\right)}{2L} \quad (2.30)$$

If the product of the reflection coefficient is chosen to be 0.97 (if one mirror was chosen to be 3 % transmitting as explained in section 2.1), then in a gain medium of 2  $\mu\text{m}$  long an estimate of the threshold gain is,  $\gamma^{th} = 369 \text{ cm}^{-1}$ . The authors in [38] estimated experimentally the gain coefficient,  $g(\nu) = 3600 \text{ cm}^{-1}$  for a single pass of the 620 GHz phonon modes, which is well above the estimated threshold value obtained above. Therefore, the cavity proposed here would be suitable for the stimulated LA phonons to grow in intensity using the gain medium proposed in [37, 38].

## 2.5 The Cavity Lifetime and Q Factor

There are several ways of measuring the quality of a cavity. For a laser cavity, it is common to calculate the finesse of a cavity in conjunction with the dimensionless quality factor (Q-factor), and the cavity lifetime [48, 65]. Two typical parameters will be considered in this work; one being the quality factor, Q, and another, the cavity lifetime,  $\tau_{cav}$ .

The lifetime of a cavity is an important factor particularly when observing the dynamics of the cavity, implying how long the cavity is able to sustain the oscillations without the presence of a gain medium. Ignoring losses other than through the output coupler, the cavity lifetime may be calculated as

$$\tau_{cav} = m \times \tau = \frac{-1}{\ln(R_1 R_2)} \times \frac{(\text{round trip length})}{c_s} \quad (2.31)$$

where m is the number of round trips for the phonon intensity to fall to  $1/e$  if it is not restored by gain and  $\tau$  is the cavity round trip time.

The Q-factor may be estimated by the ratio of the frequency to the cavity linewidth. Since  $R_1 \approx R_2 \approx 1$ , the cavity linewidth,  $\Delta\nu$  may be deduced as follows [48]

$$\Delta\nu = \frac{1}{\tau_{cav}} \quad (2.32)$$

A large Q factor indicates a good quality cavity, such that the threshold will be low. The Q-factor and cavity lifetime corresponding to each SASER device studied in this work will be calculated and discussed in Chapter 4.

## 2.6 Build-up of SASER Oscillation

When the gain exceeds the threshold value, cavity phonon modes will be able to build up in intensity until they deplete the population inversion and oscillate at a steady state intensity. The gain would then fall as it gets saturated by the phonons. In general, the gain may be expressed as

$$\gamma = \gamma_0 - \gamma_1 I - \gamma_2 I^2 \dots \quad (2.33)$$

The change in the intensity of phonons propagating through an element of the gain medium, of length  $dz$ , with an initial intensity  $I(z)$  may be expressed as

$$dI(z) = I(z + dz) - I(z) = \gamma I(z) dz . \quad (2.34)$$

The time it takes to travel a distance of  $dz$  is  $dt = dz/c_s$  and considering only up to the first non-linear term in Equation 2.33, Equation 2.34 may be written in terms of time as

$$\frac{dI(t)}{\gamma_0 I(t) - \gamma_1 I^2(t)} = v dt. \quad (2.35)$$

Integrating Equation 2.35 and equating  $I(t = 0) = I_0$ , the intensity as a function of time is

$$I(t) = \frac{\gamma_0}{\gamma_1 + \left(\frac{\gamma_0 - \gamma_1 I_0}{I_0}\right) e^{-\gamma_0 ct}}. \quad (2.36)$$

As  $t$  approaches infinity, the phonon intensity reaches steady state intensity, where

$$I_{SS} = \frac{\gamma_0}{\gamma_1}. \quad (2.37)$$

Rewriting Equation 2.36 in terms of the steady state and initial intensity yields

$$I(t) = \frac{I_{SS} I_0}{I_0 + (I_{SS} - I_0) e^{-\gamma_0 ct}}. \quad (2.38)$$

The equation thus far has not included the losses in the system. The loss coefficient,  $\beta$ , may be defined as

$$dI(t) = -\beta I(t) c dt. \quad (2.39)$$

The phonon intensity for each round trip, including all the losses occurring inside the cavity, is

$$I(t) = I_0 R_1 R_2 e^{-2kL_s}. \quad (2.40)$$

By integrating Equation 2.39 and substituting for  $I(t)$  from Equation 2.40, the loss coefficient may be expressed as

$$\beta = -\frac{1}{\tau c} \ln(R_1 R_2 e^{-2kL_s}), \quad (2.41)$$

where  $\tau$  is the cavity round trip time (which is equal to  $2L / c_s$ , where  $L$  is the length of the cavity). The loss term,  $\beta$ , is identical to the threshold gain,  $\gamma_{th}$ , as expected.

Equation 2.38 would now be

$$I(t) = \frac{I_{SS} I_0}{I_0 + (I_{SS} - I_0) e^{-\gamma c t}}, \quad (2.42)$$

where  $\gamma$  is the net gain and  $I_{SS}$  is the steady state intensity. Equation 2.42 implies that the phonon intensity will only grow with each round trip if the net gain is positive, defining the condition for SASER oscillations.

The net gain will only be greater than zero if the small signal gain of the gain medium,  $\gamma_0$ , exceeds the threshold gain, since

$$\gamma = \gamma_0 - \gamma_{th} = \gamma_0 - \frac{\ln(R_1 R_2 e^{-2kL_s})}{2L}. \quad (2.43)$$

Only the linear part of the gain is corrected with the loss coefficient as all losses are assumed to be linear.

## 2.7 Estimation of Initial Intensity

SASER oscillation will start to build up inside the cavity when the stimulated emission rate becomes equal to the spontaneous rate. The initial intensity at which this occurs,  $I_0$ , corresponding to one phonon per mode, may be estimated theoretically by relating it to the thermal population at a temperature of  $\sim 2\text{K}$  (temperature where experiments were conducted).

The density of states,  $D(\nu)$ , for the phonon population per unit volume per unit frequency is

$$D(\nu) = \frac{2\nu^2}{\pi c_S^3}, \quad (2.44)$$

where  $\nu$  is the phonon frequency. The number of these phonons propagating in the z-direction (direction of growth) is  $1/3 D(\nu)$  and the number of phonons crossing a unit area in a second is  $D(\nu) \times c_S$ . Each phonon carries an energy of  $h\nu$ , therefore,  $I_0$  is

$$I_0 = \frac{2\nu^2}{3\pi c_S^2} h\nu p \Delta\nu, \quad (2.45)$$

where  $p$  is the number of longitudinal cavity modes that are confined and  $\Delta\nu$  is the line width of a single cavity mode (Equation 2.32). The frequency spacing between the LA modes inside the cavity is  $c_S/2L$ , where the length of the cavity is  $L$ .

A theoretical estimate of  $I_0$  will be presented in chapter 4, using the parameters for the actual SASER device investigated. However, as an example for the 620 GHz phonons in a 2  $\mu\text{m}$  long cavity, a rough estimate of  $I_0$  may be obtained by considering the following values for the parameters in Equation 2.45: cavity mode frequency spacing of 1.25 GHz and if the reflectance occurs across a 20 GHz frequency range, then the number of modes in the reflectance band are 16. Line width for 620 GHz phonon modes 38 MHz and the average speed of sound propagating through the structure is 5000  $\text{ms}^{-1}$ . The value of  $I_0$  in this case is 814  $\text{Wm}^{-2}$ .

## 2.8 Estimation of SASER Output

As the coherent phonons build up in intensity with each round trip, the gain will eventually saturate and a maximum constant intensity in the cavity is established, which depends on the pumping rate. This steady state intensity is defined as  $I_{SS}$  in Equation 2.42.

The SASER output,  $P_{output}$ , after phonon build up is established, is the fraction of steady state intensity,  $I_{SS}$ , transmitted from the partially transmitting cavity mirror:

$$P_{output} = I_{SS} \times T_M \times \text{Area of device} , \quad (2.46)$$

where  $T_M$  is the transmittance of the cavity mirror providing the output. Furthermore, it is also possible to attain the efficiency of the device by the ratio of the output power and the applied power of the device.



A theoretical prediction of the steady state intensity may be obtained by considering the number of phonons passing through the gain medium. If the gain medium is assumed to be 100 % efficient, then every “hop” between adjacent wells is by stimulated emission and the maximum number of “hops” possible for an applied current per second through the 50 period gain medium SL is

$$n_{hops} = \frac{50JA}{e}, \quad (2.47)$$

where  $J$  is the current density (current per unit area of the device),  $A$  is the area of the device and  $e$  is the elementary charge. Each phonon carries energy of  $h\nu$ , so the maximum possible steady state intensity is

$$I_{SS} = \frac{50Jh\nu}{e}. \quad (2.48)$$

For example, if 10 mA of current is going through a 400  $\mu\text{m}$  diameter device, then an estimate for the maximum steady state intensity at this current is 5000  $\text{Wm}^{-2}$ .

## 2.9 Theoretical behaviour of the phonon intensity build up

By using an estimate for the  $I_0$  and  $I_{SS}$  values, as provided above for a current of 10 mA, it is possible to predict the possible outcome of the phonon intensity build up in the proposed SASER device using Equation 2.42. The frequency of the SASER oscillations is taken to be 620 GHz, as used in calculating the scattering losses and

threshold gain previously. The small signal gain,  $\gamma_0$ , may be estimated as  $3600 \text{ cm}^{-1}$  as described in [38], providing a value for the net gain,  $\gamma$ , as  $3231 \text{ cm}^{-1}$ . The estimated values of the initial and steady state intensities are  $814 \text{ Wm}^{-2}$  and  $5376 \text{ Wm}^{-2}$  respectively. Figure 2.4 shows the theoretical prediction of the phonon intensity build-up against time for the 620 GHz phonons for three different steady state intensities.

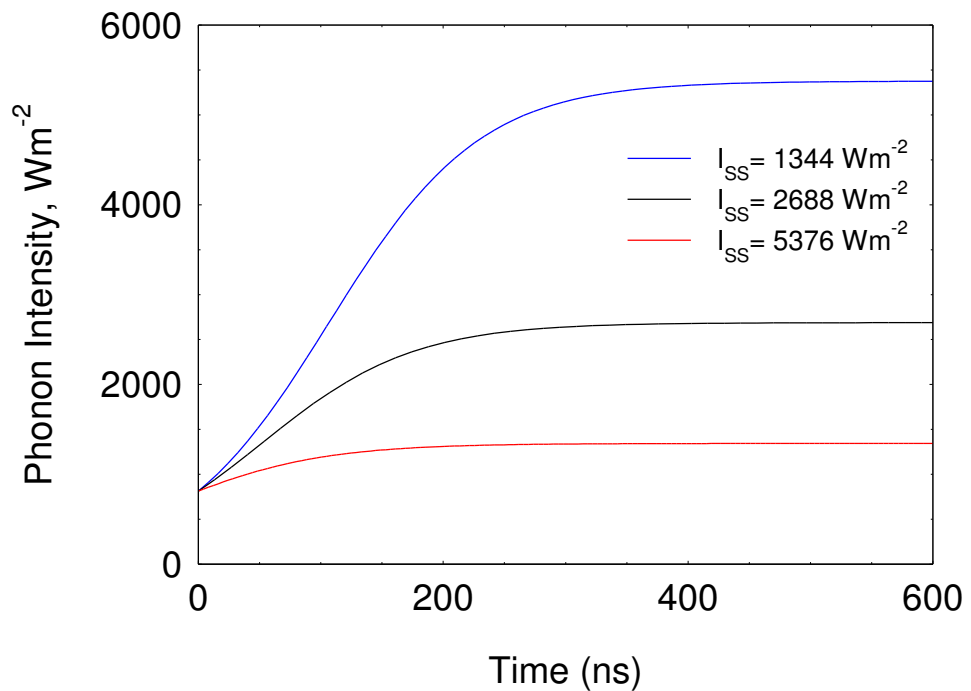


Figure 2.4: The theoretical model for the build-up of phonon intensity inside a  $2 \mu\text{m}$  SASER cavity device for 620 GHz phonon modes. The build up time for different steady state intensities is compared.

The value of  $5376 \text{ Wm}^{-2}$  is with the assumption that every 'phonon-assisted hop', between adjacent wells, is by stimulated emission. However, in reality, this may not be the case. Slight fluctuations in the growth of the device structure, leading to slight disorder in the layer thickness, may reduce the number of phonon-assisted hopping to occur for a particular frequency. Hence, the steady state intensity may be at a much lower value. This in turn reduces the time it takes

for the phonon modes at this frequency to build up to its steady state intensity. Another factor that may influence the build up time is the different experimental value of the initial intensity. However, this value is unknown and an estimate is obtained using Equation 2.45.

## 2.10 Conclusion

In conclusion, this chapter has considered the feasibility of a SASER oscillator device using a cavity made of SLs. The phonon modes that are Bragg reflected by the cavity mirrors would grow exponentially with each round trip if the gain exceeds threshold. A theoretical approach regarding the build-up of SASER oscillation was established, taking into account all possible losses from the proposed cavity. A prediction of this build-up of the SASER oscillations is also presented. A comparison of this model with experimental observations will be discussed in much more detail in later chapters.

# CHAPTER 3

## EXPERIMENTAL DEVICES AND TECHNIQUES

The aim of this chapter is to provide a detailed description of the experimental methodologies and techniques used in obtaining the results that will follow in the next chapter. This includes methods of characterising the SASER devices and details of the specific experimental apparatus used in the experiments. Improvements to the current experimental setup will also be highlighted especially in terms of the software developed for experimental control. First, a description of the SASER device structure will be presented alongside with the fabrication processes involved.

### 3.1 Device Structure

Three device structures were designed and grown on 2" GaAs semi-insulating wafers using molecular beam epitaxy (MBE) [66] in Nottingham University. Sample NU 2694 was grown by Prof M. Henini in a *Varian Gen II* whereas sample MN 685 and MN 652 were grown by Dr R. Campion in a *Veeco mod Gen III* system. The differences between the three samples are the doping levels in the gain medium and the thickness of the GaAs/AIAs layers making up the cavity mirrors.

### 3.1.1 NU 2694

The first SASER structure, NU 2694, consists of 3 SL structures where a 50 period GaAs/AlAs SL with Si donor concentration of  $2 \times 10^{16} \text{ cm}^{-3}$  (the gain medium) is sandwiched between two undoped GaAs/AlAs SLs (the cavity mirrors); one with 40 periods and another with 15 periods. At each end of the gain medium SL structure is a  $0.5 \mu\text{m}$  of GaAs contact layers that are n- doped at a level 100 times higher than the doping in the gain medium. Hence, a laterally uniform electric field is formed between the top and bottom contact layers. The gain medium SL has a lower doping concentration to minimise unwanted scattering events involving the electrons and ionized Si donors and most importantly to prevent a filled miniband state as well as involving electrons filling the next excited state in the Wannier-Stark ladder regime. A 20 nm of undoped GaAs spacer layer was grown to separate the high and low doping regions. This structure is illustrated in Figure 3.1.

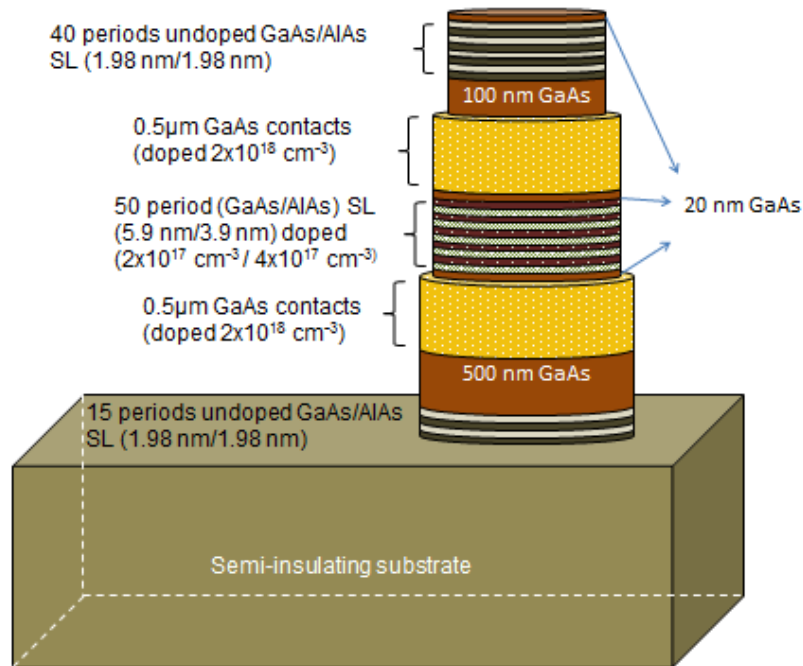


Figure 3.1: Schematic diagram of sample NU 2694. The undoped SLs acts as cavity mirrors while the doped SL situated in the centre of the structure is the gain medium.

### 3.1.2 MN 685 & MN 652

The MN 685 sample, shown in Figure 3.2, is a regrowth of NU 2694 with two changes: one is the doping profile of the gain medium SL and the other is the period of the mirror SLs. The doping level of the gain SL was increased to  $2 \times 10^{17} \text{ cm}^{-3}$  whilst the GaAs ‘spacers’ were gradually doped from the higher doping level of the contacts to the lower doping level of the SL to provide additional flow of electrons through the gain medium. On the other hand, the SL period,  $d_{SL}$ , of the mirror SL was changed to be 8 nm, instead of 4 nm. The reasons for the above changes will be discussed in later chapters.

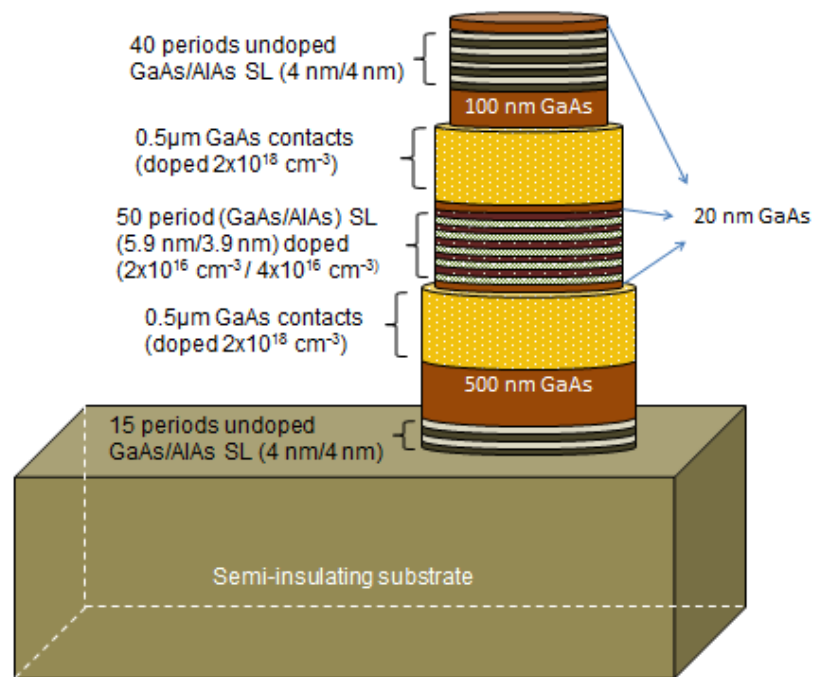


Figure 3.2: Schematic representation of sample MN 685. This structure is a regrowth of NU 2694 with slight modifications to the doping profile of the gain medium and the period of the cavity mirror SLs (8 nm).

The MN 652 sample, however, has an identical cavity structure to the MN 685 but the doping profile of the gain medium is the same as that of the NU 2694 sample. This sample was used to study the characteristics of the cavity by means of pump-probe measurements, which will be explained in a later chapter.

### 3.2 Specific Experimental Apparatus

Ballistic phonon propagation is best observed at liquid-helium temperatures where phonon–phonon scattering is significantly reduced [49]. A decrease in the thermal background allowed observation of the small effects of increased phonon population. By placing the samples in a commercially manufactured cryostat, it was

possible to achieve temperatures as low as 1.5 K. Two different cryostats were used depending on the type of experiment. The cryogenic setup for both cryostats will be explained individually in the next section. A description of the lasers employed for all related measurements will follow later.

### 3.2.1 Bath Cryostat

For low temperature bolometer and pump – probe measurements, the ‘Optistat Bath Cryostat’ made by Oxford Instruments was used. The design is shown in Figure 3.3. This cryostat contains several layers to insulate the sample space from the outer environment and ‘hold’ the cold temperature during experiments. The sample space is at the core of the cryostat, surrounded by a radiation shield thermally coupled to a liquid helium reservoir. Liquid or gas helium was then supplied to the sample space through a needle valve. An adjustable needle valve control, located at the top of the cryostat, as indicated in Figure 3.3, is used to optimise the flow of helium. Surrounding the liquid helium reservoir, and insulated from it by a vacuum space, is a liquid nitrogen reservoir, acting as a radiation shield and therefore, substantially reducing the helium boil-off rate. The outermost layer incorporates a shell of vacuum space (pumped down to at least  $10^{-4}$  mbar) to isolate the inner cryostat from the room temperature surroundings. Encompassing the sample space at the bottom end are five indium sealed quartz windows for optical access.



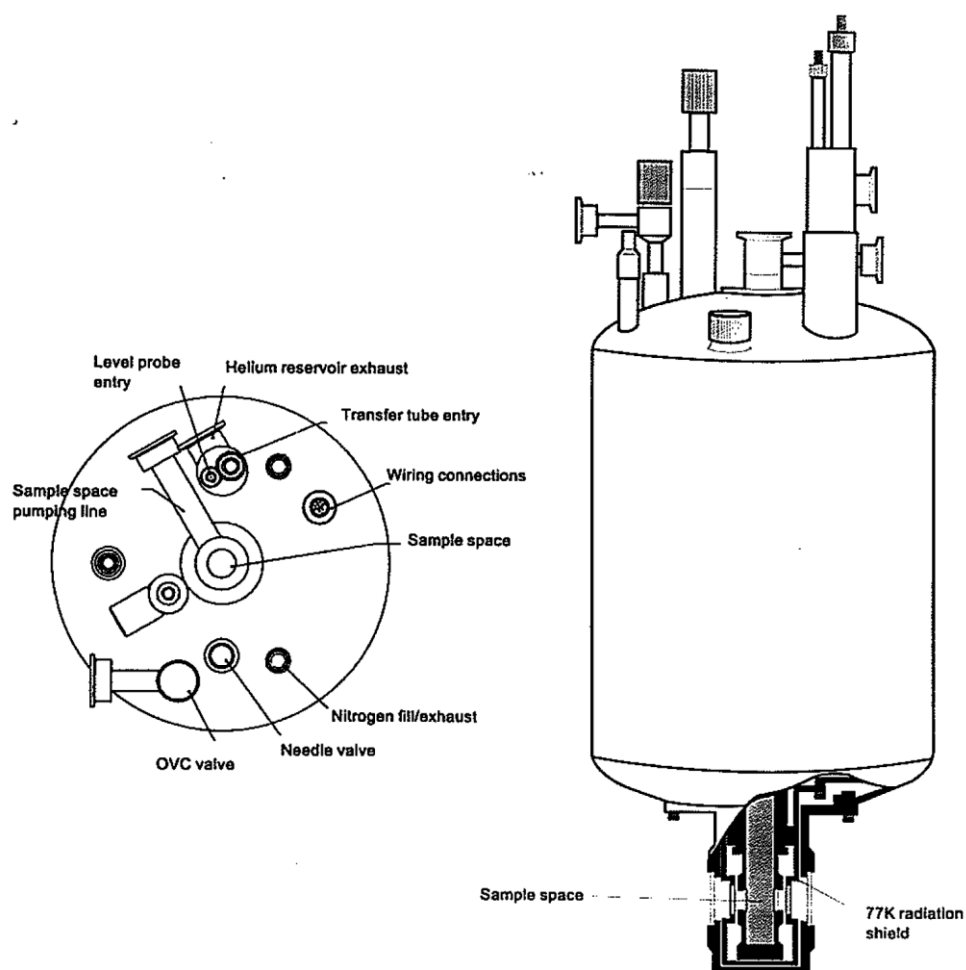


Figure 3.3: Diagram of the Optistat bath cryostat (taken from OXFORD Research Instrument manual). A temperature as low as 1.5 K was achieved by lowering the pressure in the sample space containing liquid helium using a vacuum pump.

Experiments were conducted at temperatures between 10 and 1.5 K, achieved by pumping on the sample space using a rotary pump. A manostat, situated between the pump and the cryostat, was used to set (lock) the pressure at a certain level to maintain the required temperature. Accurate measurements of the temperature within  $\pm 0.05$  K was achieved using the Allen Bradley resistor that was mounted on the sample probe together with a heater.

Below 4.5 K (in liquid helium), stable temperature was achieved by stabilising the helium flow through a combination of the needle valve

position and the manostat pressure. Above 4.5 K (in helium vapour), optimum temperature stability of the desired temperature was achieved using the heater. Stabilised temperature was controlled in both cases using the resistor by means of software, implementing a proportional-integral-derivative (PID) feedback loop.

By having a good vacuum and a filled nitrogen reservoir, to minimise helium boil-off rates, low temperatures are maintained in the system up to a full day, without the need to refill the liquid helium reservoir during experiments.

The sample holder, as shown in Figure 3.4, was mounted at the bottom of the sample rod. Coaxial pin connections are available from the head of the rod that may be used to make connections to any devices on the sample. A Vernier micrometer, also located at the rod head, provided height control for the sample holder. It was also possible to rotate the rod to make the sample's surface in parallel with one of the cryostat windows if required.

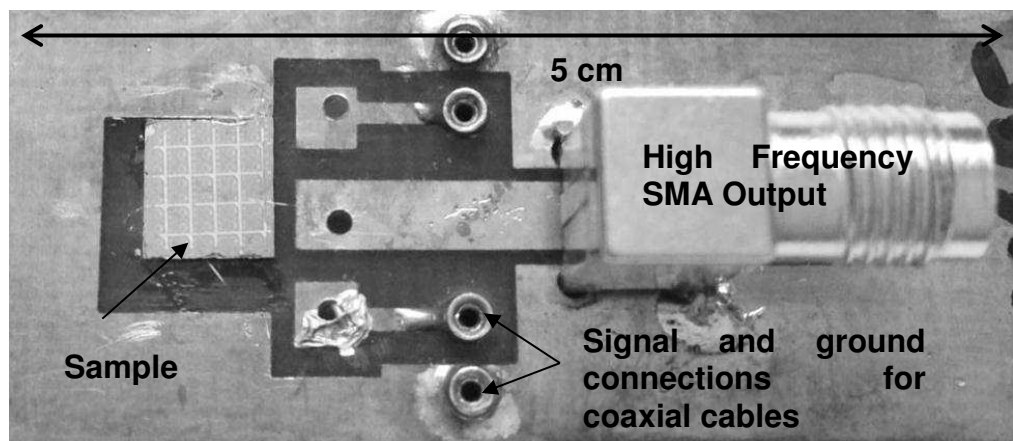


Figure 3.4: The sample holder used for the Optistat cryostat comprised of a copper clad PCB. Gaps between the copper plates were intended to isolate individual electrical circuits. The outermost copper plate was grounded.

### 3.2.2 Continuous flow cryostat

For the photoluminescence (PL) measurements, a continuous flow, 'Microstat He', cryostat manufactured by Oxford Instruments was employed. Figure 3.5 illustrates the design of this cryostat. As in the case of the Optistat cryostat, an outer vacuum chamber is pumped to high vacuum to thermally insulate the sample space and radiation shields from its room temperature surroundings. Two windows were permanently bonded to the outer vacuum chamber flange, to allow optical access to the sample. The outer vacuum chamber flange was shaped specifically for the sample to be mounted as close as possible to the inside surface of the windows to maximise the numerical aperture.

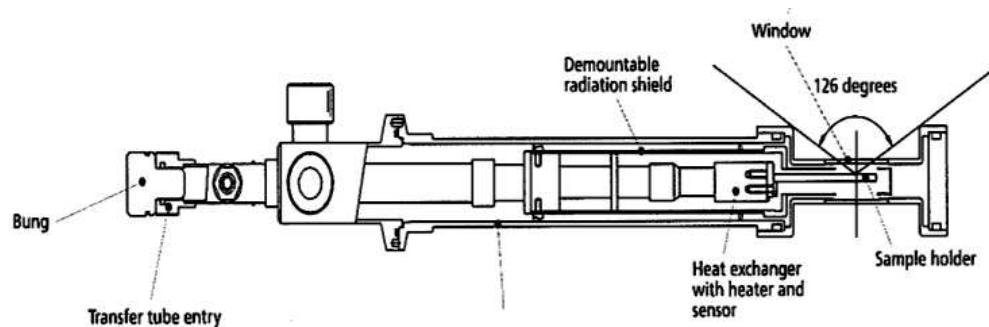


Figure 3.5: Diagram of the continuous flow cryostat taken from the Oxford Instruments manual. The heat exchange combined with a heater and a sensor provides accurate control of the temperature using PID feedback algorithm.

Helium was transferred continuously from a helium Dewar to the cryostat using a well-insulated transfer tube. A needle valve located on the transfer tube was used to control the flow. The sample was mounted on a heat exchanger that thermally couples the liquid helium to the sample. Through a combination of the heater and sensor incorporated in the heat exchanger, stable temperatures were attained. The temperature was measured and controlled by the ITC

503 (also provided by Oxford Instruments) temperature controller that used a PID feedback system. Temperatures as low as 3.8 K may be achieved under constant pumping from a large (40 m<sup>3</sup>/hr) rotary pump.

### 3.2.3 Laser

Two different lasers were used for PL measurements. For the NU 2694 sample, a diode pumped solid state laser (3<sup>rd</sup> harmonic Nd:YAG laser) with Q-switch acousto-optic modulator (AOM), model LCS-DTL-374QT, supplied by LASER 2000 was used. This 3B class laser has maximum pulse energy of 30 μJ with 10 ns pulse duration at a wavelength of 350 nm. To achieve this, the 1060 nm wavelength of the Nd:YAG laser beam goes through a frequency doubler crystal, located inside the laser cavity. The beam then recombines with the 1060 nm beam (frequency mixing) to obtain the 350 nm beam. On the other hand, for the MN 685 sample, a class 2 solid state laser, operating at 690 nm, was used.

For pump-probe measurements, a Spectra Physics 'Tsunami' mode-locked tuneable Ti:Sapphire (Titanium-doped sapphire) solid-state laser was employed. Mode locked laser pulses with wavelengths ranging from 690 nm to 1080 nm, with 120 fs pulse duration and a repetition rate of 82 MHz are emitted. An output of at least 1 W was attainable between the 790 nm and 850 nm. The Ti:Sapphire rod is pumped using a Spectra Physics 'Millennia Xs' continuous wave laser. This class 4, diode-pumped, laser uses Nd:YVO<sub>4</sub> as a gain medium and provided 10 W of continuous laser beam at a wavelength of 532 nm.

### 3.3 Device Fabrication Procedures

The fabrication procedures described below were only applied to the NU 2694 and MN 685 samples as the MN 652 sample was not processed into a SASER device. The key elements in fabricating the SASER devices are explained as follows. First, a sample, typically 5 mm x 5 mm in dimension, was obtained by cleaving from the MBE wafers. Any contamination on the chip's surface was then removed using the nominal 'four solvent clean' process in a manner of increasing purity (ethyl lactate, acetone, methanol and isopropyl alcohol (IPA)). Residual solvents were removed by baking the chip in an oven for 10 minutes at 130 °C.

#### 3.3.1 Photolithography and Wet etching

Patterning of the device was done by employing standard photolithographic techniques whereby a positive photo resist (BPRS 100) was used to form the mesa pattern, ranging from 20  $\mu\text{m}$  to 400  $\mu\text{m}$ , through the exposure of UV light from a Karl Suss MJB 3 mask aligner. The pattern was developed using a positive developer solution, AZ 400k, with a ratio of 1:8 (developer: water). The intended height of the mesa was obtained by standard wet etching techniques using  $\text{H}_2\text{O}_2:\text{H}_3\text{PO}_4:\text{H}_2\text{O}$ , 10:1:20, with a typical etch rate of 1.2  $\mu\text{m}$  per minute. The etch rate was monitored every 30 s intervals using a DekTak 3 surface profiler, providing an accuracy of  $\pm 20$  nm over the feature height.

In one particular case, it was necessary to remove all layers situated above the 50 period gain SL structure whilst making sure the etching stopped at the first SL layer. To achieve this, nominal wet etching, as mentioned above, was used up to the GaAs layers followed by a selective wet etching technique using a solution of citric acid :  $\text{H}_2\text{O}_2$ ,

4:1; etching GaAs over AIAs with a selectivity of around 1450 [67]. The first AIAs barrier in the gain SL was used as the etch stop, enabling complete removal of the GaAs layers with the loss of only one period of the SL.

### 3.3.2 Contacts metallisation and Annealing

Contacts were made by means of evaporating In/Ge-Au and annealing at a specific temperature. Both contact regions, in both samples, were *n-type*, so the same metallisation materials were used. Equal masses of indium and germanium were put in one evaporating boat and evaporated to a thickness of  $40 \pm 1$  nm at  $\sim 1 \times 10^{-6}$  mbar using an Edwards E306A evaporator. Then  $110 \pm 1$  nm of gold was evaporated onto the chip at the same pressure.

The metallic layer was then annealed using an Anealsys, AS-one, rapid thermal annealer (RTA), to diffuse the indium germanium into the GaAs contacts region, in a hydrogen: argon (5:95) atmosphere. The Argon purge gas used in the RTA prevents formation of oxide layers at the elevated temperatures. The annealing was done in a ramped sequence, where the temperature is ramped from room temperature up to a maximum of 420 °C with a 120s of ramp up time and a 30 s dwell time at the maximum temperature. The bottom contacts (grid) were annealed at 390 °C, a slightly lower temperature than that of the top contacts. The chip was then cooled down to room temperature naturally. The final picture of the fabricated device is shown in Figure 3.6.

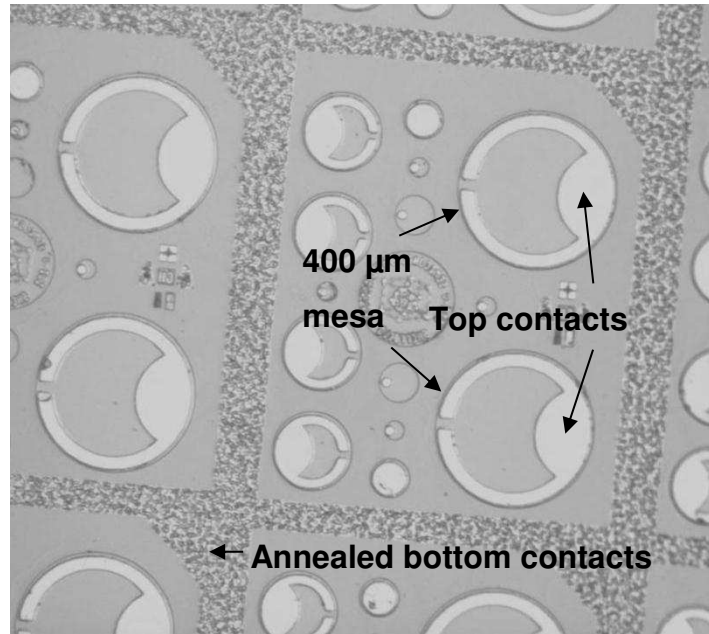


Figure 3.6: The devices on the chip before bonding the contacts. The horseshoe-shaped contact was connected to a contact pad on the sample holder with a bond wire, and the grid is bonded to ground.

The final part of processing was to bond the desired device to the contact pads (on the sample holder – refer Figure 3.4); to enable charge transfer during experiments. The bottom contacts (grid) were bonded to ground.

### 3.4 Characterisation Techniques

Upon obtaining a potential SASER device, it is essential to test that the device functions correctly, in that current can be passed through the gain medium SL structure. This was done by observing the transport properties of the gain medium SL from Current–voltage (IV) measurements of the device. However, Pump–probe reflectivity and bolometric (by optical excitation) measurements, which will be described later in this chapter, are both sensitive to the optical

excitation energy. Hence, it is essential to determine the optical resonance (electron–hole) of the SL structures under investigation. This was done by performing photoluminescence (PL) measurements, where the excitonic energy related to each individual SL structure may be verified.

### 3.4.1 Current-Voltage Measurements

Current-voltage (IV) measurements were conducted by applying a bias, from a Keithley Digital Voltage Source (DVS), to the device that was in series with a  $10\ \Omega$  load resistor. The scheme of operation is presented in Figure 3.7, where the voltage across the resistor was measured by a Digital Multi Meter (DMM). By using Ohms law, the corresponding current through the device was obtained.

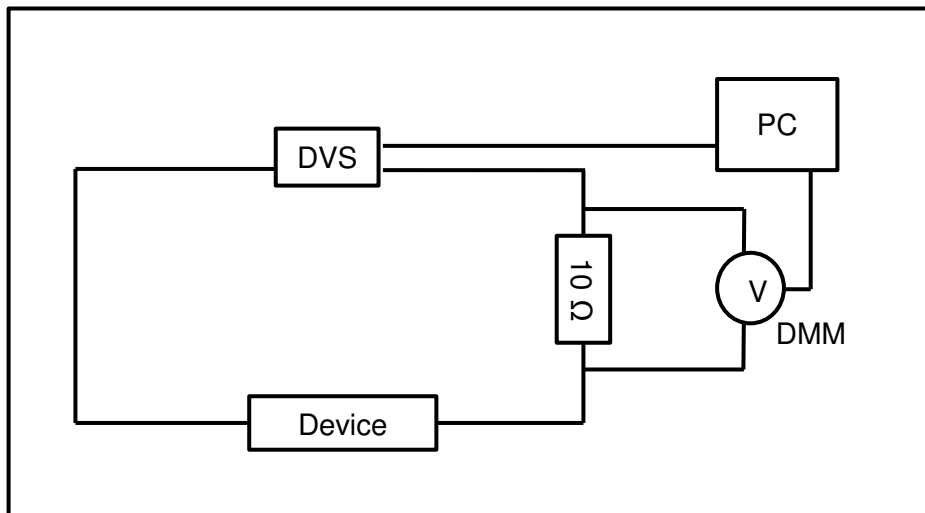


Figure 3.7: The IV setup to measure the current flowing through the gain medium SL structure for both samples. The device was biased, using a Digital Voltage Source (DVS) and the corresponding voltage drop across the  $10\ \Omega$  resistor was measured by the Digital Multi Meter, DMM.



In the case where the device resistance was considerably higher than the load resistor, the voltage dropped across the load resistor would be negligible and the voltage dropped across the device (and the SL structure) is approximately be equal to the applied bias. If, however, the resistance becomes comparable to the load resistor, the actual voltage dropped across the device must be corrected by taking the difference between the applied bias and the voltage dropped across the 10  $\Omega$  resistor.

A typical IV graph for a biased SL is shown in Figure 3.8. Normally, the current increases linearly with bias as soon as transport commences in the SL structure. At higher biases, the current then oscillates with the bias in the region of negative differential conductance; a phenomenon commonly observed in SLs [68]. A much more detailed description of the IV characteristics of a SL will be presented in Chapter 5 alongside with the results pertaining to the specific device under investigation.

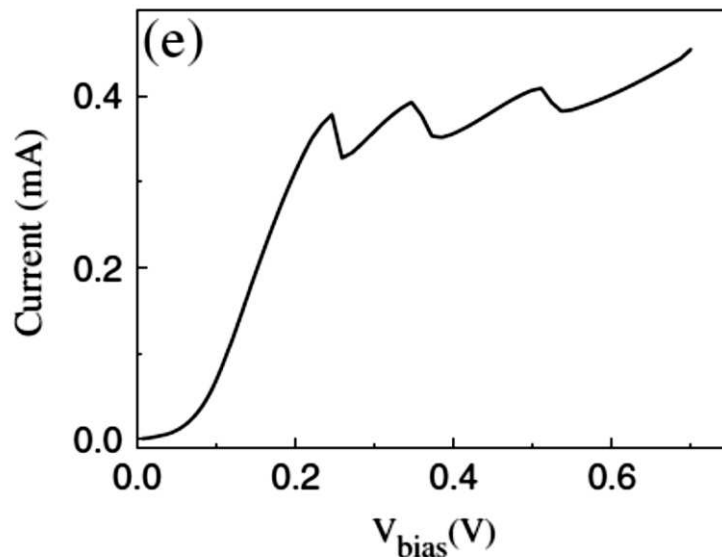


Figure 3.8: Typical IV characteristics of a SL under vertical electron transport, obtained from [37]. As the SL undergoes hopping transport, the current increases linearly with bias until negative differential conductance occur in the structure.

### 3.4.2 Photoluminescence (PL) Measurements

The heavy-hole excitonic peak for the mirror SL and the gain medium SL (refer Figure 3.1 and 3.2 for the sample structure) were determined by PL measurements. The lasers used for this measurement is as described in Section 3.2.3. A schematic diagram of the PL setup is shown in Figure 3.9. The laser beam goes into a periscope, for height adjustment, and into a beam splitter prism. The beam then travelled through a large 100 mm-diameter (collecting) lens before arriving at the chip's surface. A portion of the luminescence from the sample was collected by the lens and focused into a spectrometer.

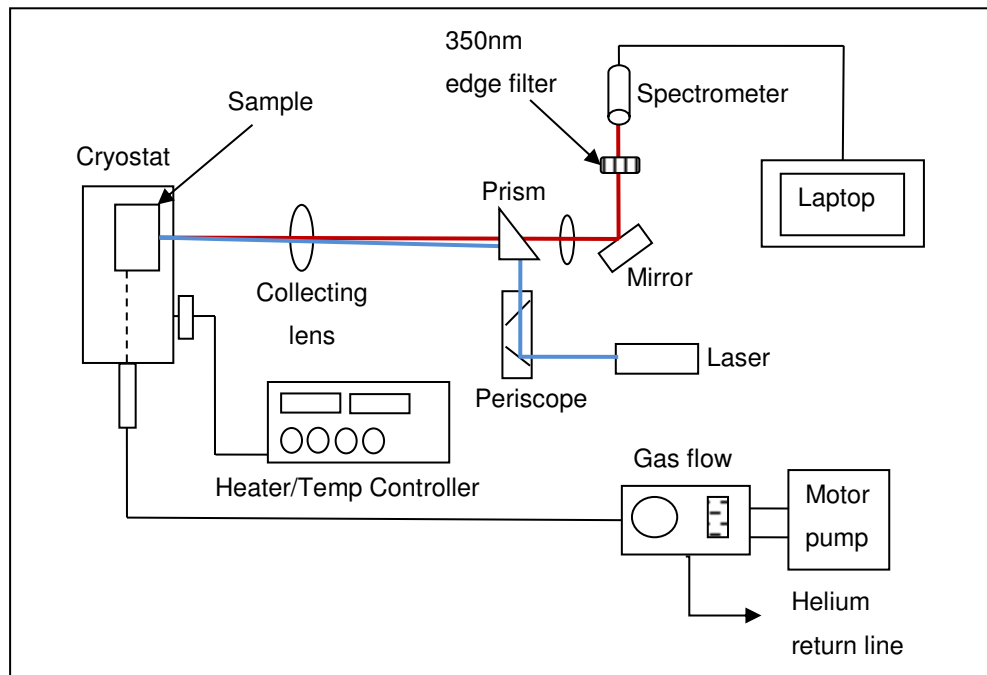


Figure 3.9: Schematic diagram of the PL setup. Near UV light was used to excite the sample (350nm). The light entered a periscope, for appropriate height adjustments, and deflected on a prism before reaching the sample. The luminescence from the sample was collected using a lens and analysed with a CCD spectrometer.

The spectrometer was controlled by software, which was provided by Ocean Optics, to view, save, subtract from the spectrum with the dark spectrum (removing unwanted background) and set the required integration time. A 350 nm edge filter was introduced to remove any laser light that was directly reflected off the chip's surface (only when studying the PL in the NU 2694 sample). The experiment was performed at 4.6 K, stabilised by means of a heater/temperature controller, while liquid helium was continuously pumped into the (continuous flow) cryostat. The results pertaining to the different SL structures in both samples are included and discussed in Chapter 4.

### 3.5 Time-Resolved Pump-Probe Experiment

Time delay modulation techniques using femtosecond lasers are commonly used in investigating relaxation processes in SLs [69-71]. There are a variety of ways of conducting the pump – probe measurements, however, the basic principle of operation is very similar [72]. In all cases, an intense beam (pump pulse) from the laser is incident onto the sample followed by a slightly less intense delayed beam (probe pulse). The pump pulse excites the SL structure in the sample and the delayed probe pulse, reflected or transmitted from the sample, is measured. By sweeping across a range of time delays, with appropriate intervals, an overview of the relaxation processes in the sample as a function of time was obtained.

The pump–probe setup, used for the work in this thesis, is explained as follows: starting with the optical arrangement, followed by a

description of the electronics involved in data acquisition. Significant improvements, made in this thesis, to the original pump–probe system involved: replacing the original lock-in amplifier with one having higher frequency bandwidth (up to 200 MHz as opposed to the 100 KHz limit) and introducing a long mechanical delay stage, the Newport Stepper, with all the experimental parameters controlled using custom written Visual Basic software. The improvements in the program will be explained in Section 3.5.2.

### 3.5.1 Optical Arrangement

The Tsunami laser, as described in Section 3.2.3, was employed in the pump-probe measurements. The mode locked laser output was split into two beams by means of a beam splitter where the 90% that passes through was referred as the pump beam. The remaining 10%, reflected from the beam splitter, was chosen as the probe beam. The probe beam was focused to a spot size of less than 50  $\mu\text{m}$ ; spatially overlapped with the 200  $\mu\text{m}$  diameter pump spot on the sample surface. A detailed experimental setup for this experiment is as shown in Figure 3.10.

A 2 meter focal length lens was introduced in the pump path just after the beam splitter to help reduce the divergence of the pump beam, hence, minimise unwanted clipping as it passed through some optical components further along the beam path. The pump beam, deflected by a mirror, travelled into a retro-reflector, positioned on top of a delay stage.

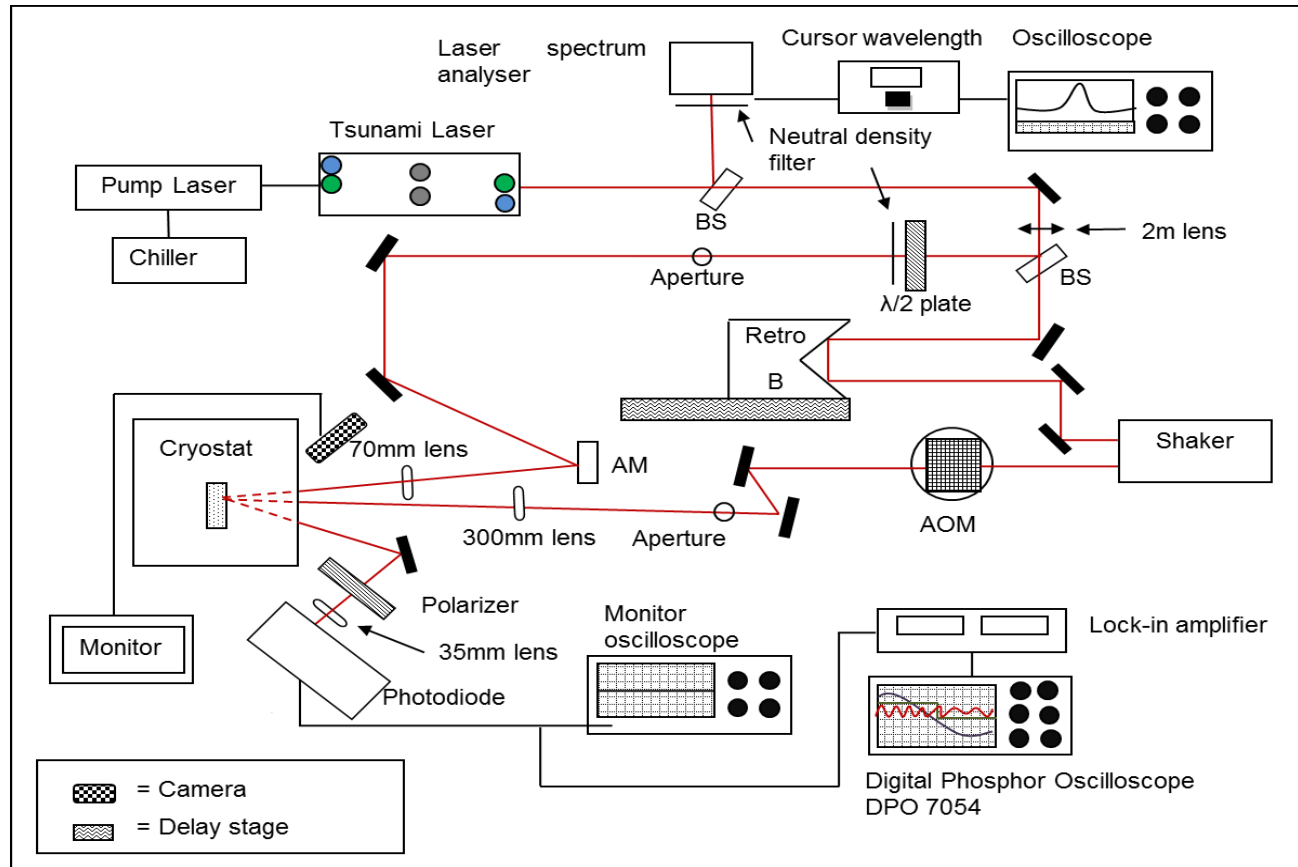


Figure 3.10: Schematic diagram of the experimental setup for pump - probe measurements.

Upon obtaining a parallel beam in and out of the retro', the beam was then directed of the edge of a mirror into another retro mounted on a 'shaker'. The shaker was used for fast scanning across a 55 ps window at 2.5 Hz, giving a resolution of 10 GHz but with high signal to noise ratio due to averaging. A longer mechanical delay stage was introduced to provide a scan of up to 2 ns with a temporal resolution of 0.1 ps.

The probe beam on the other hand, passed through a half wave plate, so that the polarisation of the emerging probe beam was orthogonal to that of the pump beam without reducing its intensity. The probe beam was then steered to the sample via a few mirrors before being focused on to the sample using a 70 mm lens.

The reflected beam from the sample was deflected by a mirror and focused into the active part of the photo diode using a 35 mm focal length lens. A linear polariser was introduced before the photodiode to preferentially select the probe beam. Hence, signals due to stray reflections from the pump and scattered light were reduced. The photo diode measures the change in reflectivity of the probe light that is induced by the pump pulse, at a known time delay after the pump beam was incident onto the sample. The signal voltage generated by the photodiode was monitored by a TDS 2022 Tektronix digital oscilloscope (200 MHz bandwidth) and recorded by the lock-in amplifier.

### 3.5.2 The Electronics

The electronics involved in the data acquisition is relatively straight forward. The signal voltage from the photodiode was fed into the SR844 RF Lock-In Amplifier, where the signal was averaged over a specified time-constant and was locked to the AOM frequency.

Choosing an appropriate time-constant was essential, especially if the shaker was used as the optical delay line. Choosing a long time-constant is favourable in terms of high signal to noise ratio, however, care must be taken so that the lock-in can follow the wanted changes in the signal.

If the shaker was used, the Newport delay stage was set to a fixed position corresponding to the centre of the required scan range. The data points from the lock-in were recorded by a DPO 7054 Tektronix digital oscilloscope, providing additional averaging. This fast scope had a 0.5 GHz bandwidth and a sampling rate up to 40 GS/s. The scope was triggered by the shaker and any data taken before triggering was ignored. However, if the Newport delay stage was used then the data obtained from the lock-in was transferred directly to the computer by means of a GPIB cable. The software program for this is explained as follows.

All experimental aspects including data acquisition, temperature regulation, resolution and the temporal time window of the data, the probe delay time and the speed of the mechanical delay stage were controlled using custom written software. However, only the major contribution of this work to the overall software suite will be outlined. This was the program and the user interface generated to control the Newport delay stage and data acquisition. A flow chart of the program is illustrated in Figure 3.11.

The speed of the retro, moving on this Newport mechanical delay line, was set according to the resolution, lock-in time constant and length of the scan defined by the user. The delay line triggers the lock-in to start recording data at a sample rate (internal sample rate) determined by the set time – constant. All the data was stored in the lock-in's buffer before being transferred to the computer.

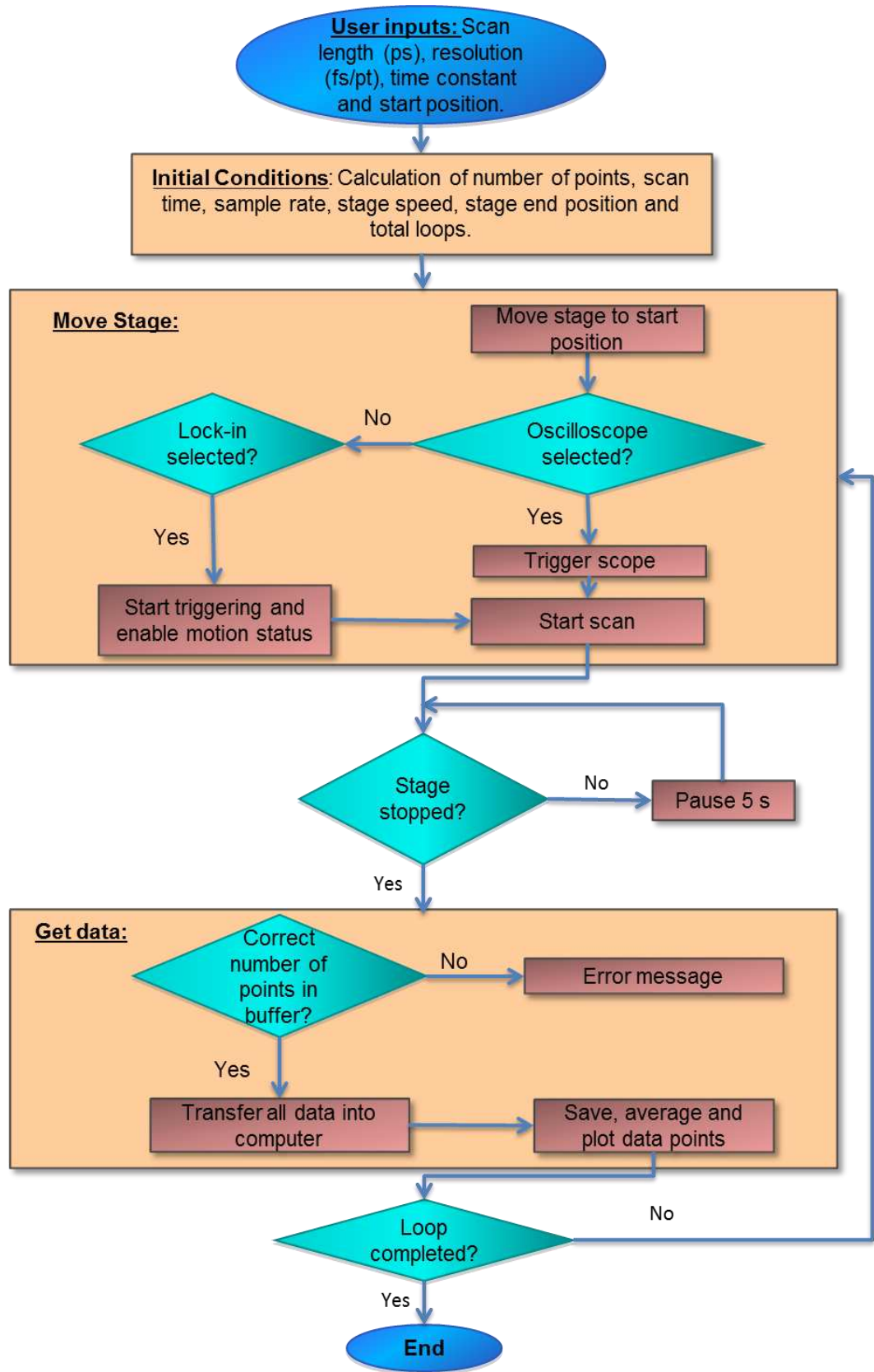


Figure 3.11: Flow chart of the Visual Basic program for experimental control.



## 3.6 Bolometric Detection

Thin granular Al films, making up the superconducting bolometers, are commonly used as phonon detectors in heat-pulse experiments as they have a rapid response time and are highly sensitive to the phonon flux incident upon them. These bolometers have extremely small heat capacities yielding very short thermal relaxation times when thermally coupled to the liquid helium surrounding the sample [73]. The process of fabricating a bolometer is detailed below followed by the experimental description of the bolometric measurements.

### 3.6.1 Bolometer fabrication

The back surface of NU 2694 was infused with indium during the growth process, which had to be removed, by means of polishing, before fabricating the bolometers. The sample was polished using a Multipol polisher to provide the smooth GaAs surface for the bolometers. The SASER devices created on the surface of the chip were protected from scratches by placing face down on a thin glass slide containing a few drops of photo resist and left to dry naturally.

To start the polishing, the surface of the chip requiring polishing is mounted face up on a metal plate with wax. The metal plate was then fastened onto the polisher jig. A low power pen laser was used to optically align the chip's surface level so that the chip's plane was in parallel with the plane at the bottom of the jig. The chip was then polished on a solder lap using a 14 $\mu$ m grade diamond paste. After the indium was completely removed, the chip was polished further

with Insec chemical-mechanical polishing solution on a felt lap, producing a mirror finish.

Upon obtaining a smooth surface, the chip is now ready for bolometer fabrication. The reverse side of the chip was spin coated with photoresist (BPRS 100) and baked in the oven for 30 minutes at 110 °C. Then the nominal photolithographic technique, as described earlier, was used to pattern the bolometer onto the GaAs substrate. The sensitive part of one bolometer needs to be exactly opposite the active device. Since GaAs and the GaAs/AlAs SL layers are transparent to infrared (IR) light, it was possible to line up the sensitive part of the bolometer pattern with the active device, under IR illumination.

Then, 37 nm of granular aluminium (Al) film was deposited onto the developed bolometer pattern. To form a granular Al film, pure Al was evaporated from a alumina crucible to introduce some oxygen impurities. By introducing these impurities in the Al, the superconducting transition temperature was shifted from 1.18 K for pure Al to ~ 1.8 - 2.4 K and broadened so that the bolometer was not easily saturated. Remaining resists on the substrate were removed with acetone and the chip was rinsed with IPA.

The detection region of the bolometer has an aspect ratio of 1:10 as shown in Figure 3.12, to provide a good balance between the sensitivity (the narrow width) and stability (wide u – shape) of the bolometer. The resistance of the bolometer depends strongly on the thickness of the evaporated film due to these fine features. At room temperature, a typical bolometer has a resistance of 100–300  $\Omega$  depending on the thickness of the evaporated film.

The final step was to contact the bolometer. Indium wires were pressed onto the bolometer contact pads and onto an available contact pad on the sample holder. The indium wires were secured

with conductive silver paint and left to dry. GE varnish was used to affix the chip onto the sample holder with the device facing upwards. A hole, predrilled on the sample holder, allowed space for the indium wires to stay attached to the bolometer contact pads.

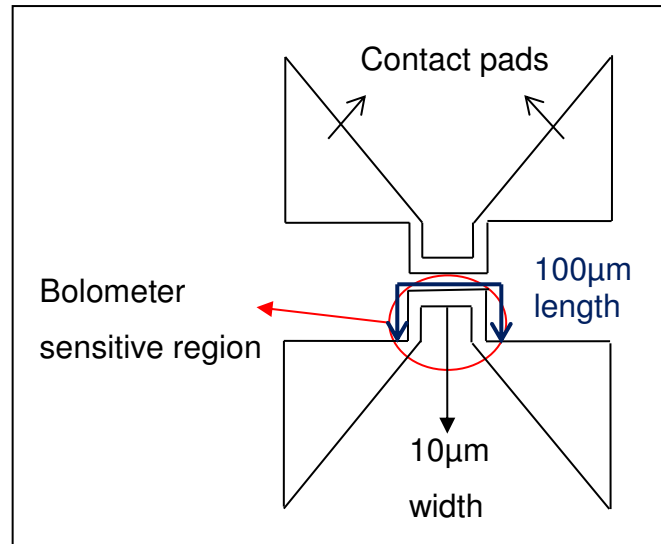


Figure 3.12: Representation of the bolometer where the sensitive detection region has a length to width ratio of 10:1. The bolometer comes in pairs; however, only one bolometer was needed to be aligned to the active device.

### 3.6.2 Principle of Operation

Two types of bolometer measurement were conducted and the results obtained in each are separately discussed in Chapters 5 and 6. In both cases, the gain medium SL was electrically excited and the phonons traversing the GaAs substrate were detected by the bolometer. The only difference between the two measurements was that in the first case a pulsed bias was applied to the device and in the latter case, a laser was used to excite the first SL layer whilst a DC bias was applied to the device.

In both cases, the chip was cooled down to just below the superconducting temperature of the (granular) Al, as shown in Figure 3.12. The working temperature for all bolometer measurements is indicated in Figure 3.13 by the dotted line, pinpointing to the bottom of the transition curve. A slight rise in temperature would consequently push the Al up the transition and hence, change the resistance of the bolometer significantly. It was important, therefore, that the chip was at a stable temperature (part of reason for being mounted in liquid helium), so that, the change in temperature was not due to the entire chip heating but due to non-equilibrium phonon fluxes arriving at the bolometer. The stable (superfluid) temperature was achieved by pumping the sample space, containing the liquid helium, as described in Section 3.2.1.

Sometimes a 'double transition' was observed, as shown in Figure 3.13, resembled by the kink in the transition curve (black solid line in the figure). This is possibly due to the critical temperature for the wider contact pads, where the bolometer was bonded, being different to the active region. Therefore it was also crucial to set the correct initial temperature on the right part of the transition so that the slight rise in temperature was within the linear regime of the transition curve for the sensitive detection region.

The setup for a bolometer measurement from an electrically excited SL is shown in Figure 3.14. The Philips PM5715 pulse generator sent single 300 ns pulses with  $< 6$  ns of ramp time and a repetition time of 100  $\mu$ s. Specific parameters of the signal generator pertaining to each investigated sample will be presented in Chapter 5. An attenuator was used, to attenuate the bias at a range between 10 to 30 dB. An additional, 0.5 dB attenuator pad made from resistors was also introduced to provide extra resolution.

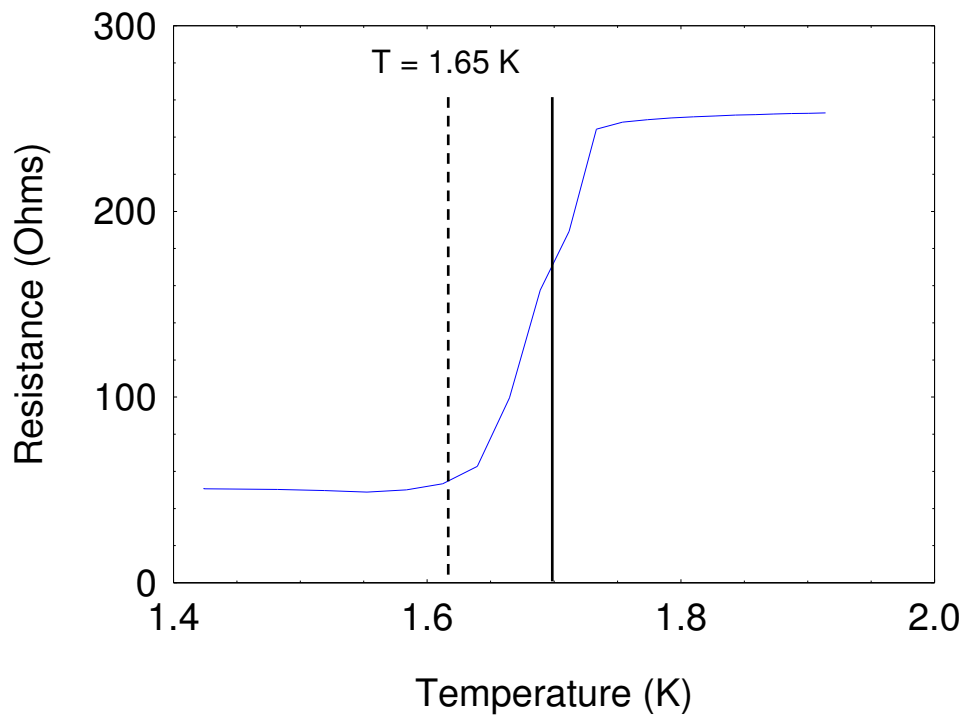


Figure 3.13: Graph representing the superconducting transition for a typical bolometer. The dotted line indicates the bottom of the transition curve which is the ideal temperature for conducting the experiment. The solid black line indicates the position of a second transition, also observed under experimental conditions.

A constant voltage bias was applied to the preamplifier box consisting of a 10 K $\Omega$  resistor in series with the bolometer, to provide small currents (typically  $\sim 100 \mu\text{A}$ ) for the bolometer. The bolometer signals, provided by the small change in resistance, at each attenuated bias were then amplified 100 times before being recorded by the DPO oscilloscope. Generally, it was desirable to have a bolometer resistance of 50 – 100  $\Omega$ , at the superconducting temperature, in order to match the impedance of the signal preamplifier and standard electrical coaxial cables.

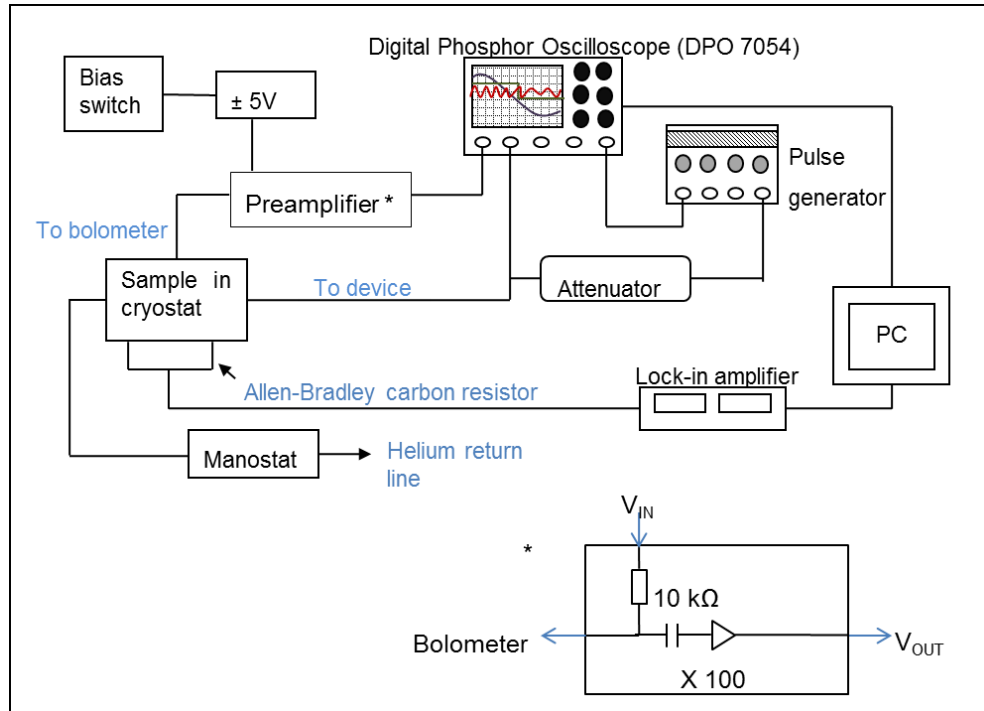


Figure 3.14: The setup for bolometer measurements conducted at around 2 K. Electrical pulses were sent to the active device from a pulse generator and the signal obtained at the bolometer was amplified and recorded using the DPO oscilloscope. A constant (small) current was sent to the bolometer by means of a 10 K $\Omega$  resistor inside the preamplifier box.

### 3.6.2.1. *By optical excitation*

To observe the effects of injection seeding in the SASER device, phonons at specific frequency may be injected into the cavity device by optically exciting the first mirror SL. The bolometer then detects the phonons escaping the cavity. The same setup as shown in Figure 3.14 was employed with two additional apparatus introduced, namely the Tsunami laser and a pulse selector.

An APE Pulse Select, single pulse selector, was introduced just after the laser to reduce the laser's repetition rate. This was necessary as the phonons need  $\sim 100$ 's nanoseconds to reach the bolometer and

an overlap of pulses may be avoided by introducing sufficient time lengths between each laser pulses. The pulse selector, based on an AOM, provided means of selecting a pulse at a certain slower rate than that of the laser using a division ratio defined by  $x$  as

$$\frac{82 \text{ MHz}}{x}, x \geq 2 \quad (3.1)$$

The division ratio may be set between 2 and 200000. Typically in the current measurements, the division ratio was set to 1000.

### 3.7 Conclusion

This chapter has provided detailed descriptions of the experimental methods and characterisation techniques, alongside with the specific apparatus employed. The method for obtaining low temperatures and the fabrication process for the device and the bolometer has also been explained.

# **CHAPTER 4**

## **OPTICAL CHARACTERISATION OF THE CAVITY**

This chapter focuses on the study of the SASER cavity by means of pump-probe measurements. The essential properties of the SASER cavity such as the phonon round trip time and the attenuation in phonon intensity with each round trip obtained from these measurements are discussed and compared with theoretical estimates from Chapter 2 for sample MN 685 and NU 2694 respectively. However, the optical characteristics of the SL structures must first be obtained. This was achieved by photoluminescence (PL) measurements, as described in the next section.

### **4.1 Optical (electron-hole) resonance of the SLs**

Photoluminescence (PL) measurements were conducted on two samples, NU 2694 and MN 685, to determine the first interband transition of each SL structure. The structure of the mirror SLs in both samples was the same; hence only one of the mirrors was investigated. For the case of sample NU 2694, electrons were excited in the SL structures by the 355 nm Nd:YAG laser. However, due to the short wavelength, most of the laser light is absorbed by the first SL structure. Therefore, the first SL structure of sample NU 2694 was completely removed, by means of selective wet etching as described in Chapter 3, to enable direct optical excitation of the gain



medium SL structure. Figure 4.1 illustrates the scheme of operation for PL measurements on both samples.

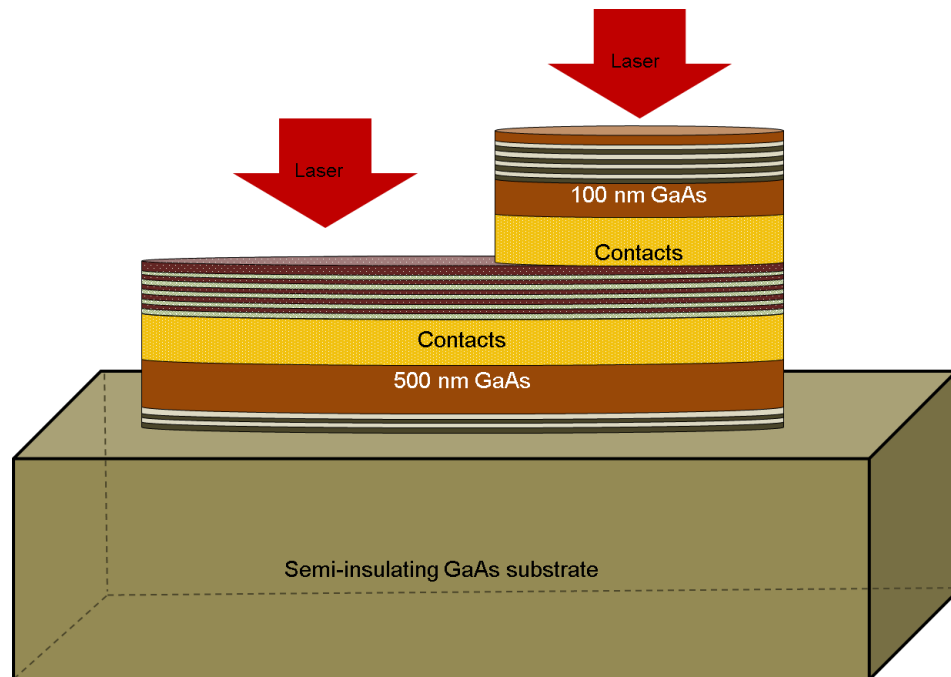


Figure 4.1: Photoluminescence from the different SL structures was observed by optically exciting the SL structure(s). For sample NU 2694, the first mirror SL structure was completely removed, by means of chemical etching, to allow direct photo excitation in each SL structure of interest.

If the incoming photons provided enough energy to excite electrons from the valence band into the conduction band (photon energy greater than the SL band gap energy), then the promoted electrons leave behind holes in the valence band. After relaxing excess energy, the electrons recombine with the holes, forming excitons, and emit luminescence with an energy corresponding to the interband transition for the SL structure. This is illustrated in Figure 4.2.

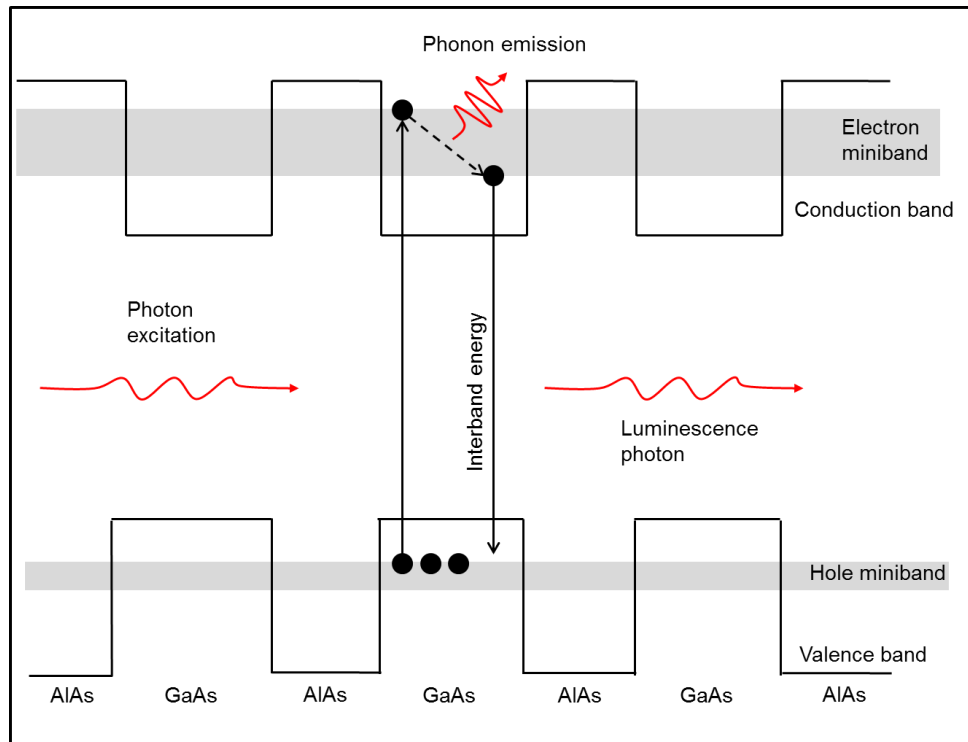


Figure 4.2: The process of photoluminescence for a type I SL where the incident photons excite the electrons into the conduction band and the emitted photon luminescence provided a measure of the interband energy gap.

Figure 4.3 reveals the PL peaks for sample NU 2694 with each associated wavelengths of the luminescence labelled accordingly for each structure. The mirror SL indicated a resonance centred at 663 nm and the middle SL peaked at 758 nm. The mirror SLs in this sample are type II SLs. Therefore the intensity of the PL peak for this SL structure may be two orders of magnitude weaker than that of a type I SL (the gain medium SL is type I) [74]. The PL peak at 818 nm may correspond to the band gap of GaAs at low temperatures (1.516 eV) which would arise from the 0.5  $\mu\text{m}$  GaAs contact layers. A small peak observed at 831 nm (24 meV smaller than the band gap of GaAs) possibly resulting from residual donor–acceptor recombination [75, 76].

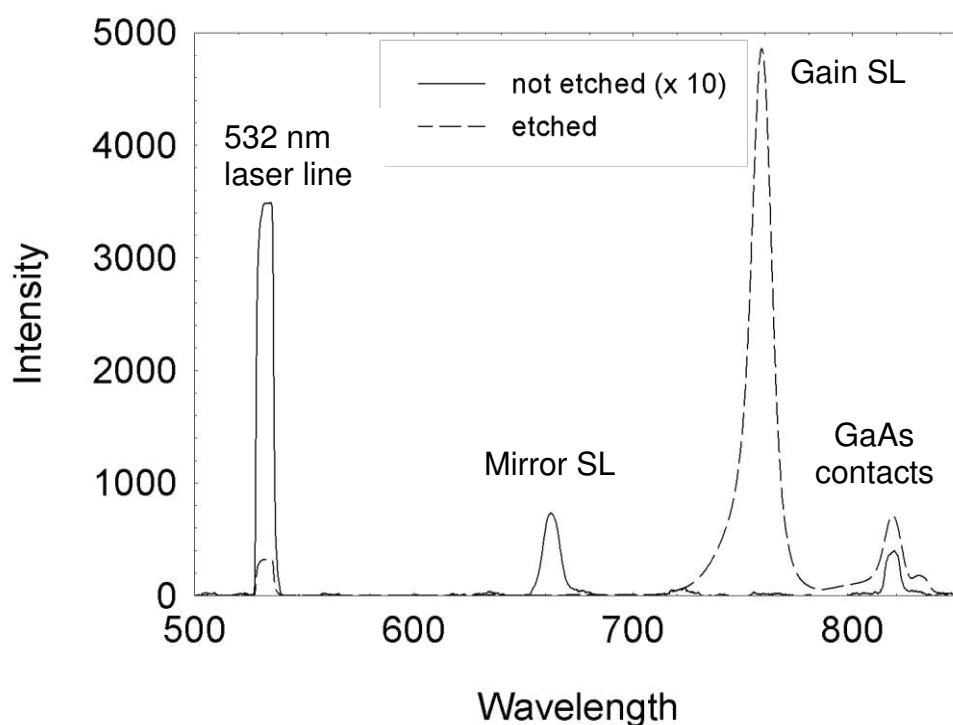


Figure 4.3: The luminescence spectrum for sample NU 2694. The mirror SL had an optical resonance centred at 663 nm whilst the gain medium SL peaked at 758 nm.

The MN 685 sample was excited with a 690 nm solid state laser. This laser is operating at a longer wavelength compared to the Nd:YAG laser employed for sample NU 2694; providing enough light penetration to excite the gain medium SL and reveal an additional peak in the PL spectrum. Therefore, it was not necessary to remove any of the SL structures in this case. Figure 4.4 shows the resonant excitonic energy of the SL structures in sample MN 685. The PL peak for the mirror SL was centred at 718 nm and for the middle SL at 759 nm (the same as the one in NU 2694). As previously explained, the 818 nm and 831 nm exciton peaks is possibly from the GaAs contact layers.

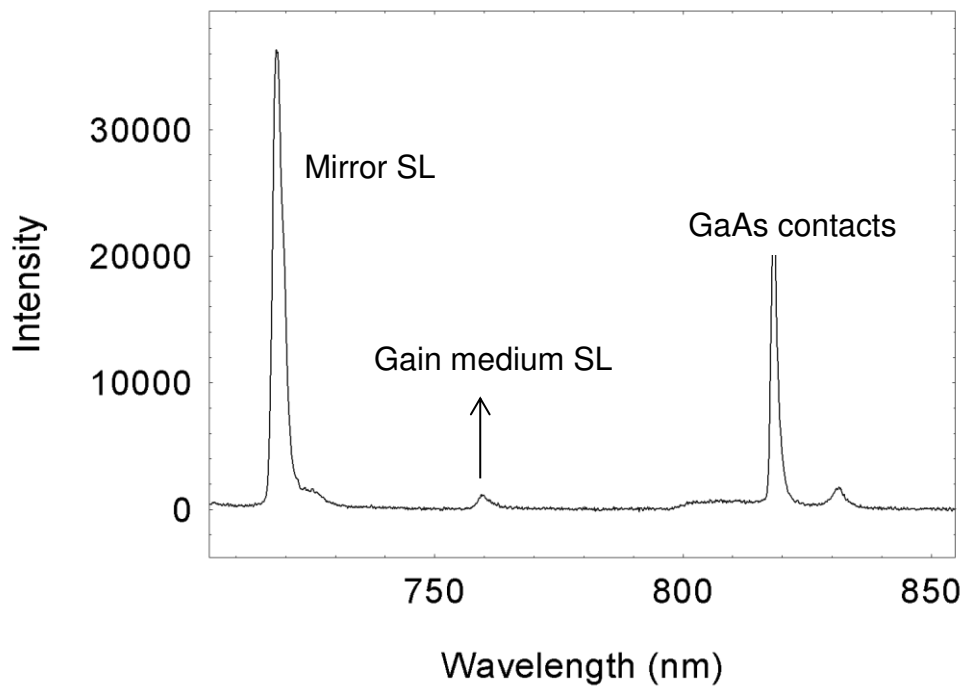


Figure 4.4: The optical resonance of sample MN 685, using laser light with a wavelength of 690 nm. The first interband transition for the mirror SL was centred at 718 nm and for the middle SL centred at 759 nm.

## 4.2 SASER Cavity Characteristics Determined by Pump – Probe Measurements

The characteristics of the SASER cavity were obtained by means of pump-probe reflectivity. Only samples MN 685 and MN 652 had the mirror SL optical resonance in the tuning range of the TSUNAMI laser. Hence the NU 2694 sample was not investigated. Both of these samples had the same cavity structure, the only difference being the doping profile in the gain SL. The measurements of the MN 652 sample included a long scan of the pump-probe reflectivity to determine the cavity round trip time from the reflected cavity modes as well as to accurately determine the frequency of these modes. Short scans were performed on the MN 685 sample to confirm the

frequency of the cavity modes and estimate the actual phonon loss in this cavity.

However, first a brief theoretical background regarding the generation and detection mechanism of pump–probe reflectivity measurements is presented. An overall description of the properties of the SASER cavity of sample MN 685 and NU 2694 is provided at the end.

#### 4.2.1 Generation and Detection

Coherent phonons may be generated and detected in pump–probe experiments by tuning the laser at the optical absorption edge of the SL structure of interest [77, 78]. The interband absorption energy for the SL structures may be determined by PL measurements, as previously explained. Considering the optical generation and detection of coherent phonons in an ideal infinite system, theoretically, the wave number selection rules permit the generation of the zone centre phonon modes (where  $q = 0$ ); and the detection in reflection geometry pump-probe is sensitive to the phonon modes having wavevector  $2k_{\text{laser}}$ .

However, in reality the SL structure is finite and according to a recent paper [79], some degree of violation of the momentum selection rules was possible due to the attenuation of the light as it penetrates into the finite SL structure. Slight absorption of the pump light enabled the experimental observation of all three modes. In [79], it has been shown theoretically how the detection was sensitive to the modes associated with the generation process, leading to the experimentally observed phonon modes in the Fourier spectrum: one zone-centre phonon mode (odd symmetry) and two other phonon

modes at either sides of the first zone centre gap with energy  $q = 2k_{\text{laser}}$ .

Figure 4.5 shows the calculated dispersion curve of the mirror SLs. The blue square represents the zone centre phonon mode at 640 GHz whereas the  $2k_{\text{laser}}$  line intercepts at 594 GHz and 694 GHz, represented by the red circles. Brillouin oscillations may also be detected, indicated by the black circle, with a frequency of around 51 GHz.

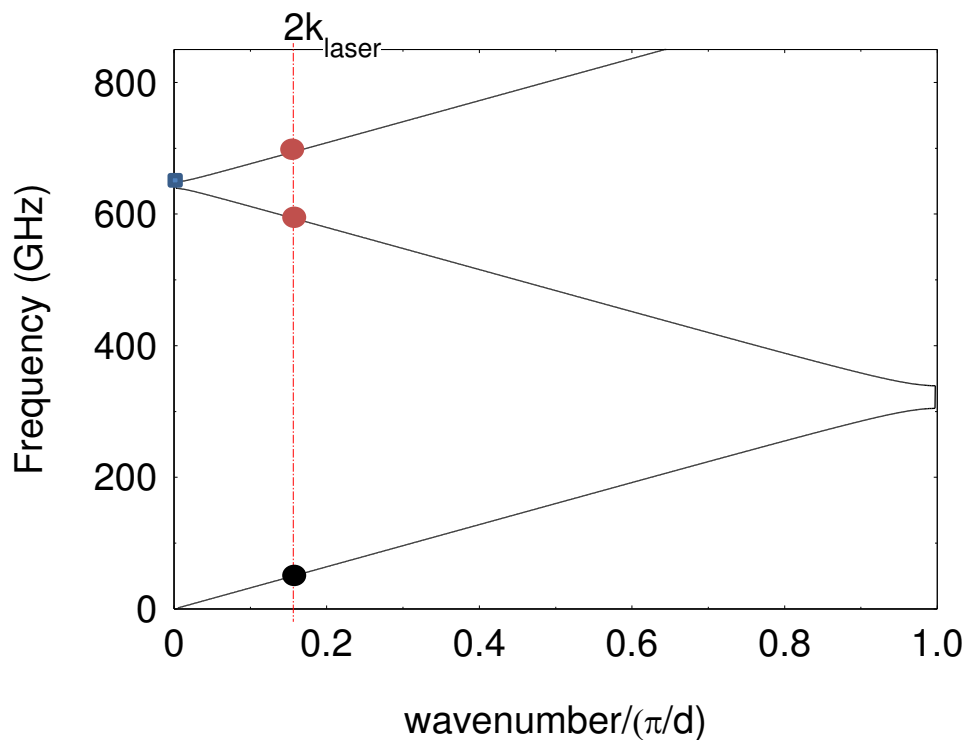


Figure 4.5: The folded dispersion curve for LA phonon modes of the mirror SLs in sample MN 685 and MN 652. The  $2k_{\text{laser}}$  red line at 594 GHz and 694 GHz, represented by the red circles whilst the blue square corresponded to the zone centre phonon mode at 640 GHz. Brillouin oscillations may also be detected, as marked by the black circle.

The laser wave vector ( $2k_{\text{laser}}$ ) may be calculated as

$$2k_{laser} = \frac{4\pi n}{\lambda}, \quad (4.1)$$

where  $n$  is the refractive index of the SL ( taken as 3.5 from [43] ) and  $\lambda$  is the laser wavelength. For a laser with a wavelength of 715 nm, the corresponding  $2k_{laser}/(\pi/d) = 0.16$  ( $d = 8$  nm).

The calculated reflectance of the mirror SLs for this cavity is shown in Figure 4.6. The zone centre phonon modes reflected by the mirror SLs are centred at 644 GHz, where the cavity mirrors are 90% reflecting at one end (40 period SL) and 36 % reflecting at the other end (15 period SL).

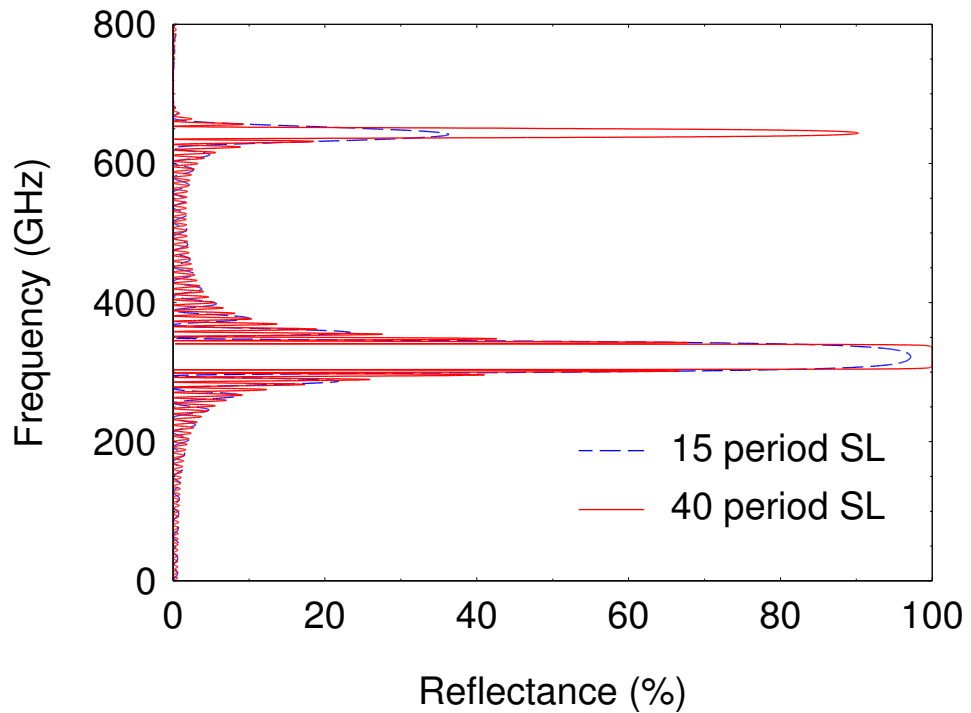


Figure 4.6: The reflectance for the cavity mirrors in MN 685 and MN 652. The zone centre phonon modes reflect 36 % and 90 % for the 15 period and 40 period mirror SL respectively.

The experimental setup and methodology for pump–probe measurements have been described in Chapter 3. The mode–locked Ti:Sapphire laser, with a pump spot of 200  $\mu\text{m}$  was tuned near to the optical resonance of the cavity mirror SL structure. The coherent phonons generated in the mirror SL, by the pump pulse, changes the index of refraction of the SL layers as they propagate through the structure. A probe beam, focused to 50  $\mu\text{m}$  spot in diameter, was then used to measure the temporal change of the transmitted and/or reflected intensity from the sample surface, as illustrated in Figure 4.7.

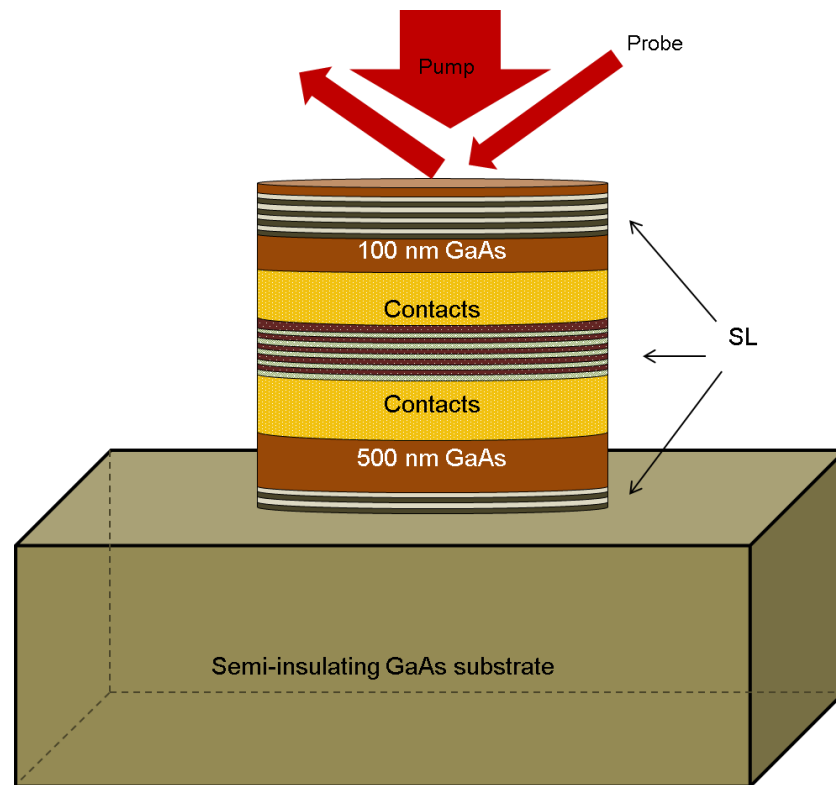


Figure 4.7: Pump-probe technique employed for measuring the characteristics of the SASER cavity. The pump beam was tuned to the optical resonance of the mirror SL structure and a probe beam, with intensity roughly an order of magnitude lower, measures the change in reflectance caused by the phonons generated.



## 4.2.2 Results and Discussion

Figure 4.8 shows the temporal change in reflectivity, detected by the photodiode, for the cavity of the MN 652 sample at 715 nm. High frequency phonon oscillations were observed within the first 200 ps after the arrival of the pump pulse and from 893 ps later. A third, weak, reflection was also detected 1.6 ns after the arrival of the pump pulse.

Figure 4.9 illustrates a zoomed image of the change in reflectivity for the first 130 ps after the arrival of the pump pulse in (a) and from 880 ps in (b). In (a), high frequency phonon oscillations as well as beating effects, possibly due to the interaction of the zone centre modes and modes corresponding to  $2k_{\text{laser}}$ , were observed. Brillouin oscillations were also detected, occurring at a lower frequency of 51 GHz. In (b), however, evidence of frequency beating was no longer noticeable indicating that only a single mode was reflected by the mirror SL. This mode, preferred by the cavity, was able to complete a round trip inside the SASER cavity in 893 ps.

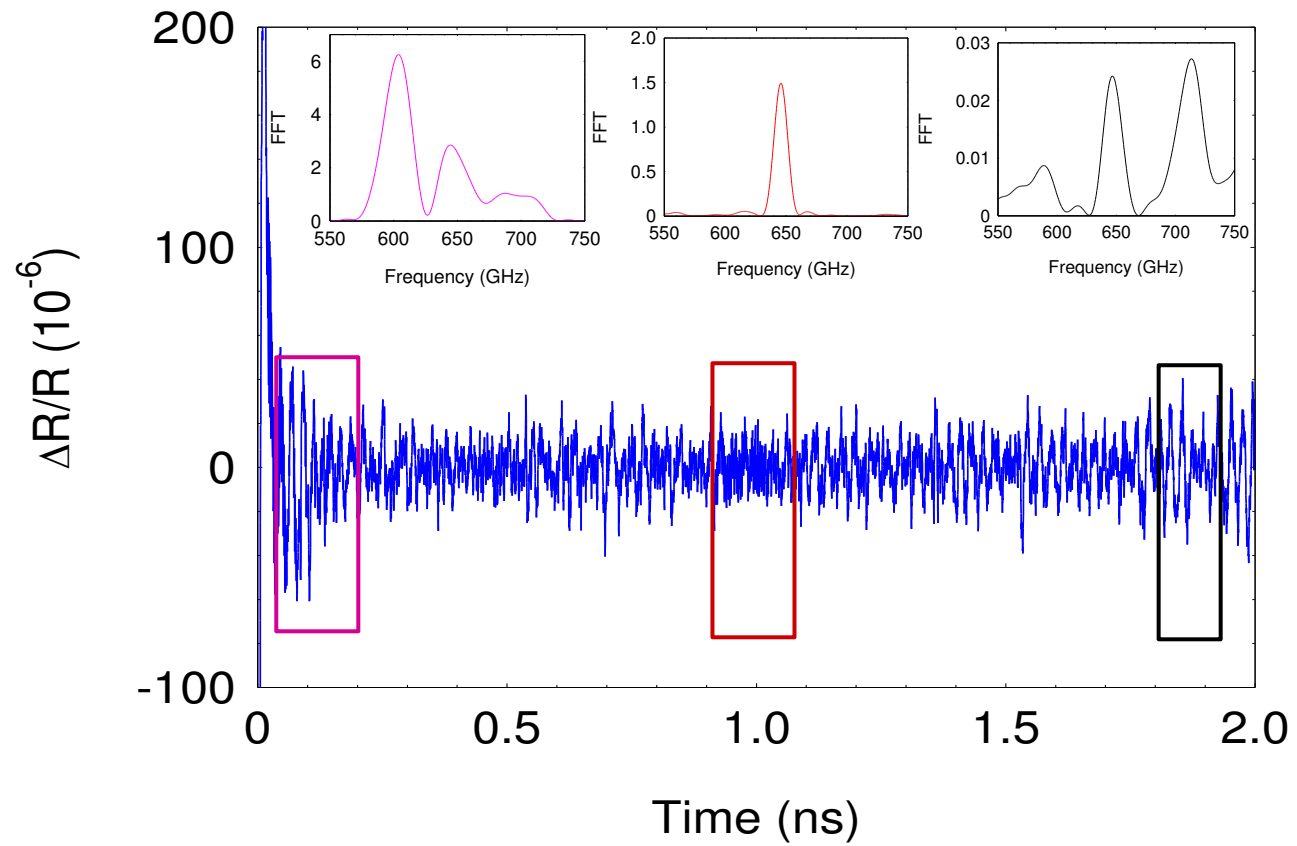


Figure 4.8: The temporal change in reflectivity measured by the probe pulse. The phonon spectrum related to each box is also presented.

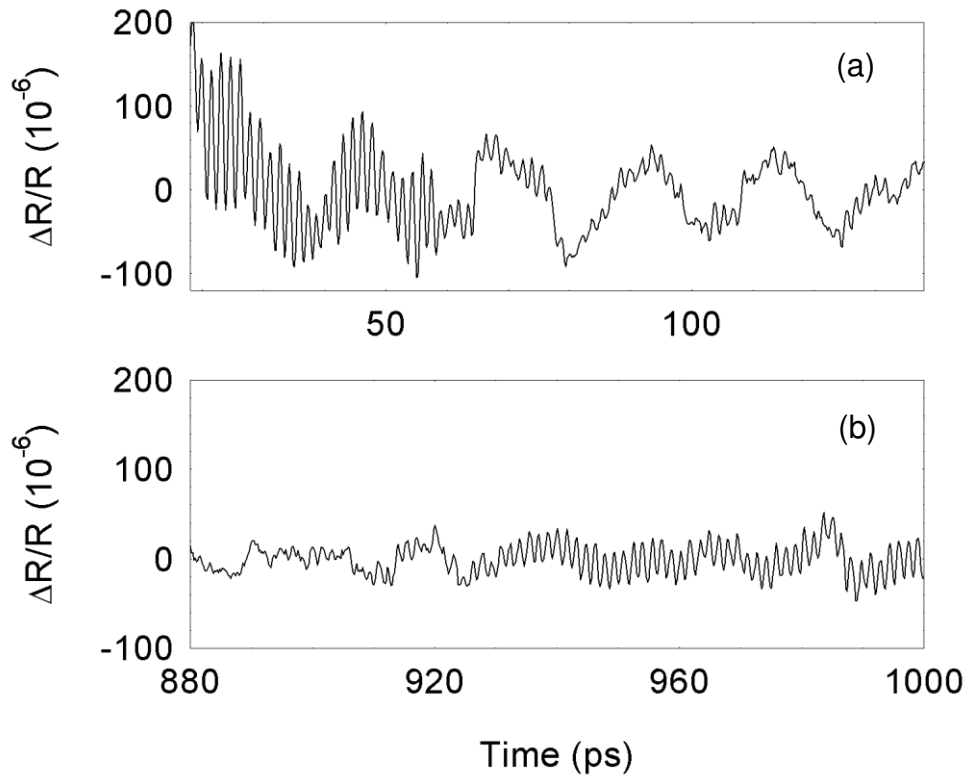


Figure 4.9: (a) Coherent phonon oscillation in a 130 ps time window after the arrival of the pump pulse. Beating effects, observed, may be due to the interaction of the zone centre modes and the  $2k_{\text{laser}}$  modes. The strong low frequency oscillations are possibly related to Brillouin oscillations. (b) The high frequency oscillations were detected for the second time from 893 ps, indicating the phonon mode that was able to complete a round trip inside the cavity.

The contributions to this round trip time are as follows. The cavity was  $2.13 \mu\text{m}$  long, where  $1.935 \mu\text{m}$  consisted of GaAs and the remaining  $0.195 \mu\text{m}$  was the AIAs layers. The speed of sound for LA phonons is  $4730 \text{ m/s}$  and  $5680 \text{ m/s}$  for GaAs and AIAs respectively [52]. Therefore, it is expected that the phonon modes reflected by the mirror SL take  $887 \text{ ps}$  to travel one round trip. As shown in Figure 4.9 (b), the high frequency phonon oscillations start to occur at  $893 \text{ ps}$  after the arrival of the pump pulse. There was an extra  $6 \text{ ps}$  observed experimentally, which may be due to the fact that the phonons

slightly penetrate into the cavity mirror a certain distance before reflecting and travelling back to the other end of the cavity.

The changes in reflectivity observed in Figure 4.6 were analysed by means of Fourier analysis. The Fourier transform of these high frequency phonon oscillations are shown in Figure 4.10 for two different time delays. The time window for the Fourier transform yields a resolution of 10 GHz.

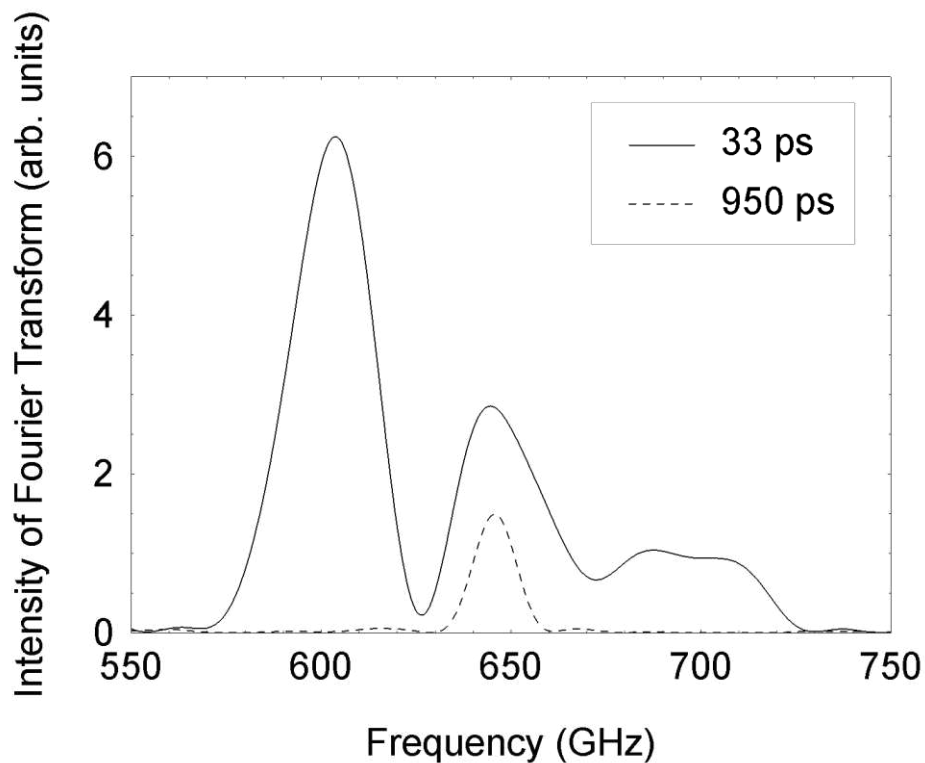


Figure 4.10: The frequency spectrum of the phonon modes detected by the probe pulse at different time delays for sample MN 652. Peaks at 33 ps delay corresponded to phonons at the zone centre ( $q = 0$ ) and  $2k_{\text{laser}}$  whereas only the zone centre phonon mode was present 950 ps later.

At early time delays (33 ps), the Fourier spectrum revealed three frequencies: 604 GHz, 644 GHz, and 684 GHz; representing the zone centre phonon modes and phonons at  $2k_{\text{laser}}$ . Comparing these frequencies with the calculated dispersion curve, in Figure 4.5, the

zone centre frequency was within  $\pm 4$  GHz whereas the  $2k_{\text{laser}}$  frequencies were within  $\pm 10$  GHz which may be due to an uncertainty in the value of the refractive index. However, the calculated reflectance graph in Figure 4.6 shows that the mirror SLs are centred at 644 GHz, which coincided well with the one mode observed at 950 ps (Figure 4.10). This frequency was the only mode out of the three initially observed modes, selectively reflected by the mirror SL and was detected 893 ps later, after completing a cavity round trip. The fact that this mode was observed, even when the SL mirror at one end of the cavity was only 36 % reflecting, does suggest that the cavity is a good candidate for a SASER device.

The actual frequency of the cavity modes in sample MN 685 was determined by means of pump – probe where one of the mirror SLs was optically excited close to its exciton resonance. The effective bandwidth in the data acquisition was improved by employing a shaker to record the phonon oscillations in a 55 ps window, as previously explained in Chapter 3. Figure 4.11 shows the phonon oscillations in the time window of 920 – 975 ps.

Three modes were present at 33 ps, as illustrated in Figure 4.12, with the 645 GHz zone centre phonon mode at the centre and phonons corresponding to  $2k_{\text{laser}}$  at each end. Only one mode was apparent 950 ps later, which corresponded to the zone centre phonon mode. For an excitation wavelength of 714 nm, only 17 % of the initially detected zone centre phonon mode completed a round trip inside the cavity.

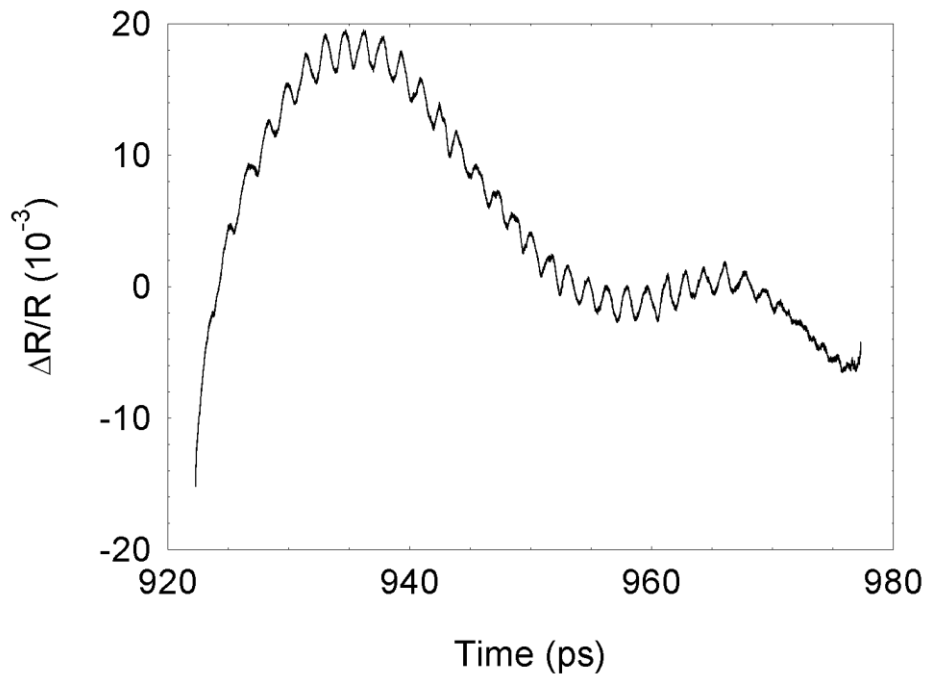


Figure 4.11: Pump - probe reflectivity in a 55 ps window acquired by the DPO oscilloscope, enabling large averaging to provide high signal to noise ratio.

In Figure 4.6, the cavity mirror containing 15 periods was numerically estimated to be 36 % reflecting for zone centre phonon modes using the method described in Chapter 2. The discrepancy in the percentage reflectance of the zone centre phonon modes, observed experimentally, upon completing a round trip is possibly due to additional unaccounted losses, in the calculated reflectance, experienced by these modes. Losses due to scattering were discussed in Chapter 2, revealing that the dominant, most relevant, scattering loss was due to electron–phonon scattering which may occur from the highly doped GaAs contact regions. Using Equation 2.28 from Chapter 2, the electron – phonon scattering length for 644 GHz phonons is estimated to be 29.5  $\mu\text{m}$ .

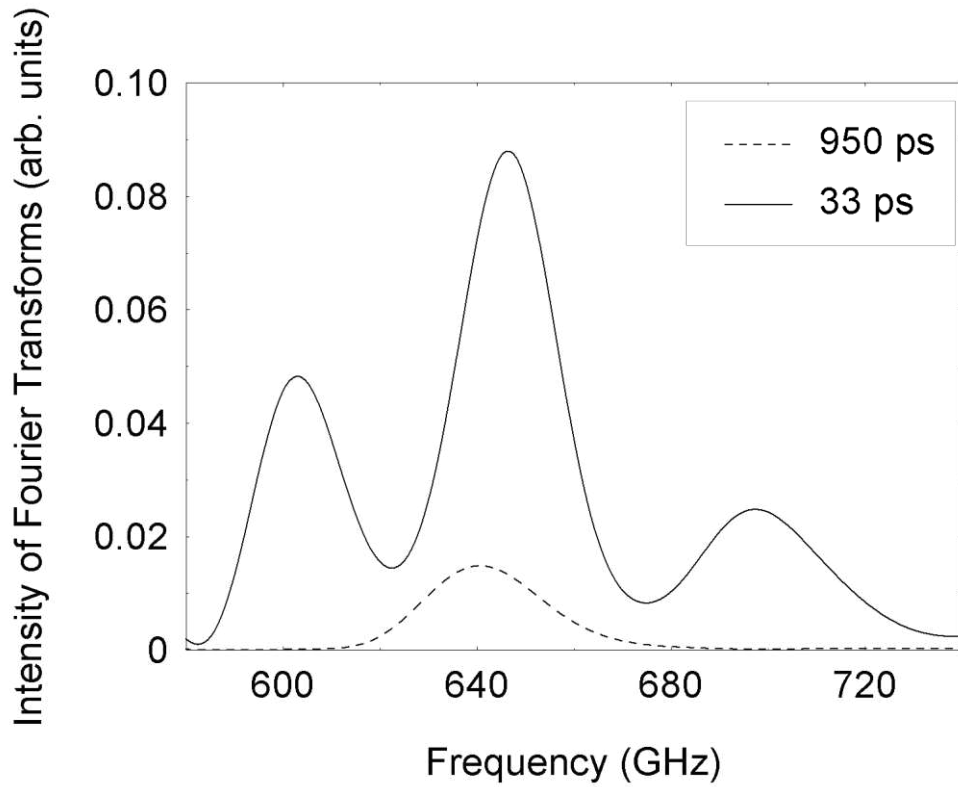


Figure 4.12: Fourier transform of the change in reflectivity in sample MN 685 at an excitation wavelength of 714 nm. The blue solid line represent the frequency of the phonon modes 33 ps after the arrival of the pump pulse and the dotted red line represent the frequency of the phonon oscillations 950 ps later. The height ratio of the zone centre phonon mode at the two time delays is 0.17.

The device, in this pump–probe experiment, was not used as a SASER device, hence, phonon scattering off electrons in the gain medium SL may also provide additional losses as the carrier concentration is only a factor of 10 lower than the doping level of the GaAs contact regions. By including the length of the gain medium (1  $\mu\text{m}$  for one round trip), the corresponding fraction of phonons propagating inside the cavity per round trip (contacts are 1  $\mu\text{m}$  thick each way) is

$$e^{-2kL_s} = e^{-2\left(\frac{3}{29.5}\right)} = 0.82 \quad (4.2)$$

In other words, a further 18 % was lost due to scattering events. This brings the expected reflectance of the zone centre phonons, as calculated in Figure 4.6, down to 18 %. This is in good agreement with the experimentally observed, percentage of phonons detected after one round trip (17 %) and further clarifies the approach in determining the cavity losses.

However, the cavity was designed to highly reflect the zone edge phonon modes, centred at around 325 GHz, as indicated in Figure 4.6. It has been shown that the zone edge phonon modes may be optically generated and detected in a SL [80, 81]. The detection was possible in pump – probe measurements due to coupling of the zone edge phonon mode to the available electrons in the doped SL. However, it was not possible to detect these zone edge modes in the mirror SL as they were nominally undoped. Nevertheless, by analysing the experimentally observed zone centre phonon modes and relating to the theoretical estimates, it was possible to infer the behaviour of the zone edge modes for sample MN 685.

#### 4.2.3 Other Properties of the MN 685 SASER Device

By relating the properties of a SASER cavity theoretically discussed in Chapter 2 to the experimentally observed reflected zone centre phonon modes, it was possible to obtain a prediction on the properties of the SASER device for the zone edge phonon modes.

The zone centre phonon modes have shown the dependence of scattering inside the gain medium. However, when the gain medium is electrically excited, the calculation with regards to the SASER action has already accounted for the electron–phonon interactions inside the gain medium. Therefore, only electron–phonon scattering occurring inside the contact regions will be considered; providing a



scattering loss of 7 % for 325 GHz phonon modes. By recalling Equation 2.30 from Chapter 2, an estimate of the threshold gain for the MN 685 SASER cavity is

$$\gamma_{th} = \frac{\ln\left(\frac{1}{R_1 R_2 \times 0.93}\right)}{2L} = 233 \text{ cm}^{-1}, \quad (4.3)$$

where  $R_1 R_2 = 0.97$  as calculated and shown in Figure 4.6.

As previously mentioned in Chapter 2, a cavity having a threshold gain as small as this would be suitable for the gain medium structure studied in [36, 38] as the gain ( $3600 \text{ cm}^{-1}$ ) is able to overcome the threshold gain and provide means of achieving sustained phonon oscillations inside this cavity.

The lifetime of this cavity, for the zone edge phonon modes, may be estimated alongside with its Q-factor. The round trip time was deduced as 893 ps in Section 4.2.2 and hence, the cavity lifetime may be calculated, using Equation 2.31, as

$$\tau_{cav} = m \times \tau = \frac{-1}{\ln(R_1 R_2)} \times \frac{(\text{round trip length})}{c_s} = 28 \text{ ns} \quad (4.4)$$

Using Equation 2.32, the cavity linewidth was determined as

$$\Delta\nu = \frac{1}{\tau_{cav}} = 35.7 \text{ MHz} \quad (4.5)$$

The Q-factor of this cavity at 325 GHz is then  $9.1 \times 10^3$ . A Q-factor of up to 2400 has been reported for an acoustic cavity made of GaAs/AlAs SLs [44]. A large Q factor indicates a good quality cavity, for which the threshold gain coefficient is low; implying a short time for phonon oscillation to build up time towards steady state.

### 4.3 The SASER cavity of NU2694

The NU 2694 SASER device was designed with slight modification in the period of the first mirror SLs, so that the first zone edge phonon modes are at a higher frequency. Similarly, estimations with regards to the threshold gain, the cavity lifetime and Q-factor for the NU 2694 SASER device may also be obtained. Figure 4.13 shows a calculation of the reflectance for the mirror SL in the NU 2694 SASER device. Just like the case for the MN 685 SASER cavity, the reflectance for the zone edge frequency, centred at 646 GHz, was 97 % and 100 % for the output coupler and high reflector cavity mirrors respectively.

The lifetime and linewidth of the cavity would be the same as in the case of MN685, as the cavity has the same length and the same mirror reflectance. The Q-factor however, is  $1.8 \times 10^4$  for the 646 GHz phonons. A higher Q-factor was obtained for this cavity due to the fact that it operates at a much higher frequency than sample MN 685.

However, the phonon–electron scattering length for 646 GHz, calculated using Equation 2.28, was 29  $\mu\text{m}$  corresponding to an additional loss of 13 % from scattering events. The threshold gain for this cavity at 646 GHz, using Equation 4.3, is then  $509 \text{ cm}^{-1}$ . Although the threshold gain for the NU 2694 SASER device is much higher, this cavity would still work with the same gain medium as used in [36, 38], just like the case for the MN 685 SASER device. By exciting the zone edge phonon modes electrically, coherent phonon oscillations may be achieved in this device.

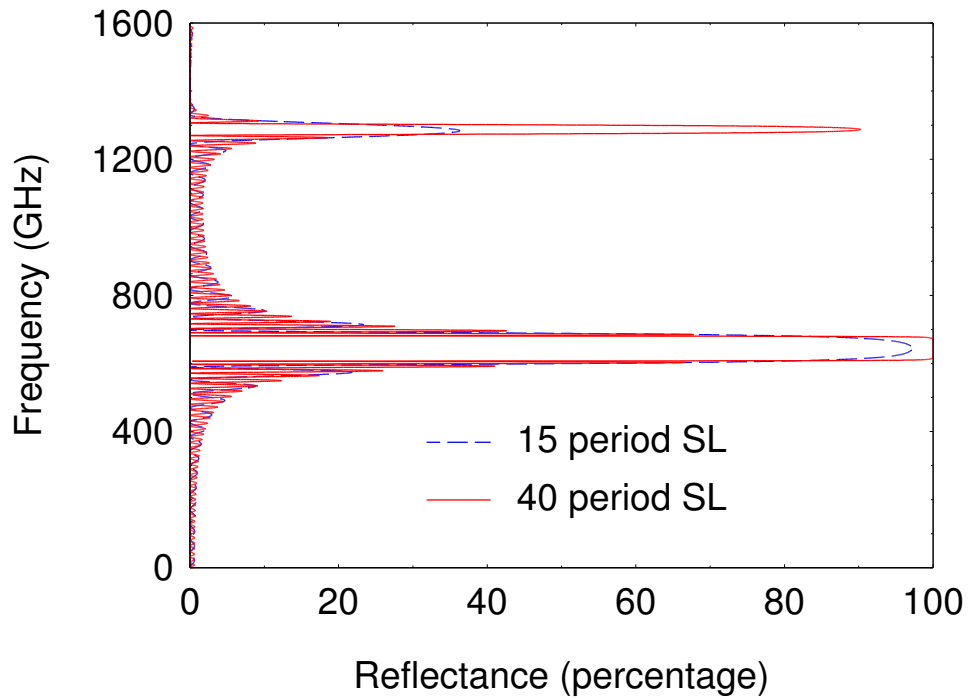


Figure 4.13: Reflectance of the mirror SLs in sample NU 2694. The zone edge modes centred at 650 GHz is 97 % reflected by the 15 period SL and near 100 % from the 40 period SL.

#### 4.4 Conclusion

In conclusion, this chapter has provided specific results pertaining to the optical characteristics of each SL, in both samples, leading to characterising the SASER cavities by means of pump–probe reflectivity measurements. Fundamental properties of the SASER cavities such as the phonon round trip time, the mode of the cavity and the cavity lifetime was determined. A summary of the characteristics of the cavities is described in Table 4.1.

	MN 685		NU 2694
	325 GHz	646 GHz	646 GHz
Round trip time (ps)	893		893
Q-factor	$9.1 \times 10^3$	$1.8 \times 10^4$	$1.8 \times 10^4$
Scattering losses	7 %	13 %	13 %
$\gamma_{th}$ (cm <sup>-1</sup> )	233	398	509

Table 4.1: Summary of the parameters of each SASER device, for different operating frequencies.

## **CHAPTER 5**

# **DYNAMICS OF A SASER OSCILLATOR – THE BUILD UP OF PHONON OSCILLATIONS**

This chapter describes measurements of the dynamics of SASER oscillator devices made from sample MN 685 and NU 2694. The build-up of phonon oscillation was investigated by means of bolometric experiments and the results were analysed and compared with the theoretical model, derived in Chapter 2, to extract information regarding the SASER gain and the output power.

The characteristics of the acoustic cavity were determined by means of pump–probe reflectivity experiments described in Chapter 4. By having an electrically pumped SL gain medium inside the acoustic cavity, as proposed in this thesis, it was possible to achieve coherent phonon oscillations if the threshold gain condition was achieved. The coherent phonons generated by stimulated emission, that are reflected by the cavity mirrors, build up in intensity with each cavity round trip before reaching steady state intensity. The intensity of the LA phonons initially rose exponentially with time and eventually reached a steady state, as described by Equation 2.42, which will be recalled in later sections of this chapter.

The build-up of the intensity of the oscillations is theoretically expected to occur when the gain spectrum, which has a peak close to the Stark splitting energy, is tuned, by application of bias, to coincide with the energy of the oscillating cavity modes. As the

output coupler mirror at one of the cavity is partially transmitting, a monochromatic beam of acoustic emission can escape the oscillator.

A thorough investigation into the dynamical behaviour of the cavity will be discussed here. However, first the current–voltage (IV) characteristics of each SASER device will be presented.

## 5.1 Transport measurement of the devices

The setup for obtaining the IV graph for the gain medium SL was explained in Section 3.4, and the measurements were conducted at a temperature of  $\sim 2$  K, the same temperature used in all bolometer experiments. Figure 5.1 shows the IV characteristics for the NU 2694 SASER device under electrical bias.

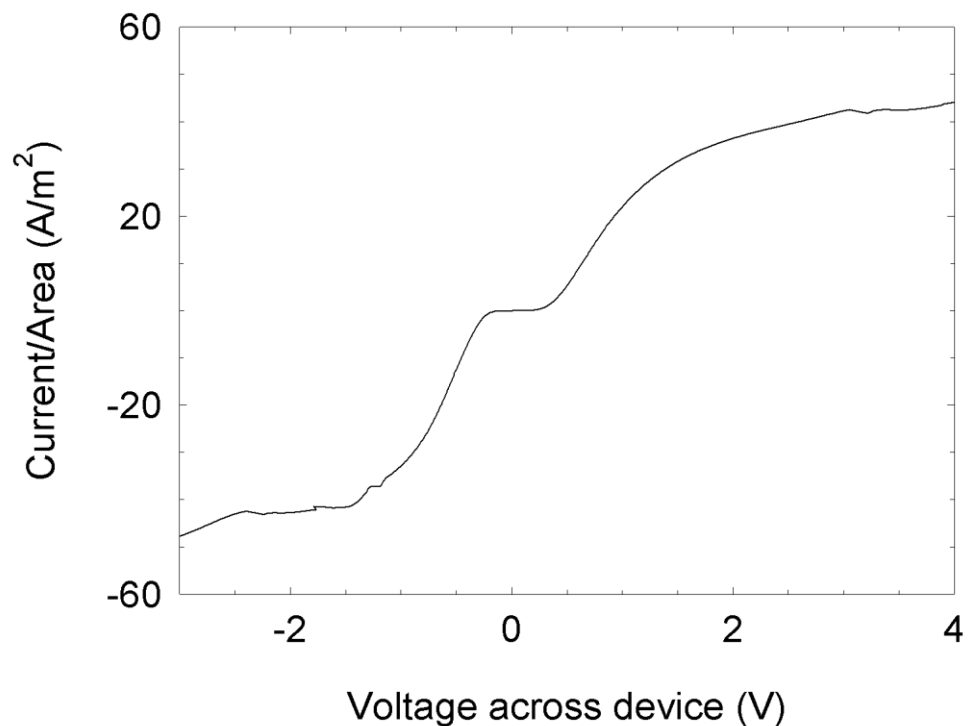


Figure 5.1: IV characteristics for NU 2694 SASER device. Due to the low doping in the SL, the resistance of this device was relatively high (in the  $k\Omega$  range). The IV shows characteristics of a typical biased SL.

The device was slightly asymmetric at zero which may be due to the different annealing temperatures of the contacts at each end of the SL. A small bias was needed to align the Fermi level in the contacts with the quasi Fermi level of the first quantum well, resulting in zero conductance below the threshold value [82]. This threshold voltage was smaller under negative bias compared to, at positive bias. Since a larger threshold bias implies a larger amount of background power dissipated in the structure, resulting in heating the device, the negative bias range was used when conducting all experiments. The corresponding threshold voltage was - 200 mV.

The miniband width for this gain medium SL was estimated to be  $\sim 1$  meV [83], corresponding to - 50 mV across the device. Therefore, the gain medium SL requires negative biases greater than 250 mV to put it into the 'Stark Ladder' state where tunnelling of electrons is via hopping conduction. The electrons hop from one well to the other by either absorbing or emitting a phonon with the energy of the Stark splitting,  $\Delta$  ( $=\hbar\omega$ ) [35]. This occurs over most of the monotonically increasing region of the IV curve.

The IV trace showed structure for negative biases greater than 1.2 V due to charge building up in the quantum wells. The current, in this region, oscillates with bias due to the formation of electric field domains; giving rise to regions of negative differential conductance (NDC) [82]. To avoid issues with these domains, the range of biases applied to the SASER device during experiments was kept at below - 1.2 V, where the device was operating in the Wannier-Stark ladder regime.

The IV characteristics for the MN 685 SASER device are shown in Figure 5.2, also at 2K. The gain medium SL had an order of magnitude higher doping concentration compared to the NU 2694

SASER device, and the GaAs buffer layer between the contacts and the gain medium SL was gradually doped to allow additional current flow from the contacts. The resistance of the MN 685 SASER device was, therefore, much smaller and there is no threshold.

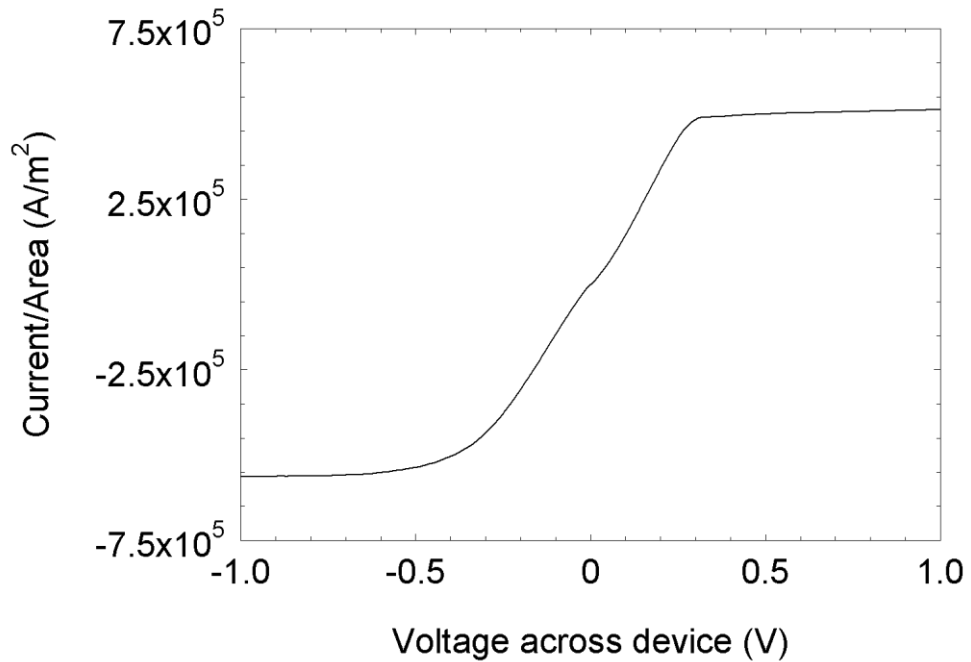


Figure 5.2: IV characteristics of the MN 685 SASER device. A linear region from zero, followed by regions of NDC are typical characteristics of a biased SL.

The IV curve for this device, as in Figure 5.2, showed nominal characteristics of a SL under bias. The device showed ohmic behaviour at low biases and transport began as soon as bias was applied. The Wannier Stark regime would commence at a bias voltage of - 50 mV across the SL. Above 310 mV, a non – linear and oscillatory behaviour of the current with increasing bias, due to NDC, was observed.

The resistance of the SL for a 400  $\mu\text{m}$  device was 19  $\Omega$ , at 300 mV, and typical contact resistance is of a few ohms. Hence, for the MN 685 SASER device, not all of the applied bias is dropped across the



SL and the small amount of voltage dropped across the contacts may need to be taken into account when considering the results in the later sections of this chapter.

## 5.2 Bolometric detection of the phonon flux

A bolometer (bolometer 1) was fabricated on the reverse side of the grown substrate and aligned to be directly opposite the SASER device in both samples, as described in chapter 3. For the MN 685 SASER device, a second bolometer (bolometer 2) was also fabricated on the reverse side of the grown substrate at an angle of  $57^\circ$  from the normal to the device.

An illustration of the experimental scheme is shown in Figure 5.3. The setup and experimental procedures for the electrical bolometer measurements are as described in Section 3.6.2. An electrical (pump) pulse was applied to the device, injecting electrons into the gain medium SL. This generates phonons at a frequency dependent on the amplitude of the applied pulse. The phonons propagated into the substrate, reaching the bolometer after a time  $t_S/c_S$  where  $t_S$  is the thickness of the GaAs substrate and  $c_S$  is the speed of sound in GaAs. The electromagnetic pick up of the pump pulse was cancelled by subtracting the positive and negative bolometer bias traces.

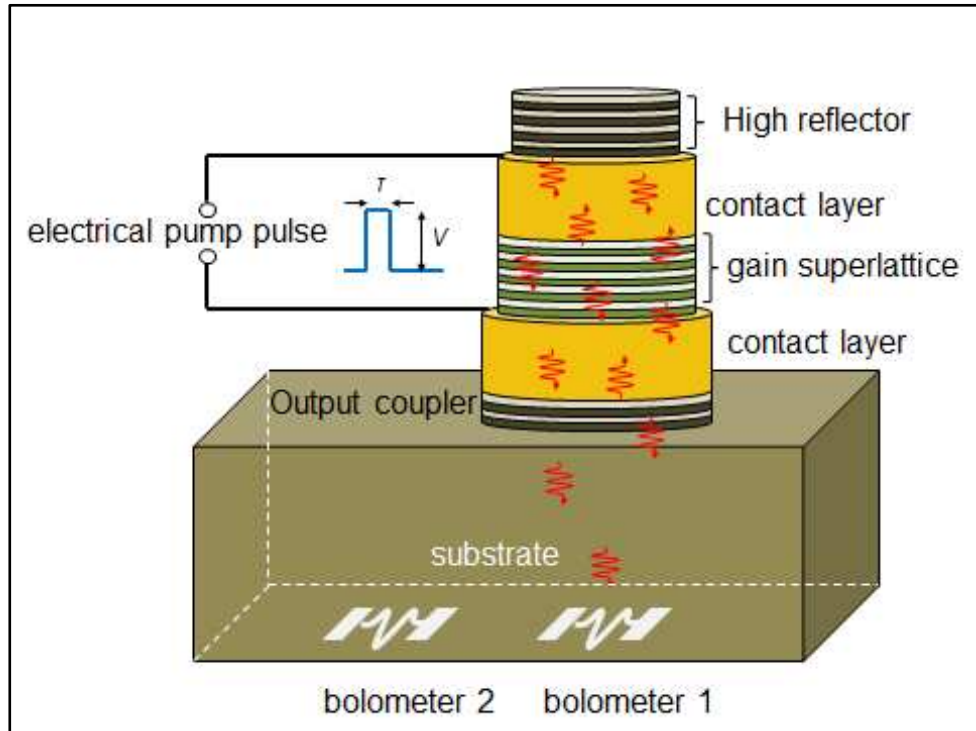


Figure 5.3: Schematic diagram of the experiment performed on the device for both SASER devices. An electrical pump pulse was sent to the device to provide bias through the gain medium SL. Phonons generated in the gain medium travels through the substrate and the superconducting bolometer provides a response as soon as any phonons arrived.

As described in Section 3.6, the bolometer was held at the lower end of the superconducting transition to provide a measurable change in resistance as a function of temperature. Therefore, the bolometer detects any phonons or heat flux incident upon it which means that the detected phonons are superimposed on a thermal background. However, since the bolometer was operating at a temperature of  $\approx 2$  K, the thermal background energy,  $k_b T$ , is much less than the emitted phonon energy,  $\hbar\omega$  (for hundreds of GHz phonon frequencies); significantly reducing the thermal background. To reduce the background even further, the analysed signal was normalised to the total power dissipated across the device. If there is an increase in emission of LA phonons towards bolometer 1, as

expected if SASER oscillation occurs, then a significant peak will appear when the cavity mode phonon energy matches the Stark splitting energy.

The power dissipated in the device,  $P_d$ , was calculated by considering the forward and reflected voltages of the applied pump pulse, passing through the cables with an impedance of  $50 \Omega$ , as follows

$$P_d = \frac{V_f^2 - V_r^2}{50}, \quad (5.1)$$

where  $V_f$  and  $V_r$  denotes the forward and reflected voltages respectively.

It is also essential that the bolometer signals analysed were not affected by bolometer saturation. A clear 'topping out' of the signal was observed for the MN 685 SASER device at the bolometer saturation point, as shown in Figure 5.4. As saturation occurred for applied biases from 212 mV (at 3 dB attenuation), only signals obtained below 212 mV were used throughout all analysis of results from this device. In contrast, the NU 2694 SASER device had much smaller currents flowing through the device and the maximum power dissipated was below the levels that would cause bolometer saturation. Hence, bolometer saturation issues were avoided, in this device, for all pump amplitudes.

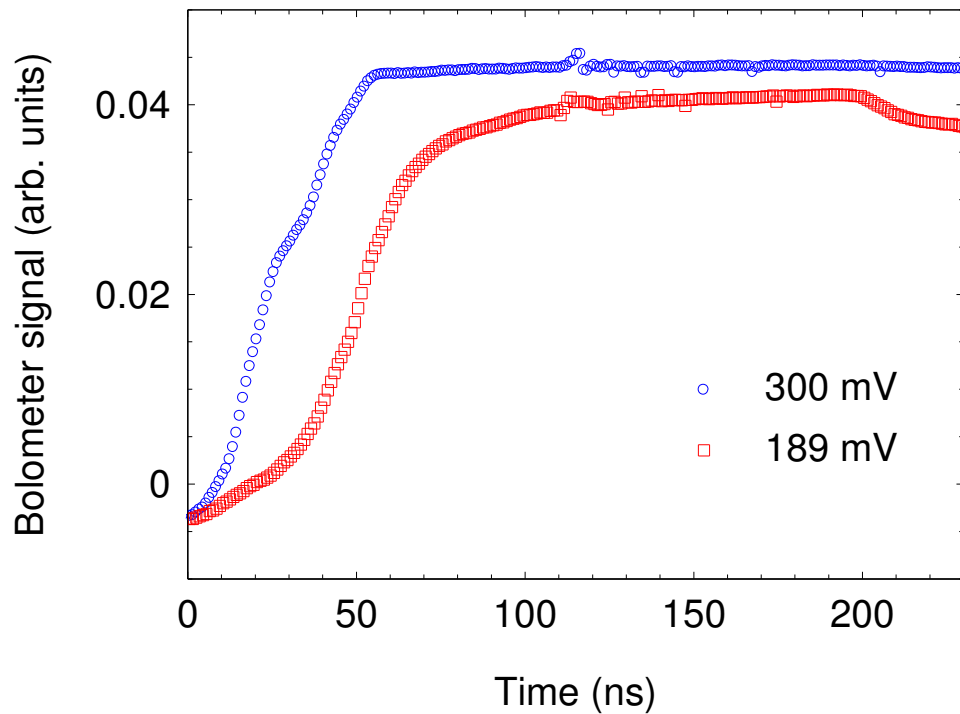


Figure 5.4: Clear limiting of the maximum signal was observed for the bolometric response at pump amplitudes above 212 mV, as shown by the circles. The squares represent the bolometric signal for pump amplitude of 189 mV, where the signal is not saturated, for comparison.

Results from bolometer 1 will be the main subject of discussion here whereas results pertaining to bolometer 2 will be reviewed towards the end of this chapter.

### 5.3 Results from the NU 2694 SASER device

Firstly, phonon build up was studied in the NU 2694 SASER device. The pulsed bias was provided by a pulse generator set to an amplitude of 1 V, and the bolometric response was recorded for switched attenuation settings between 10 and 30 dB (corresponding

to pump amplitudes between 316 mV and 31.6 mV). A typical bolometer trace is shown in Figure 5.5 for 316 mV pump amplitude.

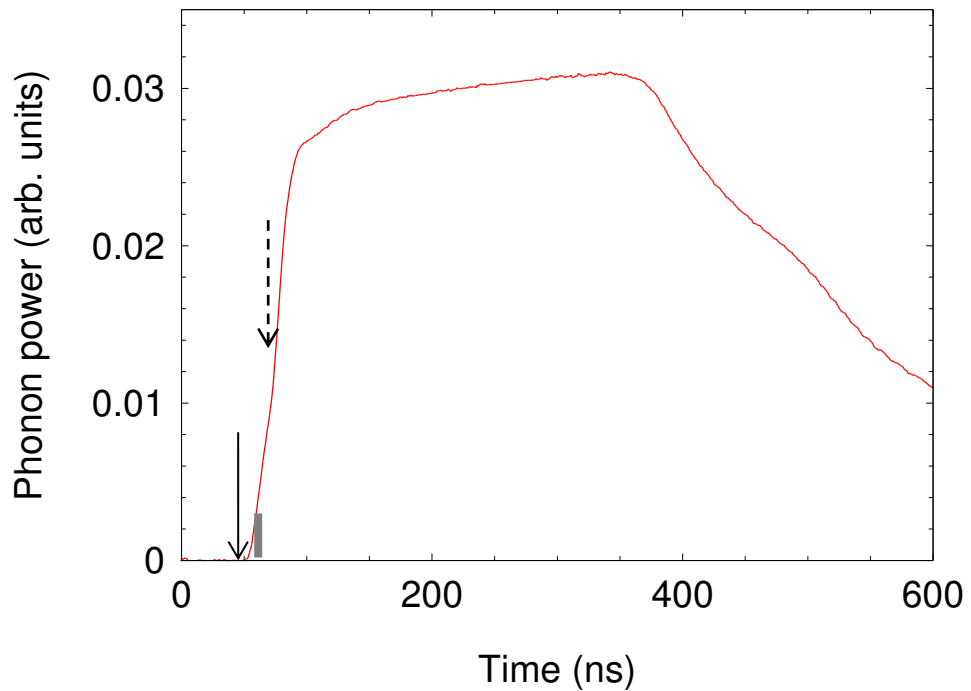


Figure 5.5: Phonon signal obtained from a superconducting Al bolometer directly opposite the NU 2694 SASER where a 300 ns pump pulse, at 316 mV, was applied to the device. The zero time indicated the time at which the electrical bias pulse turned on and the LA phonons were detected 50 ns later (solid arrow), followed by the TA phonons travelling at a slower sound velocity (dashed arrow). The shaded region represents an integrated portion of the bolometer signal across 5 ns.

The substrate of this sample was polished to  $222 \pm 1 \mu\text{m}$  thick and the cavity was  $2.13 \mu\text{m}$  long. The LA phonons travel at  $4730 \text{ ms}^{-1}$  and take  $47 \pm 1 \text{ ns}$  to reach the bolometer. Hence, the phonon signal observed at  $50 \pm 1 \text{ ns}$ , in Figure 5.5, was attributed to the arrival of the LA phonons. The LA phonons signal would then build up in intensity before reaching steady state (denoted by the flat region in Figure 5.5). The small kink in the bolometer rising edge (indicated by

the dashed arrow), at  $67 \pm 1$  ns, was ascribed to the TA phonons, travelling at a velocity of  $3350 \text{ ms}^{-1}$ .

To analyse the temporal increase in phonon power, the bolometer signal was integrated across 5 ns windows, as indicated by the shaded strip in Figure 5.5, where the integrated signal gives a value proportional to the phonon flux at the time the window is centred on.

Figure 5.6 shows the normalised phonon flux measured by the bolometer in 5 ns windows starting at time  $t$  after the arrival of the first LA phonons as a function of pump amplitude. The LA phonons peak at pump amplitude of 345 mV, building up to steady state in 185 ns. The device threshold, as determined by the transport measurements, was around 200 mV. Therefore the peak in power corresponded to a Stark splitting energy of

$$\frac{\text{voltage drop}}{\text{SL period}} = \frac{345 - 200}{50} = 2.9 \text{ meV}. \quad (5.2)$$

According to the theory, as described in Section 1.3, amplification starts to occur when the Stark splitting energy matches the phonon energy and would peak at a slightly higher Stark splitting energy [4]. The phonon energy corresponding to the frequency of the oscillating cavity modes, at 646 GHz, was calculated as 2.67 meV. Hence, the peak in the LA phonon power, observed in Figure 5.6, suggests that the increase in phonon power was due to the amplification of the 646 GHz LA phonons.

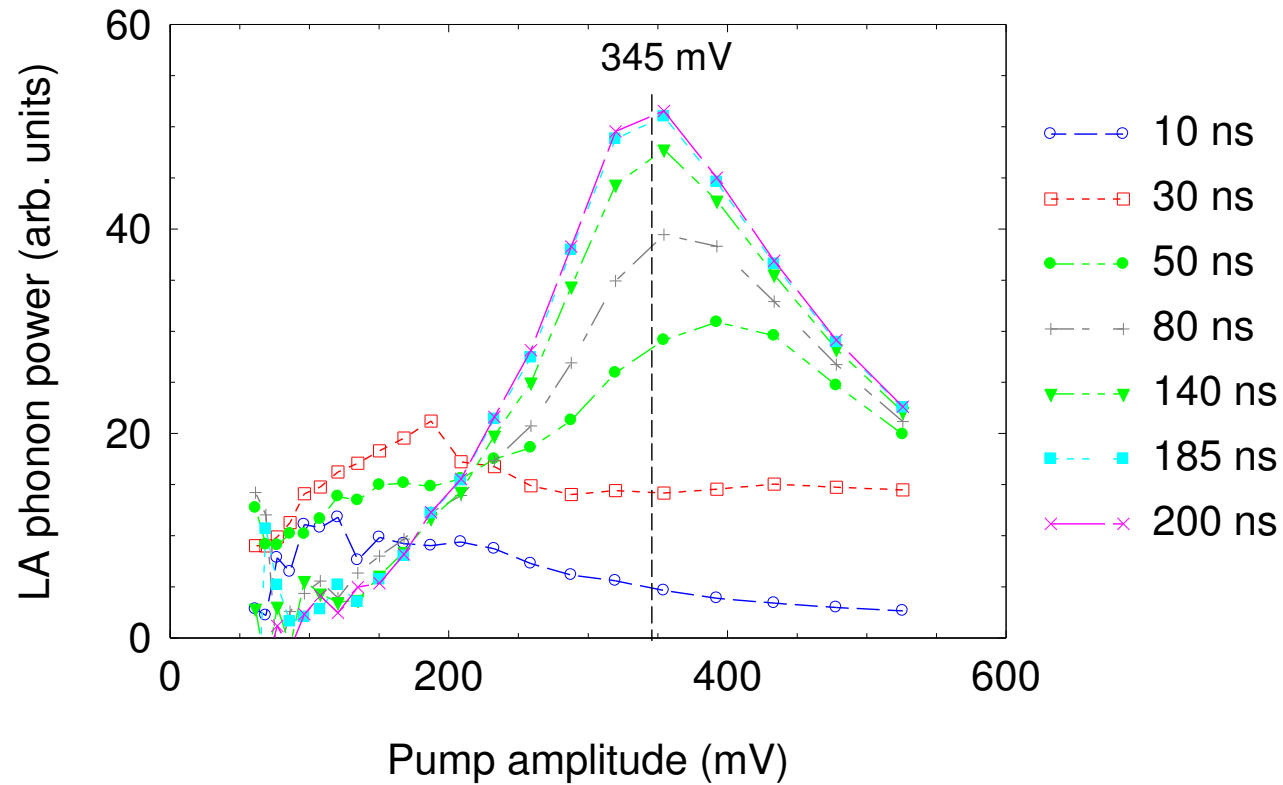


Figure 5.6: The normalised phonon power for a range of pump amplitudes for the NU 2694 SASER device. An increase in phonon power was observed at small pump amplitudes due to a capacitive coupling effect and at longer times, a distinct peak was observed at around 345 mV. The height of the peak no longer increases after 185 ns, indicating the phonons has reached steady state intensity for 345 mV pump amplitude.

The broadness of the LA phonon power peak may be attributed to the large number of modes supported by the cavity. As calculated in Section 4.4, a total of 43 modes separated by 1.1 GHz fall in the reflectance band of the cavity mirrors centred at a frequency of 646 GHz. Slight fluctuations in the growth of the mirror SLs may also broaden the reflectance band and hence allow more modes to reflect and build up in the cavity. Furthermore, disorder in the well widths and doping of the gain medium SL may provide a much larger phonon increment across a wider range of Stark splitting [38].

However, the rising edge of the bolometer trace at longer times, as shown in Figure 5.5, is comprised of both the LA and TA phonons. Therefore, the normalised phonon power illustrated in Figure 5.6 contains acoustic components of the LA and TA. It was important, therefore, to clarify that the phonon build up is primarily attributed to the LA phonons. Another possibility is that the signal obtained from the bolometer may be entirely due to the time constant of the detection scheme; effectively integrating the signal from the long applied pulse. The rate of this, ‘trivial’, growth of the bolometer signal, towards steady state, is associated with the sample geometry and instrumentation response times and is always be present in the system. In both cases, the growth of the bolometer signal and TA phonons may be extrapolated by analysing the short pulse response from the bolometer at low biases where amplification is not taking place. The bolometer signal may be expressed as a temporal convolution as

$$I_{V < V(t)}(t) \sim \int_{-\infty}^t I_0(t') V(t - t') dt', \quad (5.3)$$

where  $I_0(t)$  is the bolometer signal for a narrow excitation pulse at the SL and  $V(t)$  is the temporal evolution of the excitation pulse. The



bolometer signal,  $I_0(t)$ , includes the spontaneous phonon emission rates, the geometrical factors due to the size of the detector and the phonon source that provides different time of flights for the phonons, and the finite response time for the bolometer and electronics. If the result is different to the result shown in Figure 5.5 then it indicates that the build of signal could be due to SASER action.

However, due to the undoped GaAs spacers situated at each end of the gain SL, which behaved as coupling capacitors for the applied bias pulse, the signal was distorted at low pump amplitudes hence making it difficult to separate the bolometer response and contribution of the TA phonons to the signal. This effect is explained in Figure 5.7 which is analogous to a common series CR electrical circuit. The pulse applied to the device has a sharp rise up to the set voltage,  $V$ , and has a sharp fall at the end of the pulse (in this case 300 ns long). The current flows through the device as the capacitors (GaAs spacer) charge and discharge at the rising and falling edge of the applied pulse.

The current through the device,  $I(t)$ , as explained in a conventional CR circuit is [84]

$$I(t) = \frac{V}{R} e^{-\frac{t}{\tau}}, \quad (5.4)$$

where  $V$  is the applied voltage,  $R$  is the resistance of the SL between the GaAs spacer and  $\tau = RC$  is the associated time constant (or relaxation time).

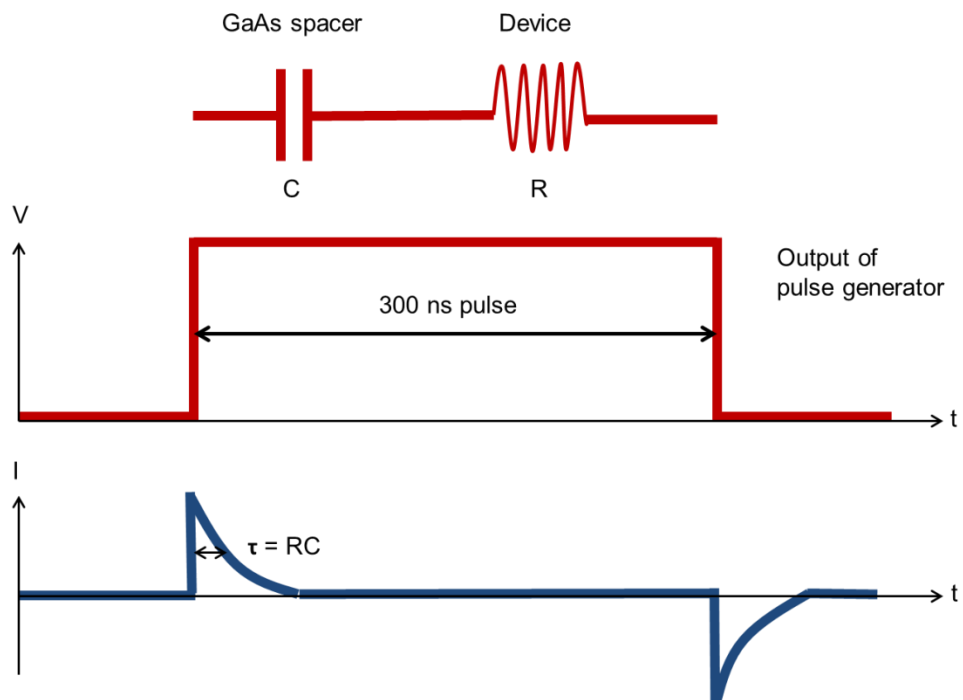


Figure 5.7: Representation of the capacitive coupling effect from the contacts as an electrical pulse was applied to the device. Charge builds up in the contact regions at the rising and falling edge of the pump pulse, generating LA and TA phonons as a burst of current flowed through the device.

The two pulses of current passing through the device at the start and end of the applied bias pulse give rise to the LA and TA phonons as shown in Figure 5.8. For biases below device threshold, almost no steady current passes through the SL (current in the order of nA) and the resistance was very high. However, the bolometer detected the LA and TA phonons at the beginning and end of the applied pulse due to the capacitive coupling effect explained above. Due to this effect, further study regarding phonon build up in the SASER cavity was unfeasible as it was not possible to determine the influence of the TA phonons in the overall signal and to fit the rising edge of the signal to Equation 2.42.

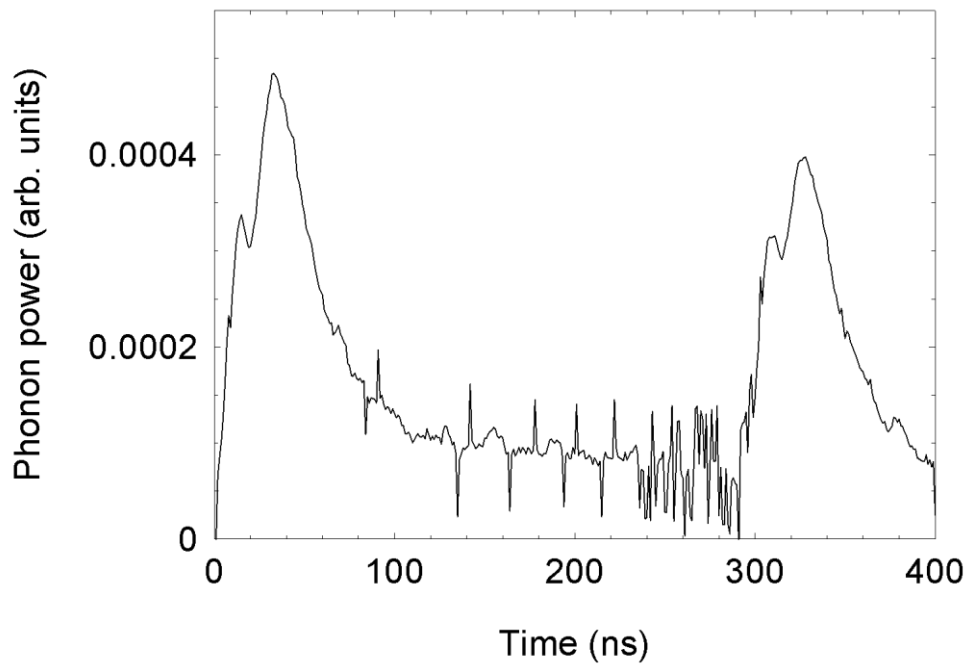


Figure 5.8: The bolometer trace taken at 23 dB (corresponding to pump amplitude of 135 mV) shows the LA phonons arriving at zero time followed by the TA phonons 20 ns later. After 300 ns, the bolometer detects the LA and TA phonons for the second time as the pulse ends.

To avoid the issue of capacitive coupling and obtain further evidence of LA phonon build up in the SASER cavity, a new device was developed in which the GaAs buffer layer, situated between the contacts and the gain medium SL, was gradually doped during the growth process: The MN 685 SASER device. Results obtained using this device are presented and discussed in the following section.

#### 5.4 Results from the MN 685 SASER Device

The MN 685 SASER device was studied by applying a 300 mV electrical pump pulse and recording the bolometric response between 3.5 and 20 dB attenuations (corresponding to pump

amplitudes between 200 mV and 30 mV. The device was ohmic from zero applied bias, as shown in Figure 5.2, and the bolometer traces show no indication of the capacitive coupling effect at low biases as previously observed with the NU 2694 device. Figure 5.9 show the signal detected by the bolometer at pump amplitude of  $\sim 190$  mV attained at different pulse durations.

The MN 685 sample was  $370 \pm 10$   $\mu\text{m}$  thick and the grown layers were  $2.6$   $\mu\text{m}$  thick. Therefore the LA phonons take  $80 \pm 1$  ns to arrive at the superconducting bolometer, followed by the TA phonons at  $110 \pm 4$  ns after the electrical pulse reached the device. The arrival times of all components agreed reasonably well with the observed bolometer traces shown in Figure 5.9.

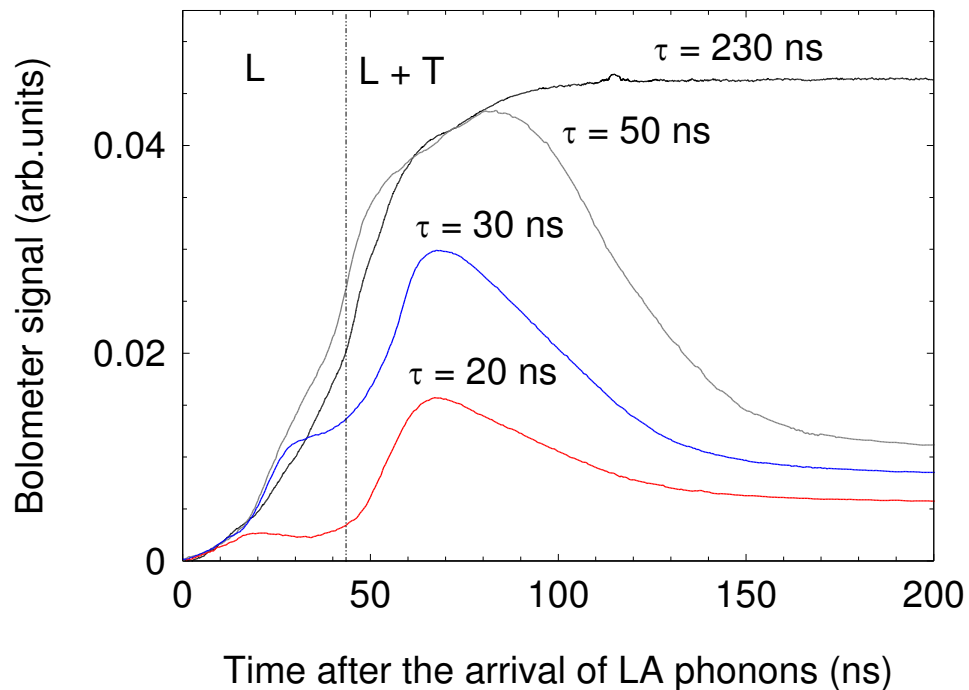


Figure 5.9: The bolometric responses for several different pulse durations at pump amplitude of 190 mV. The zero time indicates the arrival of the LA phonons followed by the TA phonons 50 ns later, represented by the dotted line. As a much longer pulse was applied, the intensity of the LA phonons kept growing even after the TA phonons arrived.

By varying the pump pulse duration, it was possible to observe how the LA phonons evolved with time. Initially they grew exponentially with time and continued increasing even after the arrival of the TA phonons. Steady state intensity was reached by 80 ns, as shown by the 230 ns bolometer trace.

Figure 5.10 shows the normalised integrated phonon signal in 5 ns windows starting at time  $t$  after the arrival of the first LA phonons as a function of pump amplitude. A peak appeared at 125 mV as the phonon oscillation, at this pump amplitude, reached steady state by 120 ns. The frequency of the LA phonons that would, theoretically, build up inside this cavity was estimated, using the method in Chapter 4, to be at  $325 \pm 15$  GHz and peaks at a Stark splitting energy above  $1.34 \pm 0.06$  meV. The peak at 125 mV, as observed in Figure 5.10, corresponded to a higher Stark splitting energy, of 2.5 meV, as expected.

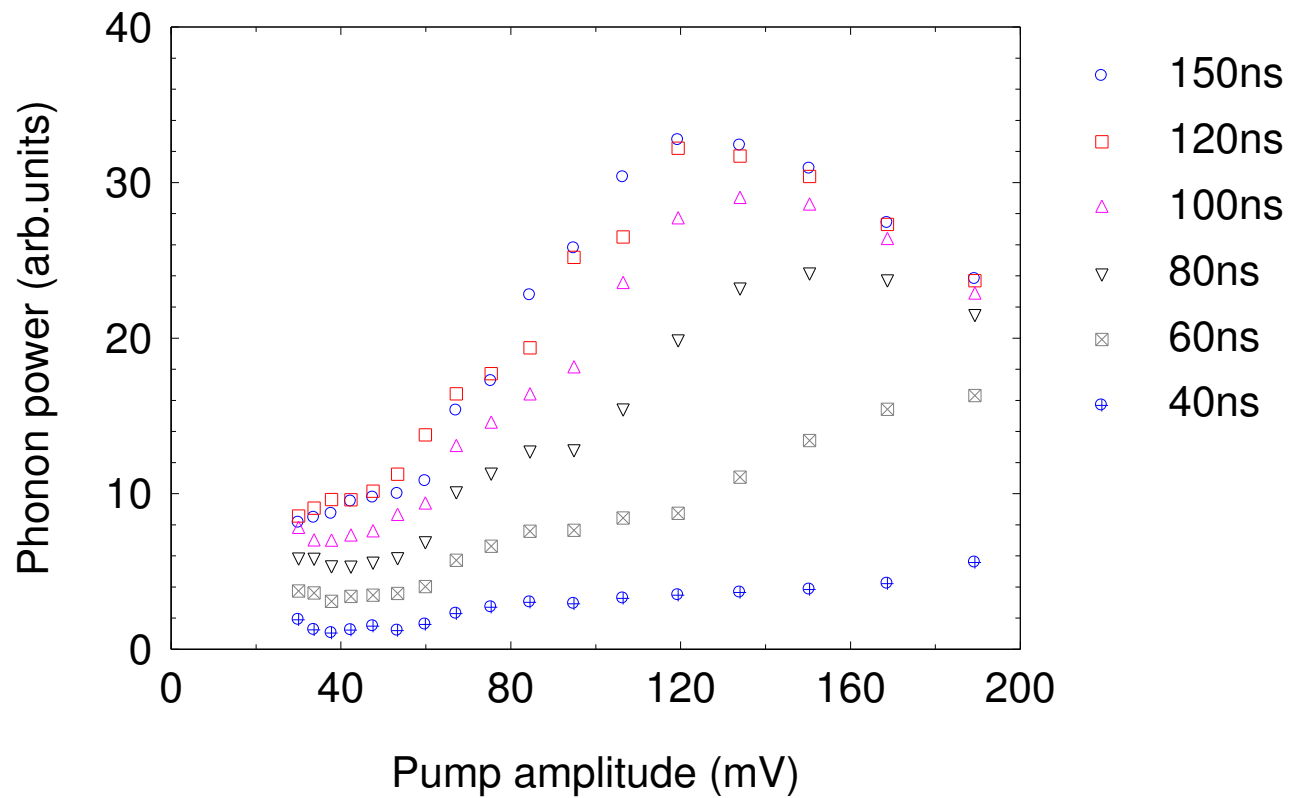


Figure 5.10: The normalised LA phonon signal plotted against pump amplitude revealed a pronounced peak centred at 125 mV at steady state intensity. The LA phonons take 120 ns to reach this steady state intensity.

## 5.5 Evidence and Analysis of the Phonon Build Up

As capacitive coupling is not an issue with this device, further evidence of LA phonon build up in the MN 685 SASER device may now be obtained. Firstly, to disassociate the increase in power from the bolometer traces due to an accumulation of signal from applying a long pulse, the bolometer signal was analysed using the convolution method as previously described by Equation 5.3. Figure 5.11 shows the temporal convolution of a 10 ns phonon signal at 53 mV pump amplitude, where amplification is not expected, with the 230 ns rectangular pump pulse and normalised to the steady state value of the actual bolometer trace at 190 mV (at 230 ns). The actual bolometric response at 53 mV was also included as a comparison.

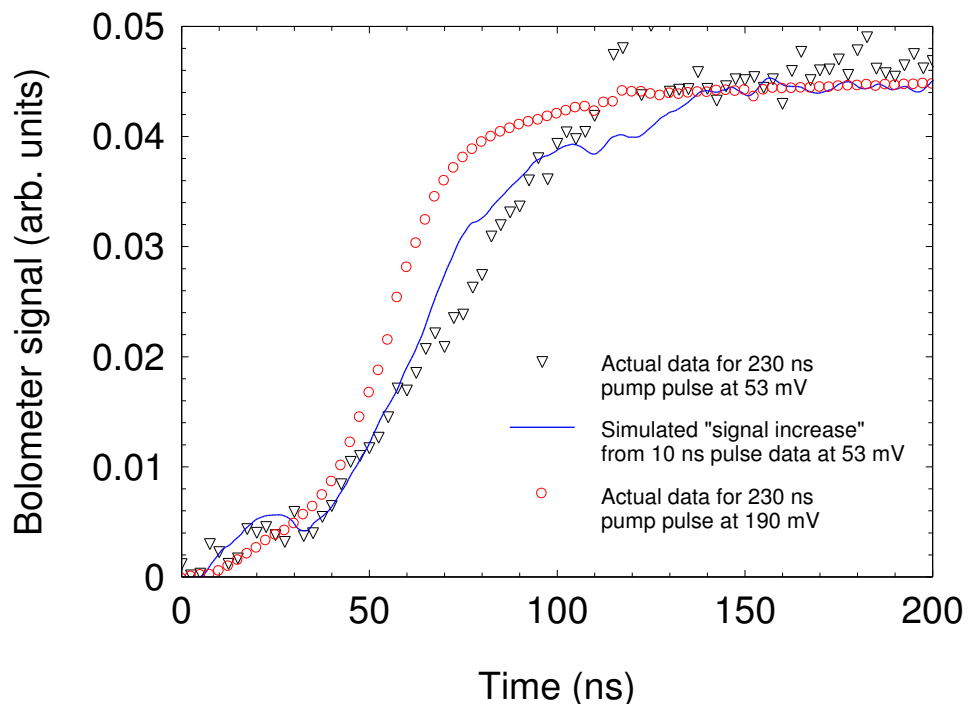


Figure 5.11: Comparison between the (simulated) accumulations of phonon signal with the actual phonon signal obtained from the bolometer for pump amplitudes of 190 mV and 53 mV respectively. The difference between the two traces, at different pump amplitudes, is attributed to the build up of LA phonons in the cavity, which is clearly observed for the data at 190 mV pump amplitude.

The estimated increase in the phonon signal matches quite well with the actual bolometer signal when SASER action is not expected to occur inside the cavity. The bolometer signal is different at 190 mV, where amplification is expected, and indicates that the faster rise rate is due to an increase in the (stimulated) LA phonon emission.

However, this rise in the phonon signal where amplification is present, as shown in Figure 5.11, also includes components of the TA phonons. The influence of the TA phonons to the overall bolometer signal may be investigated by analysing the TA phonon signal at short pulses. The temporal increase of the TA phonons may be estimated by fitting the leading edge of the TA curve for 20 ns pulse duration with an equation that describes the exponential rise and fall of the signal after time  $\tau$ , where the rate of rise and fall is related to the time constant of the system as:

$$y = \frac{a(1 - e^{-\frac{x}{b}})}{(1 + e^{\frac{x-1.25 \times \tau}{b}})}, \quad (5.5)$$

where  $\tau$  is the length of the applied pulse and  $a$  and  $b$  were coefficients determined by the fit as 0.003916 and  $28.4 \times 10^{-9}$  respectively. Figure 5.12 shows the simulated growth of the TA phonons for several pulse widths where the fit of Equation 5.5 is represented by the red line.



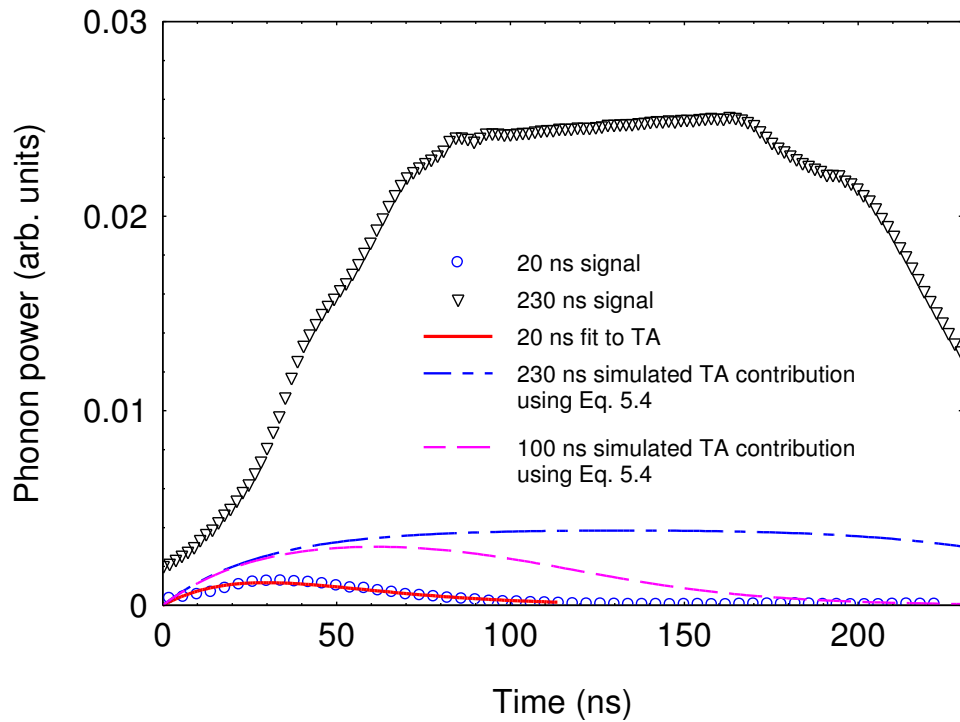


Figure 5.12: The zero time indicated the arrival of the TA phonons. The blue circles represent the 20 ns data points at pump amplitude of 106 mV whilst the red curve represents the fit. A simulation of the curve for pulse durations of 100 ns and 230 ns were obtained using Equation 5.5 and are represented by the blue and pink dotted lines respectively. The actual data for a 230 ns pulse (also at 167 mV) is shown by the black triangles for comparison.

The simulated temporal increase of the TA phonon signal, denoted by the pink and blue dotted lines for 100 ns and 230 ns pulse durations respectively in Figure 5.12, showed that the TA phonons maintained at a constant level by 35 ns and contributed no more than 15 % to the actual bolometer signal (black triangles). This is comparable to the losses due to scattering, already accounted for in the build up equation. Therefore, there is no need for a rigorous analysis to remove the TA contribution from the original trace, and the accumulated phonon signal observed in the bolometer traces may be ascribed to be dominated by the LA phonons.

Figure 5.13 shows the estimated time for the signal to reach 90 % of the steady state intensity, for a range of pump amplitudes.

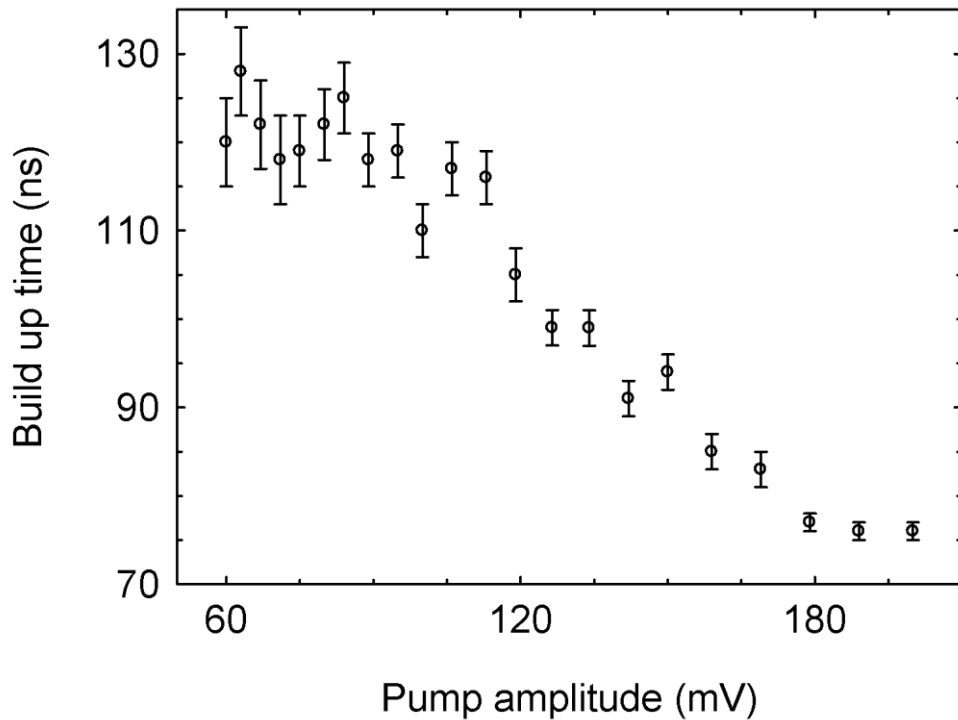


Figure 5.13: The time for the signal to reach 90 % of the steady state level across a range of pump amplitudes. The signal accumulates much faster between 90 mV and 170 mV, indicating an increase in phonon population.

A decrease in the time it takes for the signal to reach steady state level, as shown by Figure 5.13, indicates an increase in the level of phonon gain between 90 mV and 175 mV. Analysing beyond 200 mV was not possible due to bolometer saturation issues, as previously explained in Section 5.2. Nevertheless, the graph does imply that the time to reach the steady state level is no longer decreasing rapidly after 170 mV, which may indicate maximum gain is achieved by 170 mV.

To further clarify that this rise in phonon signal was due to the build-up of LA phonons via stimulated emission, the build-up equation, Equation 2.42

$$I(t) = \frac{I_{SS}I_0}{I_0 + (I_{SS} - I_0)e^{-\gamma t}}, \quad (5.6)$$

where  $\gamma$  is the net gain and  $I_0$  and  $I_{SS}$  are the initial and steady state intensities respectively was fitted to the 230 ns data set. A good fit was obtained between 3.5 dB and 9 dB, which corresponded to pump amplitudes between 106 mV and 200 mV respectively, as shown in Figure 5.14.

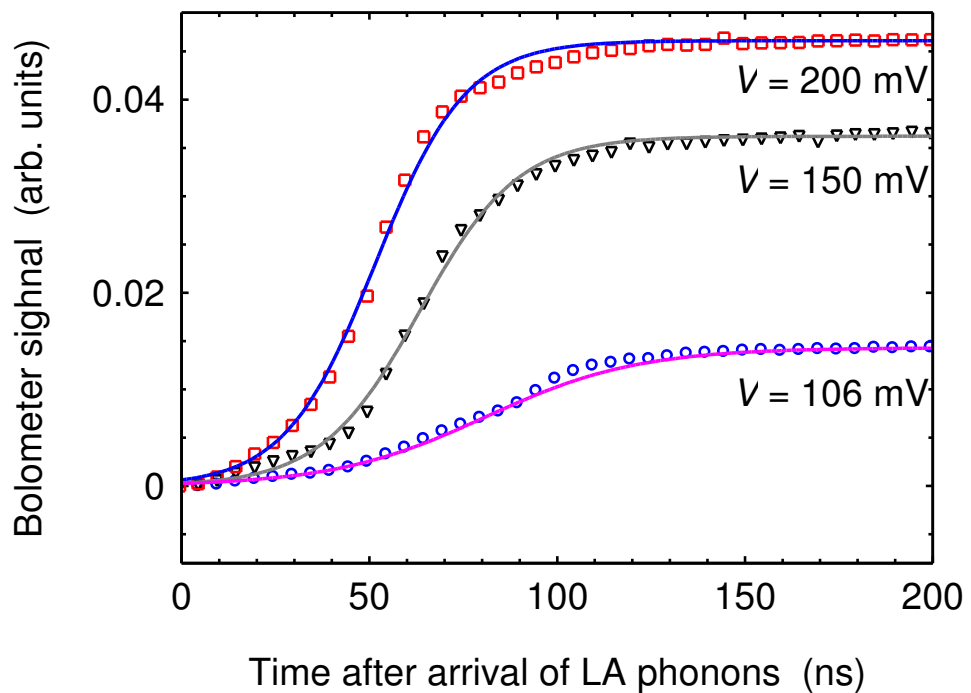


Figure 5.14: Theoretical fit to the rising edge of the bolometer trace for several different pump amplitudes with zero time indicating the arrival of the LA phonons. A good fit was obtained between 200 mV and 106 mV.

Equation 5.6 is only valid if the net gain is positive. Therefore, only at a certain range of pump amplitudes, when the gain was able to compensate the losses in the cavity, will sustained phonon oscillations occur. This is consistent with the above results where a good fit of this equation was only observed from 106 mV onwards;

indicating that a positive net gain was achieved by stimulated emission above 106 mV, as spontaneous emission dominates at lower pump amplitudes.

From the theoretical fit, it was possible to determine the ratio of the initial and steady state intensity as well as the net gain for all pump amplitudes. Table 1 below summarizes the values of the parameters in Equation 5.5, obtained between 106 and 200 mV.

Device Voltage, mV	$\frac{I_{SS}}{I_0}$ ( $\pm 0.01$ %)	Net gain, $\gamma$ ( $\text{cm}^{-1}$ ) ( $\pm 0.02$ %)
106	43	99
113	63	111
119	100	135
127	127	143
134	106	147
142	115	152
150	117	163
159	124	167
169	132	186
179	116	184
189	80	181
200	74	175

Table 5.1: Parameters obtained from a theoretical fit to the leading edge of the 230 ns bolometer traces for pump amplitudes between 106 mV and 200 mV. From these parameters, other attributes such as the gain of the gain medium, the output power and the efficiency of the SASER device may be deduced.

Other key properties of the SASER device may be deduced from these parameters such as the gain of the gain medium,  $\gamma_0$ , the output power and the efficiency of the SASER device, as explained in Section 2.4.

### 5.5.1 SASER Gain

In Chapter 2, the net gain was expressed as

$$\gamma = \gamma_0 - \gamma_{th}, \quad (5.7)$$

and the threshold gain for the MN 685 SASER device was calculated in Chapter 4 as  $233 \text{ cm}^{-1}$ . From the value of net gain extracted in Table 1, an estimate of the gain,  $\gamma_0$ , may be obtained for all pump amplitudes as shown in Figure 5.15.

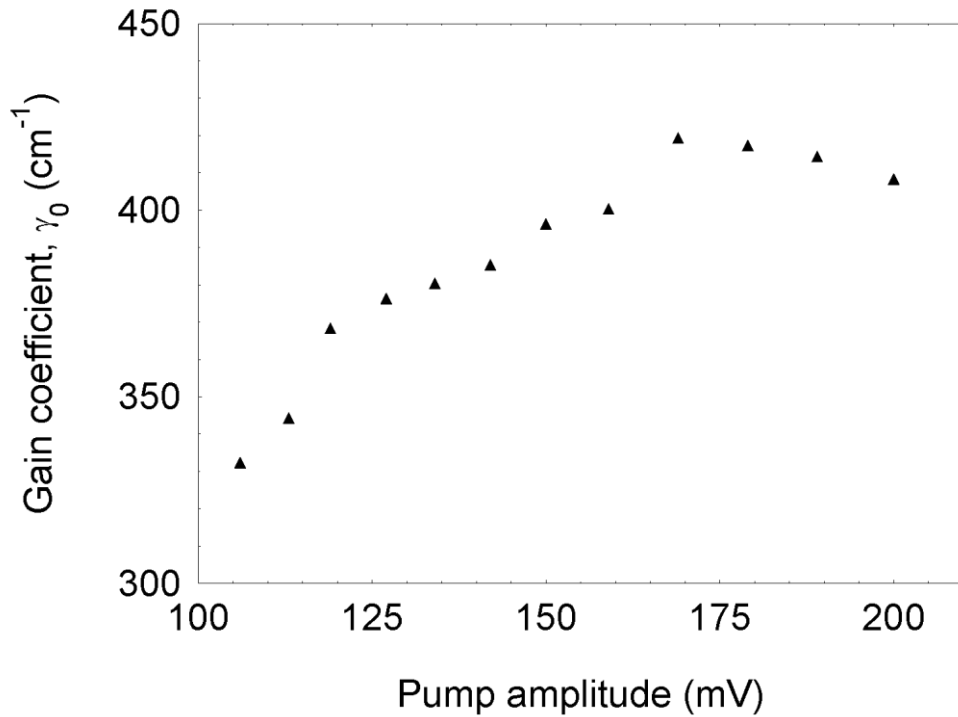


Figure 5.15: The gain profile estimated from the net gain. The gain coefficient is slightly increasing with increasing pump amplitudes and starts to decrease from 170 mV. The average gain coefficient is  $376 \pm 40 \text{ cm}^{-1}$ . Error bars are included but are typically smaller than the size of the data points.

The gain spectrum, as shown in Figure 5.15, indicated an average value of gain of  $376 \pm 40 \text{ cm}^{-1}$  over the range of pump amplitudes. A broad gain profile, such as this, may be attributed to disorder, present in the SL, as discussed in [38]. By examining the gain curve between  $300 \text{ cm}^{-1}$  and  $450 \text{ cm}^{-1}$ , the gain appears to be increasing with increasing pump amplitudes; peaking at around  $419 \text{ cm}^{-1}$  at pump amplitude of 167 mV. A maximum gain, at this pump amplitude, was also observed in Figure 5.13 where the time it takes for the phonon signal to reach steady state intensity was approaching a constant value from 170 mV.

A theoretical estimate of the gain profile was obtained by using the numerical algorithm described in [32]. The algorithm takes into account factors contributing to a decrease in the phonon increment such as the electron tunnelling rate between adjacent quantum wells, the finite electron temperature and the screening effects due to the electron-phonon interaction. By using the appropriate parameters for the gain SL used in this work, a simulation of the gain profile at a fixed phonon energy corresponding to 325 GHz phonons was obtained and is shown in Figure 5.16. The software coding used in obtaining this graph was created by Dr R Beardsley [83].

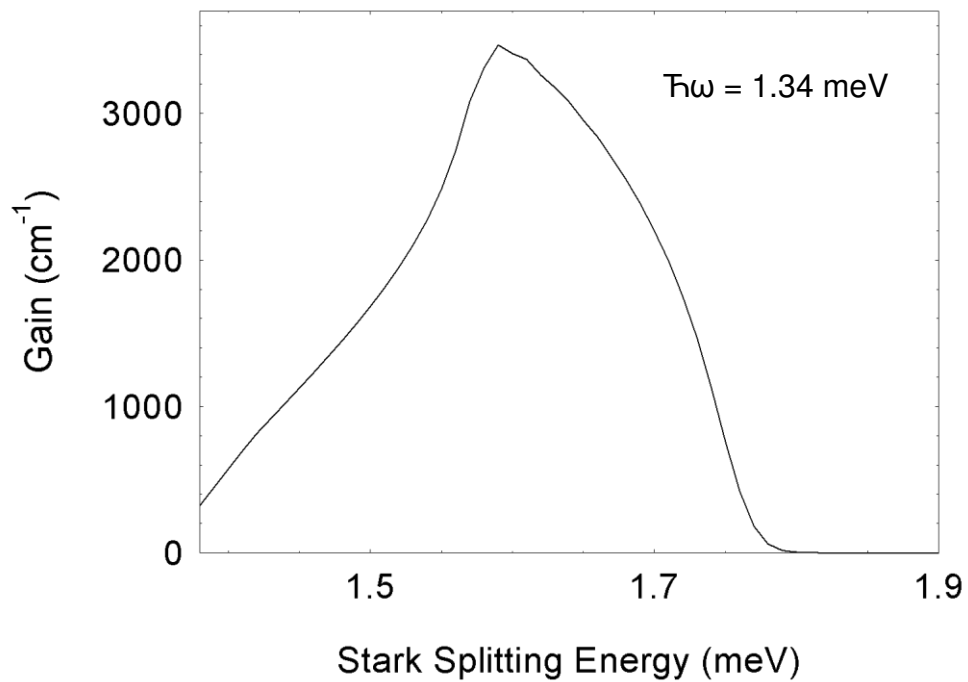


Figure 5.16: A simulation of the gain profile for the gain medium of the MN 685 SASER device. The gain is plotted against Stark splitting energy,  $\Delta$ , for a fixed phonon energy of,  $\hbar\omega = 1.34$  meV (at frequency of 325 GHz).

The prediction of the phonon increment (or gain) yield a peak gain coefficient of  $3000 \text{ cm}^{-1}$  at 1.6 meV, of which is at a much higher energy than the 325 GHz phonon energy (1.34 meV) and the estimated gain coefficient is an order of magnitude higher than observed experimentally. The discrepancy may be accounted for by some inaccuracies in the theoretical analysis. For example in determining the value of the 'true' electron temperature during the experiment, or the uncertainty in the value of the deformation potential constant, which can vary from 7-13.5 eV in the literature [56, 85].

The experimental value of gain obtained from Figure 5.15 differs from that obtained in [38] possibly due to the difference in the frequency of the amplified phonon modes as the ratio between spontaneous and stimulated emission rates, often referred to as

Einstein's A and B coefficients, has a dependence on the cube of the frequency, as described as

$$\frac{A_{21}}{B_{21}} = \frac{\hbar\omega_{21}^3}{\pi^2c^3}. \quad (5.8)$$

$A_{21}$  and  $B_{21}$  represents the spontaneous and stimulated emission rates respectively.

### 5.5.2 Estimates of the Output Power

The acoustic output power may be obtained by taking 3 % of the steady state intensity in the cavity, which is the amount of power being transmitted through the output coupler. The ratio of the steady state and initial intensities of the LA phonons is obtained from the fit of Equation 5.6 to the data; parameters listed in Table 1. In section 2.8, the initial intensity,  $I_0$  was taken as the value when stimulated emission was equal to spontaneous emission, and corresponds to one phonon per mode expressed as

$$I_0 = \frac{2\nu^2}{3\pi c_s^2} h\nu\rho\Delta\nu, \quad (5.9)$$

which includes the phonon density of states, the number of longitudinal modes in the cavity and the frequency spacing of these modes. The frequency spacing of the LA modes in this cavity was  $\approx 1.1$  GHz and the almost 100 % reflectance was across a bandwidth of 30 GHz. Therefore, 27 longitudinal cavity modes fall inside the reflectance band and the initial intensity would be 198.6



$\text{Wm}^{-1}$  for 325 GHz phonons. The estimated output power from the MN 685 SASER device (at steady state) would then be

$$P_0 = \frac{I_{SS}}{I_0} \times 198.6 \times 0.03. \quad (5.10)$$

Figure 5.17 shows the values of  $P_0$  obtained for a range of pump amplitudes. A maximum peak at  $785 \pm 40 \text{ Wm}^{-2}$  ascribed to an increase in acoustic emission was observed between 119 mV and 186 mV as indicated by Figure 5.17. The broadband nature of the peak was anticipated as the gain profile shown in Figure 5.15 also revealed a broad peak. In these regions of pump amplitudes, there was a positive net gain, hence, amplification and an increase in phonon power was expected.

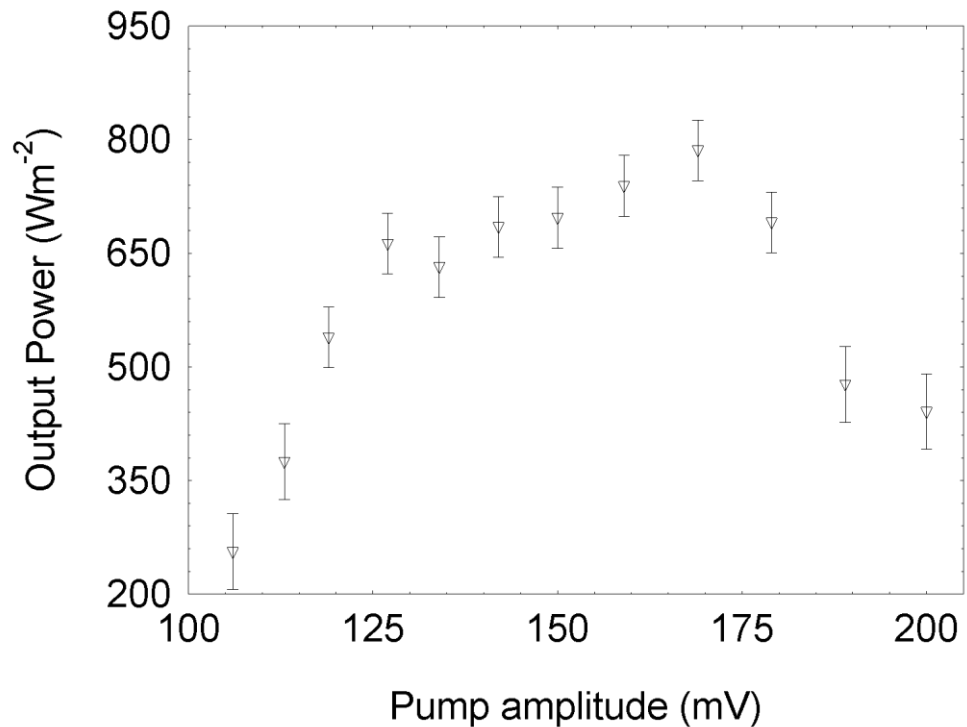


Figure 5.17: Output power of the MN 685 SASER device for a range of pump amplitudes. A broad peak was observed between 119 mV and 186 mV indicating an increase in phonon power.

However, in Chapter 4, the calculated reflectance graph of the high reflector revealed that only LA phonons with frequencies between 310 GHz and 340 GHz would be highly reflected and hence build-up in intensity. This would correspond to pump amplitudes in the range of 128 mV and 141 mV whereas the increase in the output power, shown in Figure 5.17, is across a much wider range of pump amplitudes. It is possible that the thickness of the GaAs/AlAs layers making up the cavity mirrors vary slightly, providing a much broader frequency range for the reflection of the LA phonons. Nevertheless, even if the reflectance decreases, above 340 GHz, the gain profile is broad and subject to a positive net gain, phonon oscillation inside the cavity may still be possible. The only difference may just be in terms of the build-up time towards the steady state intensity.

### 5.5.3 SASER Device Efficiency

Another characteristic of the MN 685 SASER device that could be obtained from the fit was the efficiency. The efficiency of the device was attained by taking the ratio of the output power with the power consumed by the device at different pump amplitudes and is shown in Figure 5.18.

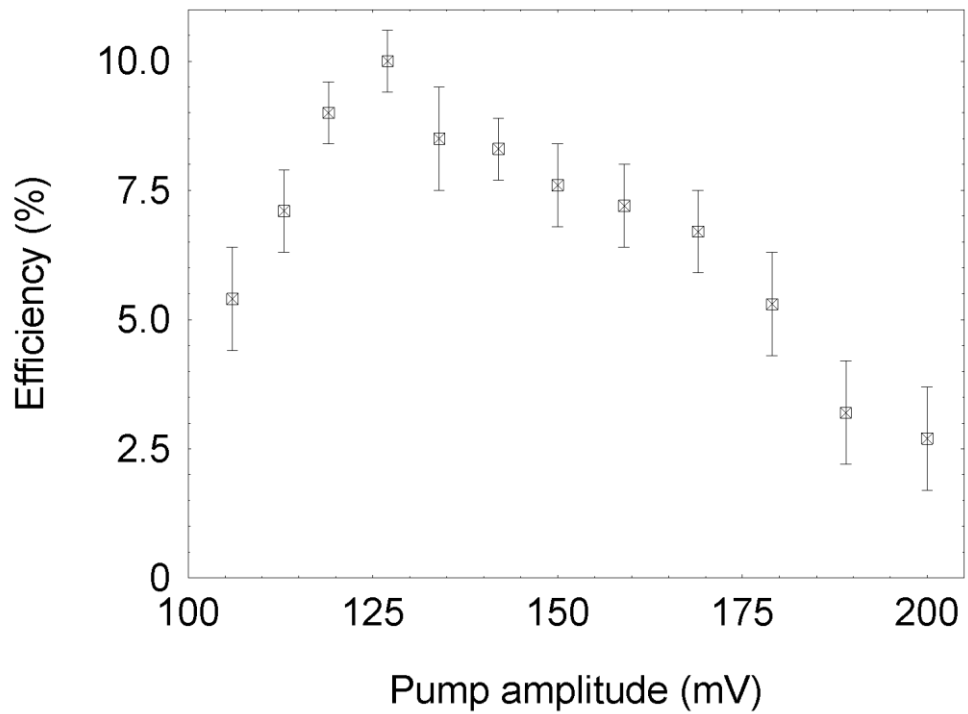


Figure 5.18: The efficiency of the MN 685 SASER device as a function of pump amplitude. The maximum efficiency is between 120 mV and 145 mV, as shown by the distinct peak in the graph.

The efficiency of the MN 685 SASER device shows a peak between 120 mV and 145 mV; providing a maximum value of  $10 \pm 0.6$  %. As previously mentioned in section 5.5.2, the range of pump amplitudes where the device is predicted to work best is between 128 mV and 141 mV. Therefore, the increase in power observed in Figure 5.17 that is beyond 145 mV was not entirely due to phonon amplification but also due to unwanted heat that was dissipated in the device, as the efficiency was decreasing beyond this value.

## 5.6 'Sidelight fluorescence'

In studying the MN 685 SASER device, a second bolometer (bolometer 2) was placed at a  $57^\circ$  angle from the device centre, as illustrated earlier in Figure 5.3. The purpose of this experiment was to observe the equivalence of an effect termed as 'sidelight fluorescence' that is commonly observed in lasers [86]. It was shown [42] that, as soon as the threshold condition is reached, a sharp clamping of the sidelight fluorescence from non-oscillating modes was observed. The same scheme of operation was employed and phonons detected by the bolometer was analysed the same way.

Figure 5.19 shows the phonon flux detected by bolometer 2 normalised to the power and compared with the increase of phonon flux detected by bolometer 1, also normalised by the power. A 'quenching' phenomenon at SASER threshold was observed from bolometer 2. The decrease in phonon power was observed as the phonon power detected in bolometer 1 started to increase from  $120 \pm 5$  mV. This decrease in phonon power may be due to the increase of phonon intensity emitted towards bolometer 1.

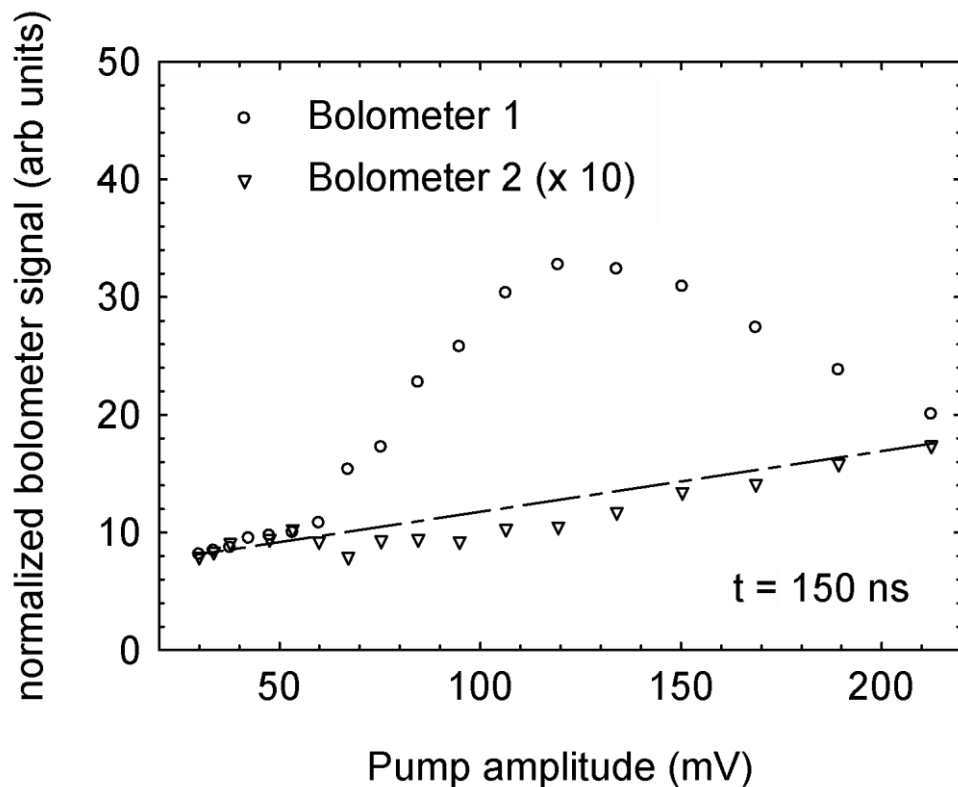


Figure 5.19: The circles represent the normalised phonon power from bolometer 1 when steady state was established whereas the triangles on the other hand represent the normalised phonon power detected by bolometer 2. The dashed line is provided as a guide to the eye.

Not only does this result resemble the clamping of the sidelight fluorescence, hence clarifying the threshold condition for sasing, as observed in lasers but also it is suggesting that the acoustic beam is highly directional towards the bolometer situated directly opposite the SASER device itself.

## 5.7 Conclusion

From the bolometric experiments performed on the NU 2694 SASER device, it may be concluded that there was an increase in phonon

intensity when the Stark splitting energy was slightly higher than the energy of the cavity-confined phonon modes. However, further analysis on the build of LA phonon oscillation inside this cavity proved difficult due to the capacitive behaviour of the undoped GaAs spacers situated at each end of the gain SL.

A redesign resulted in the creation of the MN 685 SASER device, with additional carrier concentration inside the gain SL as well as gradiently doping across the GaAs buffer layers to provide a SASER device with lower resistance and to avoid issues with regards to the capacitive coupling effect. The study of the LA phonons building up inside this acoustic cavity was then possible. Once threshold gain was achieved, a non-linear increase in phonon power was observed in the initial rising edge of the bolometer traces and after a finite number of round trips, the LA phonons reach steady state oscillation. The normalised phonon power revealed a peak where amplification was expected and by fitting a theoretical expression for the phonon build up to the bolometric data, other attributes of the SASER device were attained. The average gain coefficient was determined as  $376 \pm 43 \text{ cm}^{-1}$  with maximum acoustic power of  $785 \pm 40 \text{ Wm}^{-2}$  and device efficiency as high as 10 %. Furthermore, a reduction in the phonon power was observed at a 'side-window'; indicating that the increase in acoustic emission was highly directional.

# **CHAPTER 6**

## **SELF INJECTION SEEDING OF THE SASER DEVICE**

The purpose of this chapter is to investigate the behaviour of the SASER devices when a beam of coherent phonons, at a fixed frequency, were introduced into the cavity; a similar approach to injection seeding applied to lasers. The increase in acoustic emission detected by the bolometer relating to the frequency of the injected phonon modes is discussed in detail for each SASER device.

In the recent decade, much research was focused into making a high spectral purity, frequency stable, and precise tuneable pulsed lasers with a relatively high power. The technique of injection seeding, that is both simple and reliable, has led to the possibility of achieving these and in some cases also improving the efficiency of the lasers and providing an effective way of producing single longitudinal mode operation [87-90] . A narrow linewidth SASER in the technologically important THz frequency range with added feasibility of frequency selectivity would benefit a wide range of applications in a similar way to the lasers. For example, in high resolution spectroscopy, cross-disciplinary diagnostics and imaging.

In lasers, the output power from the seed laser is injected into the high power oscillator cavity and the seed input would then grow inside the cavity. If the injected seed is stronger than the spontaneous emission, the pulse would build up at a much faster rate than the naturally occurring pulses inside the cavity, which builds up from the zero point energy of the laser cavity or from spontaneous emission. The injected seed would deplete the gain of

the laser material before the natural pulse has had time to build up, and so, the laser output will acquire properties of the seed laser rather than the free running laser [91, 92].

Injection seeding is commonly applied to a Q-switched or a gain switched laser medium either by self or external seeding from a low power output laser into the cavity of the high power laser. In a Q-switched laser, the cavity is maintained at a low Q (i.e. the losses in the cavity is high) during operation. As the seeded pulse is injected, the gain would build up to a high value and eventually release a high energy pulse. On the other hand, for a gain-switched laser, the laser is initially set to below lasing threshold. Then the injected seed pushes the gain to above threshold level until it depletes the population inversion within the gain medium and releases the laser pulse. If the pumping rate is sufficiently high, then the gain can be forced high enough above threshold in a shorter time compared to the natural build-up of the cavity modes [93]. In both cases (gain-switched and Q-switched), lasing will occur at the wavelength (or frequency) of the intended seeded longitudinal mode as its build up time is much faster than any other unseeded mode in the cavity that must build up from random noise photon.

In Chapter 4, the phonon modes generated in pump-probe measurements from the high reflector SL of the MN 685 SASER device, reflecting at 36 % for zone centre phonon modes, revealed that the system would decay to its original state on a timescale of one round trip. Therefore, if gain is present in the system then the MN 685 SASER device will either act as a phonon amplifier or as an oscillator for these injected modes to build up with a few round trips, provided the gain was able to compensate the cavity losses. In the work presented in this chapter, a similar method to injection seeding in a Q-switched cavity was studied using the MN 685 SASER device, where phonons were injected at frequencies where the cavity had a



low Q. On the other hand, the NU 2694 SASER device was seeded with phonons at the frequency of the oscillating cavity modes.

A schematic diagram of the experimental operation is shown in Figure 6.1, where the Tsunami laser was used to excite the high reflector SL structure. A bolometer, fabricated on the reverse side of the grown layers, was centred with the SASER device axis. A range of negative DC biases were sent to the device and the bolometric response for each bias was analysed individually.

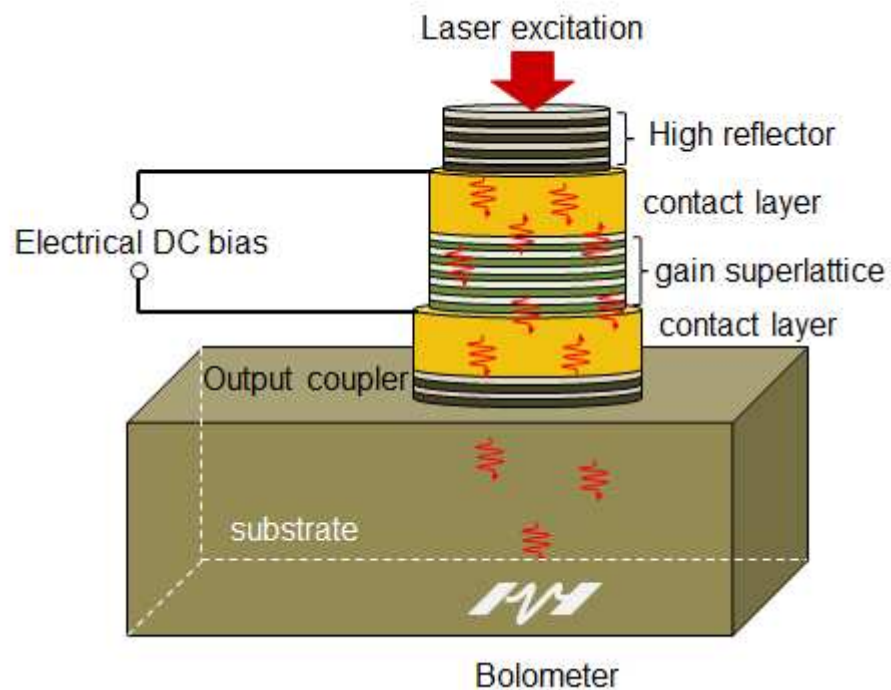


Figure 6.1: Schematic diagram of the mode of operation where the laser is used to excite the phonon modes from the high reflector SL. A bolometer was used to detect the LA phonons escaping the cavity as a function of time for all DC biases applied to the device.

The laser light passed through a pulse selector (APE Pulse Select as described in Chapter 3) to provide means of slowing the laser's repetition rate by a set numerical ratio and a range of DC biases were supplied to the gain medium SL via the contacts. The

bolometer was used as the phonon detector (bolometer operation is discussed in chapter 3) whereas the 0.5 GHz bandwidth DPO 7054 oscilloscope was used for data acquisition and was triggered from the pulse selector. The IV characteristics of the SASER devices were presented in Chapter 5; however, it is also important that the IV characteristics of the device remain unaffected under light illumination, as explained in the following.

### 6.1 Current-Voltage characteristics under light illumination

IV measurements of the MN 685 SASER device was conducted under two conditions; namely, under light illumination and in the dark, as shown in Figure 6.2, where the laser was set to 750 nm. The illuminated device, as shown in the figure, is not critically affected by the laser light. This is not surprising as only a small portion of the light is absorbed by the gain medium SL at this wavelength. Slight fluctuations observed at higher voltages in the illuminated IV are likely due to photo-excited non-equilibrium carriers and the heating of the sample. For laser beams incident onto the device at wavelengths below 750 nm, the IV curve remains unchanged. This may be due to the fact that these wavelengths are tuned close to the optical resonance of the high reflector SL where absorption would be high and there would be very little optical breakthrough.

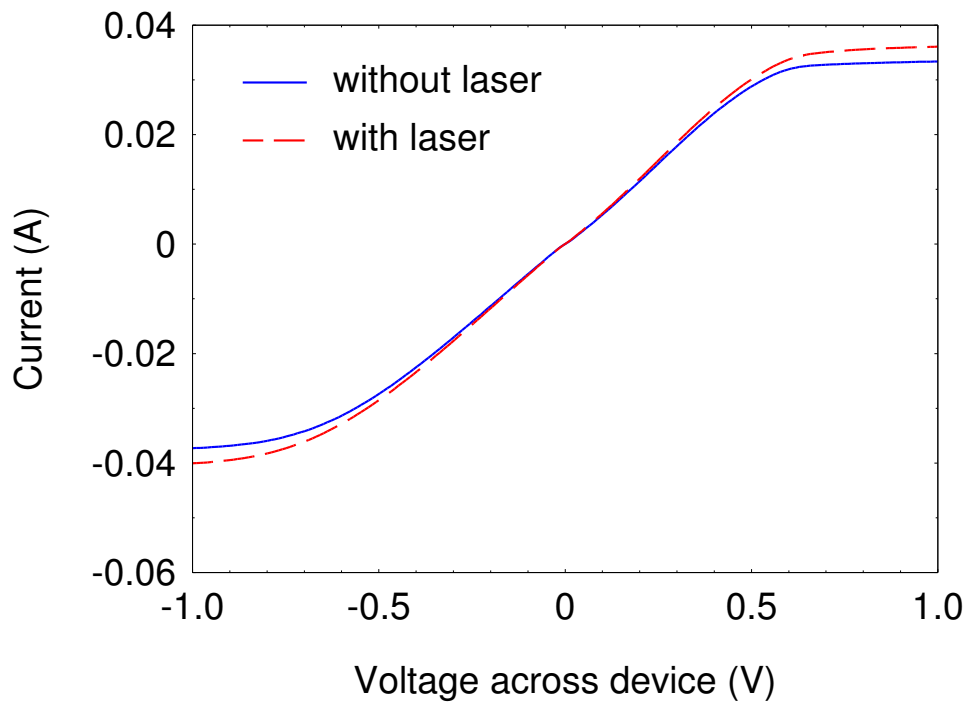


Figure 6.2: The current-voltage (IV) characteristics of the MN 685 SASER device under investigation. There is no critical change to the IV characteristics of the device under illumination by the laser, at wavelength of 750 nm, compared to when in the dark.

The essential point here is that the electronic behaviour of the gain medium SL remains unchanged with illumination, especially in the region where SASER gain is expected; even when the illumination wavelength is at 750 nm the effect is only slight. Sample NU2694 reveals a similar situation where the wavelength of excited light was at around 750 nm. The issue of capacitive coupling for this device, as discussed in Chapter 5, is no longer an issue here as the device is now biased with DC.

## 6.2 Injection Seeding with Modes of the Cavity – Case Study for the NU 2694 SASER device

For the first case, the cavity of the NU 2694 SASER device was seeded with phonons at the frequency of the oscillating cavity modes. The high reflector SL structure was excited at wavelengths of 720 nm and 750 nm and the bolometric response at each applied bias, between 0 mV and 500 mV, was recorded and analysed for both wavelengths respectively. The pulse selector was set with a division ratio of 600, hence providing a delay of 7.5  $\mu$ s between the laser pulses. The effective ‘gate’ of the pulse selector was set to 12 ns, to make sure that only one laser pulse was coming through the pulse selector between each delay. All measurements were conducted at the bolometer transition temperature where  $T \approx 2$  K. In Section 4.1, this particular structure was not used for pump–probe measurements due to the limitation of the wavelength range of the current laser, especially in detecting the zone centre phonon modes. Therefore, before going into the details of the results, it is necessary to consider carefully the phonon generation mechanism.

### 6.2.1 Phonon Generation mechanism

The generation of the oscillating cavity modes in the NU 2694 SASER device was investigated in collaboration with Dr Jeorg Debus from Dortmund University, Germany, using Resonant Raman spectroscopy (RRS). By using RRS, it was possible to tune the energy of the incoming laser with an electronic transition in the structure. The difference in energy between the laser light and the scattered light are recorded as the difference in wavenumber. This change in wavenumber or Raman shift may be positive or negative

depending on whether the emitted photon from the transition gains or loses energy.

The laser light used in the experiment was tuned at 671 nm, close to the optical resonance of the mirror SL as determined by the PL measurements in Section 4.1. Phonons at a range of frequencies were created as it is inelastically scattered in the SL. The dispersion curve for the 40 period (mirror) SL of sample NU 2694 is shown in Figure 6.3. The black dotted line represents the  $2k_{\text{laser}}$  line and the red crosses represent the phonons at  $2k_{\text{laser}}$ .

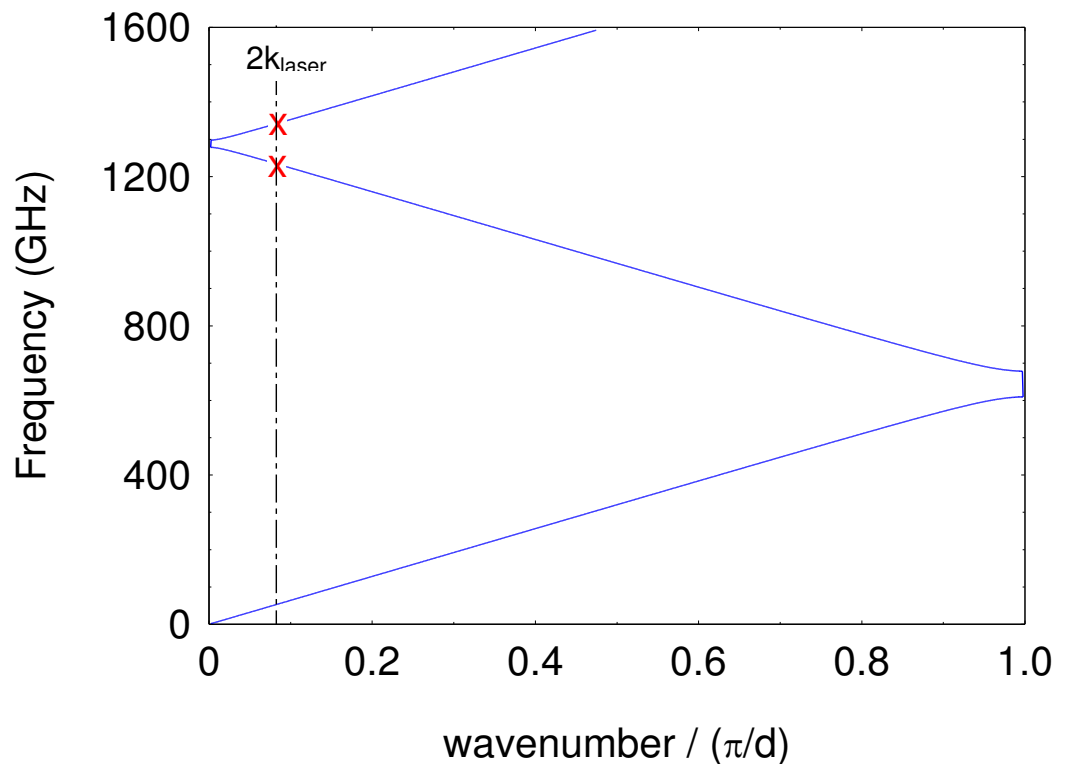


Figure 6.3: Dispersion curve of the 40 period (mirror) SL structure of sample NU 2694. The zone edge gap is between 616 GHz and 686 GHz. The  $2k_{\text{laser}}$  intercepts at 1.23 THz and 1.34 THz as indicated by the red crosses.

The  $2k_{\text{laser}}$  line, as indicated by the black dashed line in Figure 6.3, intercepts at frequencies of 1.23 THz and 1.34 THz, indicating the frequencies of the backscattering modes; as indicated by the red

crosses. These modes were clearly observed in the Raman spectrum obtained at room temperature, as shown in Figure 6.4, with the laser power at 37 mW. The Stokes line of the Raman signal was obtained under cross and parallel polarisation of the pump and probe beams.

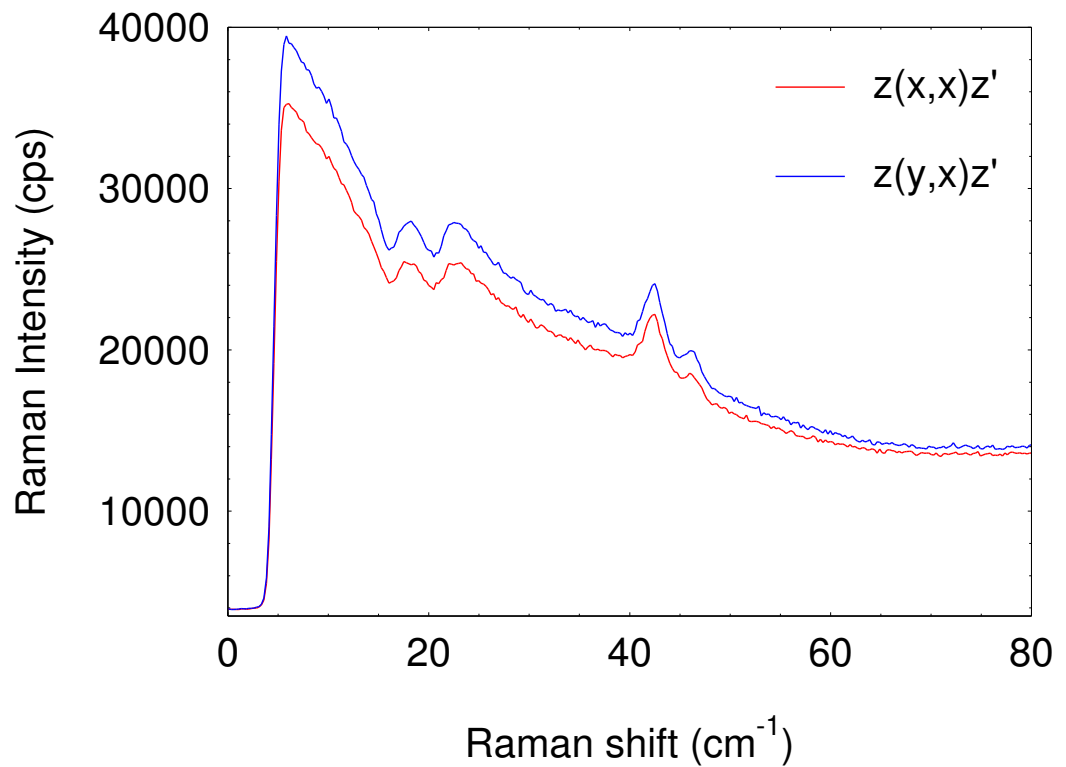


Figure 6.4: Raman spectrum of NU 2694 at room temperature obtained for two different polarisations of the pump and probe beams where  $z(x,x)z'$  means that the pump and probe beams are parallel to each other and  $z(y,x)z'$  is when the pump and probe beams are perpendicular to each other. Peaks associated to Raman shifts of  $42.73 \text{ cm}^{-1}$  and  $46.19 \text{ cm}^{-1}$  correspond to the backscattering modes, whereas peaks at  $16.07 \text{ cm}^{-1}$  and  $20.51 \text{ cm}^{-1}$  correspond to 486 GHz and 620 GHz respectively.

The strong peaks observed at  $42.37 \text{ cm}^{-1}$  and  $46.19 \text{ cm}^{-1}$  corresponded to the possible backscattering modes at 1.28 THz and 1.40 THz. Interestingly, two additional peaks, indicating Fano resonance, at  $16.07 \text{ cm}^{-1}$  and  $20.51 \text{ cm}^{-1}$ , corresponding to

frequencies of 486 GHz and 620 GHz, were also detected. The 620 GHz probably corresponds to the frequency at the zone edge gap for the high reflector SL, which was predicted to be between 609 GHz and 680 GHz as shown in the dispersion curve of Figure 6.3. It was also apparent that polarisation had no effect on the Raman signal as all peaks were clearly observed in both cases.

The above result indicates that the generation of the oscillating cavity modes at 620 GHz, by laser excitation, in this sample was possible even though the mirror SLs were a type II SL. This may be due to the SL structure being near the type I to type II crossover where the interface fluctuations are able to swap the energy of excitons between the  $\chi$  valley and the  $\Gamma$  valley locally [94]. Both localised states of excitons are within the same energy range, therefore, the electron's wave function in the conduction band is a combination from the  $\chi$  and  $\Gamma$  valley. By tuning close to the optical resonance of this energy, as described earlier, it was possible to observe the 620 GHz phonon modes.

These Raman active modes may also be generated, with the current limitation of the laser, below the absorption energy as described in [95]. The laser light used in the literature was 0.5 eV below the band gap of the material whereas in this work, the laser was tuned to 0.25 eV and 0.31 eV below the absorption energy of the mirror SL for the 720 nm and 750 nm excitation wavelengths respectively. Although the phonons generated will not have a high intensity, it may be sufficient to gently 'perturb' the system at the frequency of the cavity modes.

## 6.2.2 Results from the NU 2694 device

The arrival of each components of the phonon pulse were recorded by the bolometer as shown in Figure 6.5 where the laser was tuned to 720 nm and the applied bias was at 400 mV. The zero time indicated the arrival of the optical pulse (from luminescence) followed by the LA and TA phonons at 46 ns and 64 ns respectively. This is indicated by the respective arrows in the figure.

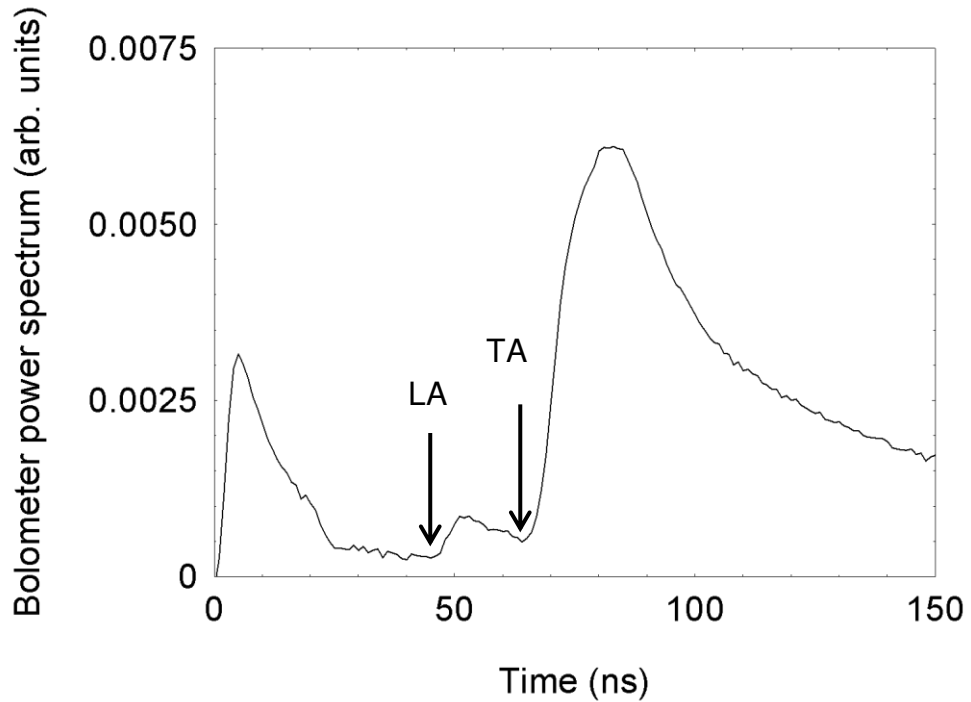


Figure 6.5: The bolometer signal for excitation wavelength of 720 nm and a dc bias of 400 mV. The zero time indicates the arrival of the direct optical pulse (luminescence) followed by the arrival of the LA and TA phonons as indicated.

The detected TA phonon peak, in Figure 6.5, is much larger than the LA phonon peak due to the normally observed phonon focusing effects in the [100] growth direction [49]. If the LA and TA were generated in equal amounts then the TA signal would be 20 times larger [96]. However, the fact that the ratio of the TA phonon signal in this case is only 8 times larger indicates that generation is weighted



in favour of the LA phonon modes, possibly due to stimulated emission.

Using a similar method to that explained in Chapter 5, by integrating over the rising edge of the LA phonon signal, the LA phonon power dependence of the bias is obtained. Figure 6.6 illustrates the detected LA phonon power as a function of the voltage dropped across the gain SL for two excitation wavelengths. Signals obtained before the device threshold, below  $\sim 200$  mV, has been removed for clarity. In both cases, the increase in the LA phonon power was observed from 165 mV corresponding to a Stark splitting energy of 3.3 meV and peaked at around 219 mV (4.4 meV).

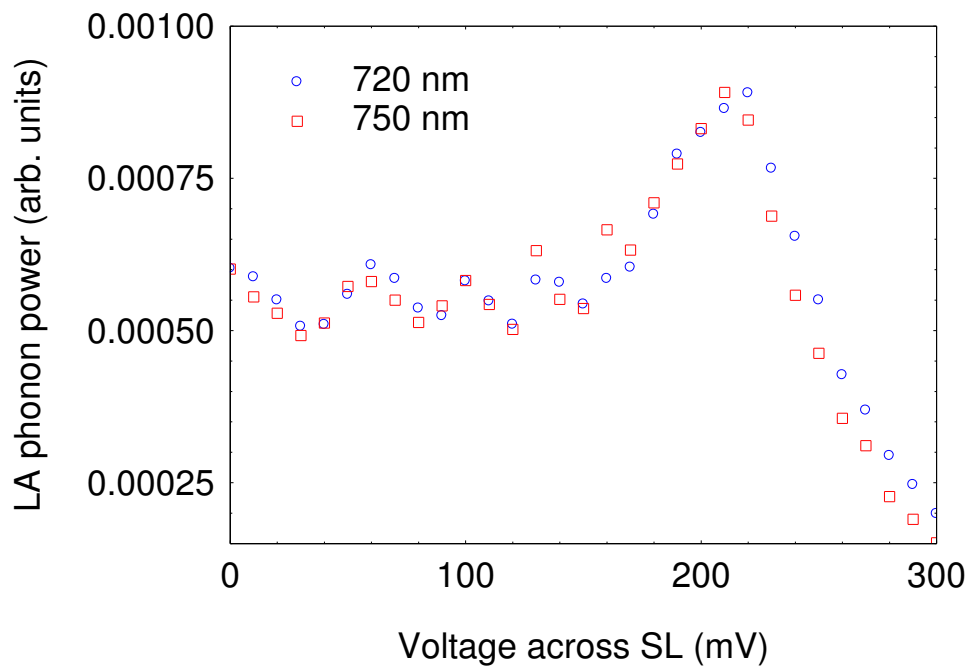


Figure 6.6: The LA phonon power against the voltage across the device for excitation wavelengths of 720 nm and 750 nm. The device threshold of 200 mV has been removed for clarity.

The increase in the LA phonon power, as shown in Figure 6.6, is occurring at considerably higher energy than the rise in the LA phonon power observed by purely electrical measurements, as

discussed in Section 5.2.1. Figure 6.7 shows a comparison of the normalised LA phonon power obtained by the electrical pumping method and the rise in LA phonon power attained by seeding additional oscillating cavity modes at frequency of 646 GHz into the electrically pumped SASER device (magnified for clarity).

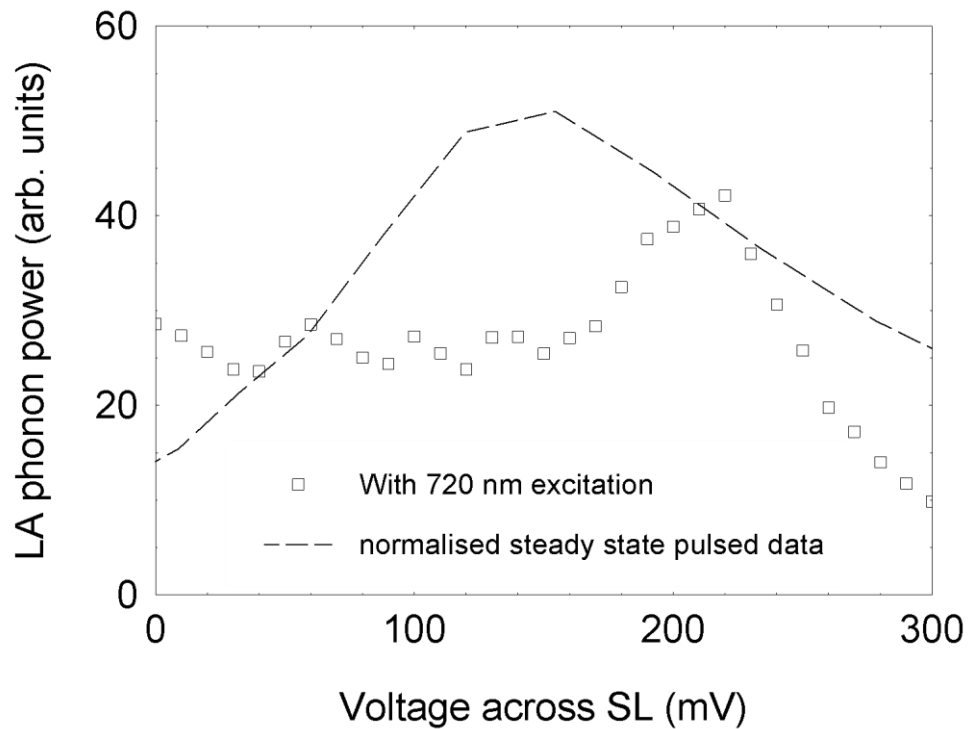


Figure 6.7: A comparison of the normalised phonon power at steady state (200 ns data) obtained by purely electrically pumping the gain SL, with the LA phonon power obtained when additional cavity modes were seeded into the electrically pumped SASER device (at 720 nm).

Without phonon injection, the phonon power starts to decrease from 160 mV, as shown in Figure 6.5, indicating a reduction in the net gain. By effectively seeding the cavity with additional phonons at the frequency of the oscillating cavity modes, an increase in phonon power was observed from 165 mV as the net gain starts to decrease whilst the gain of the gain medium was still above threshold. A smaller net gain also occurs below 100 mV, but no increase in the

LA phonon power was observed at lower biases possibly because the amount of current available is small. Furthermore, the amount of additional phonons injected into the gain medium may not be large and hence the possibility of observing any increase in acoustic emission at lower biases is small.

The effect due to the seeded mode when the system is in steady state may be deduced by recalling Equation 2.42 describing the LA phonon build up, as follows

$$I(t) = \frac{I_{SS}I_0}{I_0 + (I_{SS} - I_0)e^{-\gamma ct}} , \quad (6.1)$$

where  $\gamma$  is the net gain and  $I_{SS}$  and  $I_0$  represents the steady state and initial intensities respectively. If additional phonons were introduced inside the cavity before steady state is achieved, then the LA phonon build up would occur at a much faster rate as the initial population or phonon intensity would be at a much higher value. The rate of change of the intensity with respect to  $I_0$  is

$$\frac{dI(t)}{dI_0} = \frac{[I_0 + (I_{SS} - I_0)e^{-\gamma ct}]I_{SS} - I_{SS}I_0[1 - e^{-\gamma ct}]}{[I_0 + (I_{SS} - I_0)e^{-\gamma ct}]^2} . \quad (6.2)$$

Under steady state conditions (as  $t$  approaches infinity), Equation 6.2 would be

$$\frac{dI(t)}{dI_0} = I_{SS}I_0 - I_{SS}I_0 = 0 , \quad (6.3)$$

implying that any additional phonons, at the frequency of the oscillating cavity modes, introduced into the cavity would not contribute to any increase in the overall phonon power when steady

state is reached. Changes in intensity, with respect to  $I_0$ , would occur when the additional, injected, phonons contribute to the build-up of phonon oscillations in the system.

The build-up of phonon oscillations would depend on the threshold gain as phonon oscillations would only occur in the cavity when the gain is above threshold value. Figure 6.8 shows the threshold gain of the NU 2694 cavity across a range of frequencies, calculated from Equation 2.43, described as

$$\gamma = \gamma_0 - \gamma_{th} = \gamma_0 - \frac{\ln(R_1 R_2 e^{-2kL_s})}{2L}, \quad (6.4)$$

where  $\gamma$  is the net gain,  $\gamma_0$  and  $\gamma_{th}$  are the gain and threshold gain respectively,  $R_1 R_2$  is the product of the reflectance of the cavity mirrors,  $e^{-2kL_s}$  represents the scattering losses and  $L$  is the cavity length.

An estimate of the gain for 620 GHz phonons, obtained from [38], is  $3600 \text{ cm}^{-1}$ , as shown by the horizontal black dotted line in the above figure, which is indicating that build up to steady state intensity would no longer occur by 2.84 meV. Hence, the LA phonons would not build up to steady state intensity when the bias was tuned to Stark splitting energies  $\geq 2.84$  meV. The normalised LA phonon power, without the seeded modes, peaked at 140 mV corresponded to a Stark splitting energy of 2.8 meV, as labelled by the vertical red dashed line in Figure 6.8.

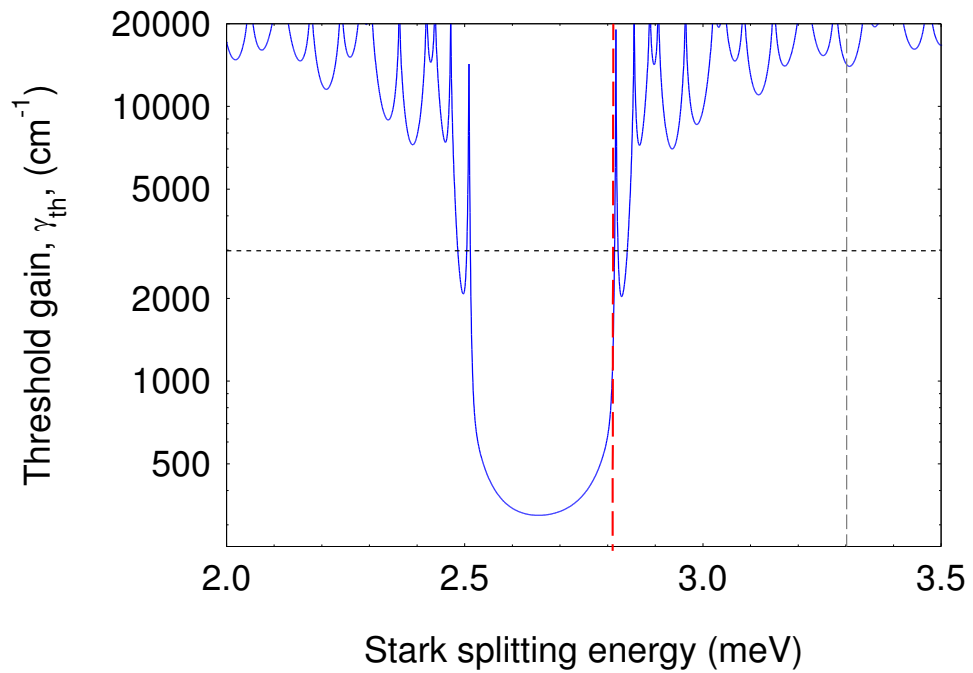


Figure 6.8: The threshold gain for the NU 2694 device, on a logarithmic scale, across a range of Stark splitting energies. The red and grey vertical dashed lines represent the Stark splitting energies corresponding to voltages of 140 mV and 165 mV dropped across the gain SL respectively. Based on an estimated value of gain for 620 GHz phonons obtained from [38], represented by the horizontal black dotted line, phonon build up is theoretically possible between 2.49 meV and 2.84 meV.

The decrease in the LA phonon power above 2.8 meV indicates that the net gain is no longer able to compensate the losses in the cavity beyond 2.8 meV. However, the injected phonons showed an effect when the Stark splitting energy was at around 3.3 meV (165 mV), as indicated by the vertical grey dashed line in Figure 6.8, where the gain was below the threshold value. Here, the gain medium will act as an amplifier as the gain would not be able to compensate with the cavity mirror losses. However, since the injected modes are preferred by the cavity, they may complete multiple round trips and hence, show an increase in phonon power.

### 6.2.3 Signals Associated with Bolometer Sensitivity

As discussed in Section 3.6, bolometric detection depends on the change of resistivity across the superconducting transition curve of the bolometer. At the start of the experiment, the bolometer was held at the bottom end of the transition and changes in the resistance caused by the incoming signal pushes the transition further up the curve. The increase in the background, caused by the application of bias, may move the transition point up to the linear region of the transition curve where the bolometer is less sensitive, and towards bolometer saturation. However, the TA signal and optical signal should not depend on bias as they are not amplified by the gain SL. For this reason, the TA and optical signal provides as a convenient reference for the bolometer sensitivity where any changes in the signals would indicate a change in the bolometer sensitivity. The TA and optical signals were analysed, also by means of integrating at the rising edge of the signal, for all biases, and is shown in Figure 6.9.

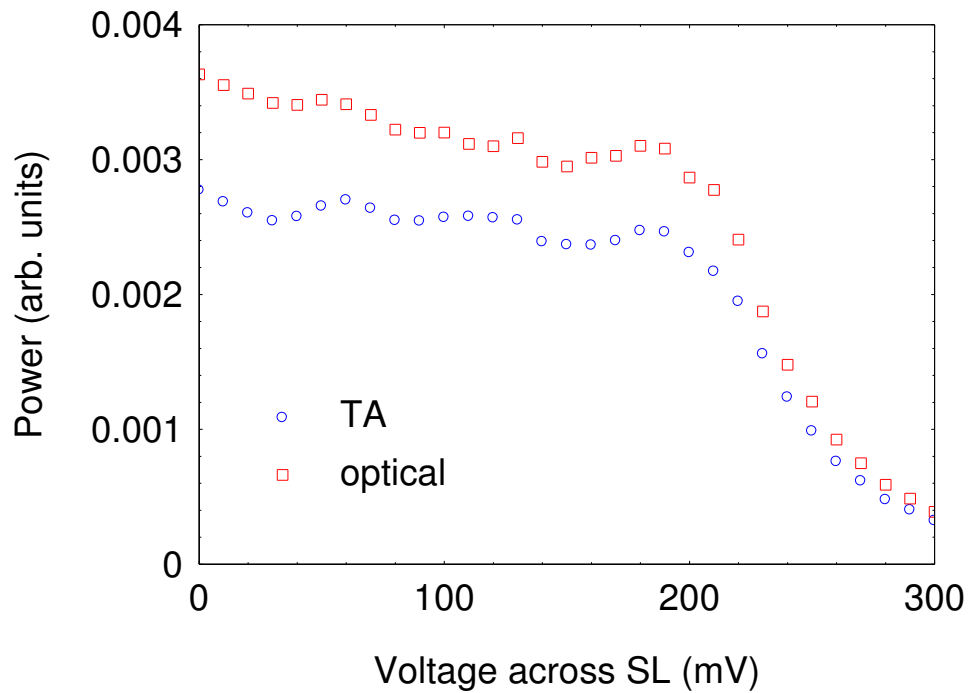


Figure 6.9: The optical (luminescence) and TA phonon power as a function of voltage dropped across the gain SL. The TA phonon power is following the trend of the optical power and the shape indicates the change in bolometer sensitivity as a function of the bias.

The TA and optical signal, in Figure 6.9, eventually decreases in power at higher biases as the bolometer approaches saturation. The fall of the detected LA phonon power at higher biases seems to follow the same trend of the change in the TA and optical power above 200 mV. However, most importantly, the graph showed no indication of rise in the optical or the TA phonon power, with respect to bias, in the range where the peak in the LA phonon power was observed. This provided additional clarification that the increase in the LA phonon power, between 165 mV and 200 mV, was not associated to changes in the bolometer sensitivity.

### 6.3 Injection Seeding in a Low Q Cavity – Case Study of the MN 685 SASER Device

The effect of seeding phonons in a low Q cavity was studied using the MN 685 SASER device where the frequency of the injected modes coincides with a relatively high loss inside the cavity. The injected modes with a frequency of 640 GHz were generated by tuning the wavelength of the laser close to the optical resonance of the high reflector SL. This was determined by PL measurements performed in Chapter 4 where the resonance centred at  $718 \pm 5$  nm. The scheme of operation is as described by Figure 6.1, where the range of excitation wavelengths was between 710 nm and 720 nm. The division ratio for the pulse picker was set to 1000, providing a delay between each laser pulse by 12.5  $\mu$ s long. The bolometric response at each applied bias, between 0 mV and 300 mV, was recorded and analysed.

#### 6.3.1 Results from the MN 685 device

Figure 6.10 shows the result obtained for an excitation wavelength of 712 nm at an applied bias of 130 mV. The zero time indicates the arrival of the optical pulse followed by the LA and TA phonons corresponding to flight times of 81 ns and 105 ns respectively, as labelled in the figure. The most intriguing feature is the ratio of heights between the LA and TA signals. In this SASER device, the ratio is much larger than that shown in Figure 6.5; indicating a greater increase in the LA phonon power. Owing to the different doping profile of the gain SL in this sample, more electrons, or current, are flowing through the gain SL which may result into



additional stimulated emission processes and hence provide much greater increase in the LA phonon population.

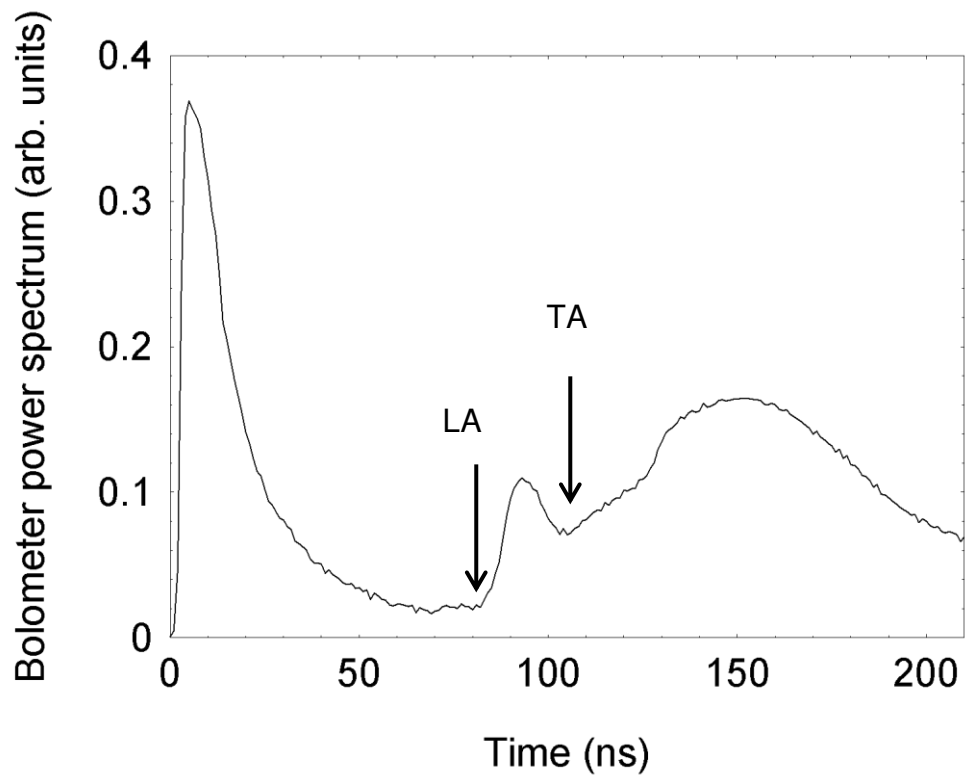


Figure 6.10: The different components of the heat pulse arriving at the bolometer where the zero time indicates the arrival of the optical pulse, followed by the arrival of the LA phonons 81 ns later. The TA phonons then appear at 105 ns after the arrival of the optical pulse.

The integrated LA phonon signal is shown in Figure 6.11 for a range of applied biases (= the voltage dropped across the SL). Results for five different excitation wavelengths were compared.

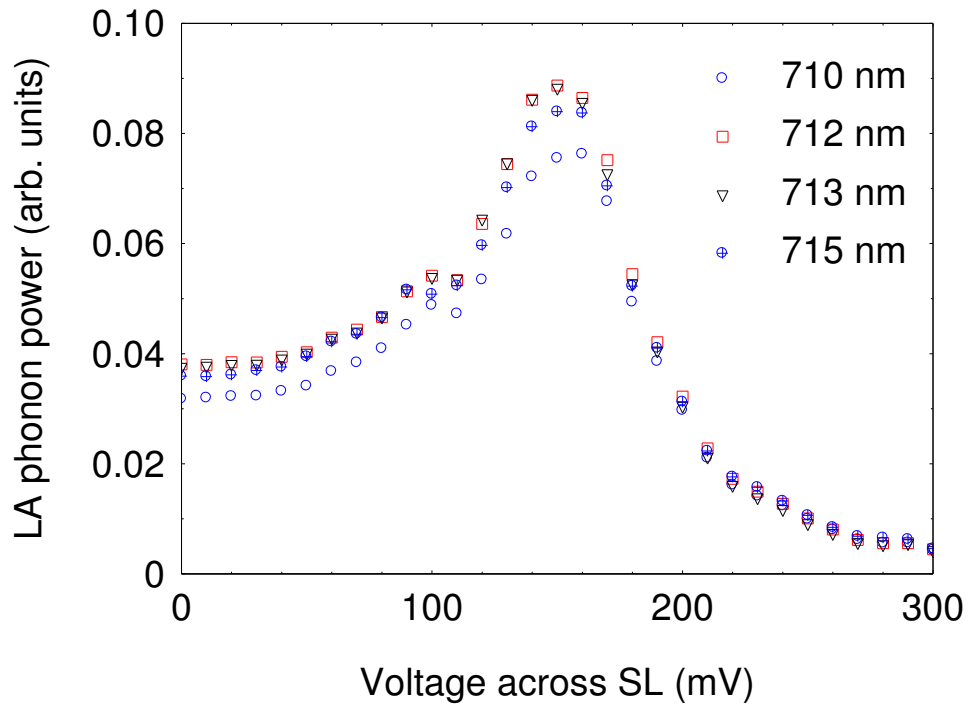


Figure 6.11: The LA phonon power for five different excitation wavelengths, as indicated by the legends, plotted as a function of the voltage across the SL. Maximum phonon power was obtained for excitation wavelengths of 712 nm and 713 nm, as the power starts to rise from 110 mV and peaks at 155 mV.

The peak in the LA phonon power occurs from 110 mV, corresponding to a Stark splitting energy of 2.2 meV. The frequency of the phonon modes in resonance with this Stark energy is  $\sim 532$  GHz. However, theoretically, the laser light generates the zone-centre phonon modes which correspond to the 646 GHz phonon modes, as shown in Chapter 4. This means that a rise in phonon power is expected from 130 mV. The discrepancy in the values may be due to an overlap of the 150 mV peak and the 100 mV weak peak. This weak peak may arise due to the presence of disorder in the SL, leading to the generation of other cavity modes, at the stop band, that may be amplified slightly. Furthermore, there may be some small voltage dropped across the contacts which has not been taken into account. Nevertheless, the LA phonon power peaks at 150

mV which corresponds to a higher Stark splitting energy than the 646 GHz phonon mode energy, as expected. Therefore, this peak may be attributed to the amplification of the 646 GHz phonon modes.

### 6.3.2 The optical (luminescence) and TA phonon power

As the TA phonons and the luminescence provide a measure of the bolometer sensitivity, both signals were analysed across a range of biases and excitation wavelengths for the MN 685 SASER device. Figure 6.12 shows the optical and TA phonon power at the excitation wavelength of 712 nm.

The TA phonons followed the pattern of the optical power detected by the bolometer. This is mostly dependent on the effect of the increase in background heat from the device. The large power attained by the TA phonons from zero bias is attributed to the large luminescence provided by the laser excitation. Also, both showed a decrease in power from 160 mV onwards as the bolometer approaches saturation. Crucially enough, in the range where a rise in the LA phonon power was observed, neither the TA phonons nor the luminescence showed any increase in signal. This implies that the rise in the LA phonon power was not due to any increase in the dissipated heat across the device as well as to any changes in the bolometer sensitivity.

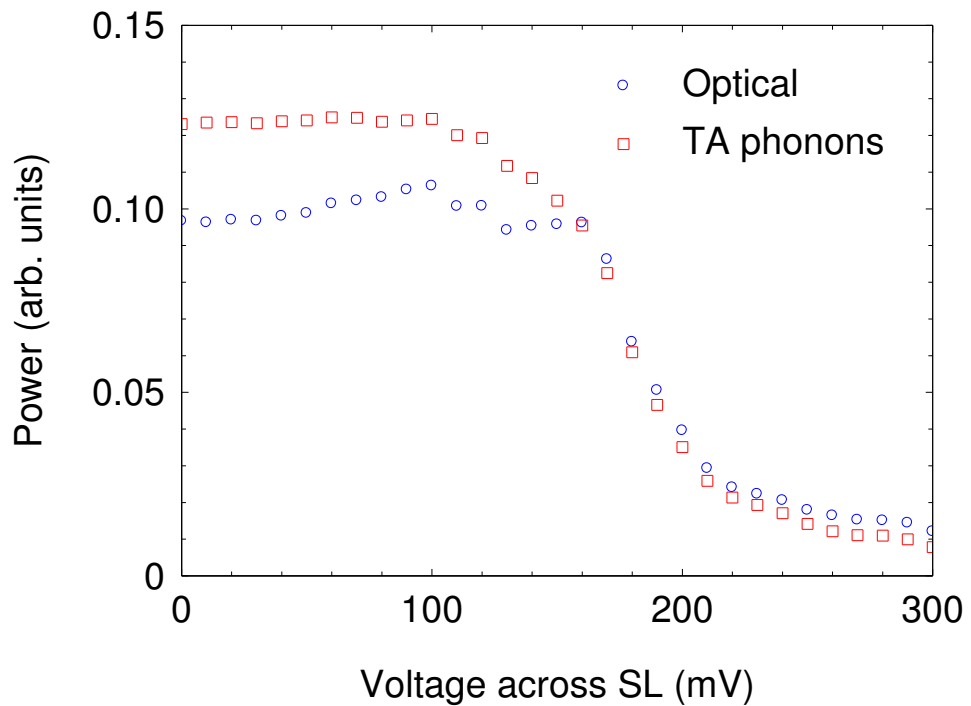


Figure 6.12: The optical and TA phonon power obtained as a function of the voltage across the SL. By 160 mV the power for both components fall at the same rate, indicating a change in bolometer sensitivity due to a larger background heat.

Above 160 mV however, the bolometer is approaching saturation point and will no longer accurately measure the changes in power of the LA phonon signal.

#### 6.4 Overall conclusion

The results of the current experiment performed on both SASER devices yields analogous characteristics of a seeded laser. Among these is the broadening of the LA phonon power observed in sample NU 2694 when the cavity was seeded with extra phonons at the frequency of the oscillating cavity modes. The peak is associated to the amplification of the generated mode when the gain starts to

decrease. An increase in LA phonon power was also observed when additional phonons, generated by the laser excitation of the mirror SL, are injected into a low Q cavity. This was investigated in the MN 685 SASER device whereby phonon amplification was observed when the injected phonon frequency was different to that of the oscillating cavity modes. The MN 685 SASER device in this case was considered as a phonon amplifier for the seeded modes. The observation of phonon amplification at a different frequency in the MN 685 SASER device, as presented in this chapter, provides added advantage and feasibility in the usage of SASER devices across a wide range of electronic applications.

# CHAPTER 7

## CONCLUSIONS AND FUTURE WORK

This chapter provides a summary of conclusions of the current work relating to the feasibility of an electrically pumped THz SASER device using SLs. Potential applications including suggestions on techniques of measuring the coherence of this SASER device will be discussed in Section 7.2.

### 7.1 Conclusions

Overall, the investigations of the proposed THz SASER device have led to significant progress in understanding fundamental principles of SASER oscillations. Optimisation of SL SASERs in this work has led to the invention of the 325 GHz vertical-cavity SASER device. By comparing with the 650 GHz SASER device, only the former exhibited phonon oscillation build up.

Optical characterisation of the cavity yields a high Q cavity suitable for sustaining phonon oscillations and extracting the SASER output. Two sets of measurements were conducted to determine the possibilities of achieving such a SASER device and to observe a potential application of the SASER device by seeding phonons at a particular frequency into the cavity. Conclusions of each work will be presented by recalling the important discussions from previous chapters.

### 7.1.1 THz SASER Oscillations:

Two SASER devices with different operating frequencies were investigated as a possible source of sub-THz acoustic radiation. One device was working at 650 GHz with donor concentration of  $2 \times 10^{16} \text{ cm}^{-3}$  in the gain medium SL and the latter at 325 GHz with ten times higher carrier concentrations.

Phonons inside the cavities would build up from spontaneous emission 'phonon noise'. Spontaneous emission depletes the inversion and reduces the gain. Hence, fabricating a SASER device at half the original frequency (650 GHz) would reduce the ratio of Einstein's A and B coefficients by a factor of eight. A much faster rate of phonon build up increases the possibility of observing sustainable SASER oscillations, to provide contrast to 'trivial' build-ups of the bolometer signal due to instrumental factors.

Build-up of phonon oscillations, towards steady state intensity, was indeed observed in a SASER device operating at 325 GHz. By fitting a theoretical expression for the build-up curve to the data, it was possible to determine other attributes of the SASER device. For a range of pump amplitudes, the gain of the SASER device,  $\gamma_0$ , was deduced as  $376 \pm 43 \text{ cm}^{-1}$  with a maximum output power of  $680 \pm 80 \text{ Wm}^{-2}$  and a maximum efficiency of 10 %. Furthermore, an indication of a highly directional SASER beam was discovered by measuring the phonon intensity emitted at an angle of  $57^\circ$  from the device axis.

### 7.1.2 Injection Seeding

Injection locking has been demonstrated in a single trapped ion 'phonon laser' operating at MHz frequencies [21]. By injecting

phonons at a specific frequency into the SASER devices, it is possible to observe injection locking of the seeded mode in the sub-THz regime. Injection seeding in two cases was presented where the seeded phonons were generated by laser excitation.

In the first case, phonons with frequencies of the oscillating cavity modes were injected into the cavity of a 650 GHz SASER device. Under steady state conditions, no increase in the phonon power is expected. However, a peak in the LA phonon power was observed at Stark splitting energies above the range corresponding to the threshold gain for SASER oscillations. Under these conditions, the gain is too small compared to the cavity losses to sustain oscillations, but will still act to amplify the seeded phonon modes.

In the second case, a 325 GHz SASER device was seeded with phonons having a different frequency to that of the oscillating cavity modes to observe the effect of injection seeding in a low Q cavity. Although no SASER oscillations are predicted to occur at the seeded frequency, as the cavity losses were high, an increase in phonon power was detected. The rise in LA phonon power was observed when the energy of the seeded mode matched the Stark splitting energy. In Chapter 4, optical characterisation of this SASER device showed that laser-generated modes completed one round trip, which would correspond to a lifetime of 600 ps. Hence, the increase of LA phonon flux may correspond to one round trip of the seeded modes passing through the gain medium.



## 7.2 Future Work

### 7.2.1 SASER Device as a Driving Source for Electromagnetic (EM) Radiation

In the beginning of this thesis, emphasis was placed on the technological interest of THz devices. A potential application is to use a THz SASER device as a driving source for EM radiation. Authors of [97] observed self-sustained oscillations of current in a doped GaAs/AlAs SL under vertical electron transport. Frequencies up to 20 MHz were detected, attributed to Negative Differential Conductance (NDC) occurring in the SL. In [98], microwave radiation at a fundamental frequency of 6 GHz was observed in a wide miniband GaAs/AlAs SL, owing to the space charge instabilities due to Bragg reflections of electrons in a SL miniband.

Preliminary studies on the 650 GHz SASER device revealed 5.3 GHz of EM radiation, electromagnetically coupled resonantly with an external circuit, when the device is operating in the region of NDC. The generation mechanism was ascribed to the field domains propagating through several periods of the SL; a motion of the domain (space charge) boundary over several SL periods, as previously mentioned in [97].

Recently, generation of THz EM radiation in a SL driven by an acoustic wave was theoretically predicted [99]. As the SASER device operates at narrow bandwidths (almost all the LA phonons are of the same mode), due to the fundamental amplification mechanism, it is possible, with all the properties mentioned above, for a SASER device to be as an EM driver and as a reliable signal analyser for acoustic and EM radiation.

## 7.2.2 Coherent Detection of Acoustic Emission

Current work presented throughout this thesis involved the use of a bolometer as a phonon detector. This is an incoherent phonon detection technique. Evidence of coherence via simulated emission was therefore indirect in this case. Hence, an obvious future work may be in determining the coherence of the acoustic beam coupling out of the SASER devices described in this thesis and to further confirm that amplification in this case is through stimulated emission.

A possible technique, that has shown to provide high signal to noise ratio, is a correlation technique as used to analyse light beams [100, 101]. By incorporating this technique with an optically gated phonon detector based on a *p-i-n* diode [102, 103], it is possible to measure the coherence of the phonon modes arriving at the *p-i-n* diode. Equal intensities of the laser light may be focused onto the *p-i-n* device, where one of the beams was set at a particular time delay. A schematic diagram of the experimental configuration is shown in Figure 7.1.

Both beams provide photo excited carriers in the *p-i-n* device, creating a stationary current level in the intrinsic region. As high frequency phonons passes through the device a change in the photocurrent is measured. The change in photocurrent arises from the strain-induced shift of the excitonic resonance in the quantum well, situated in the intrinsic region of the *p-i-n* device, due to deformation potential electron-phonon coupling [103]. If the phonons passing through the *p-i-n* device are coherent, then the measured change in photocurrent would show an oscillatory behaviour as the phonons propagate through the device.

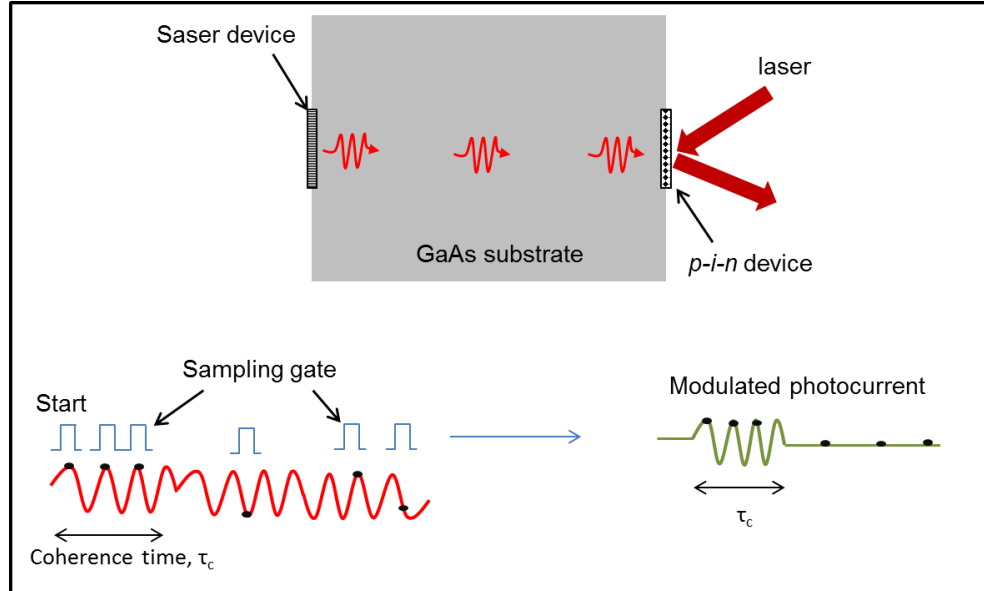


Figure 7.1: Experimental scheme of a correlation technique using a p-i-n diode as an optically gated detector.

### 7.2.3 Improvements on SASER Gain Medium

Other than the change of doping explored in this thesis, no modification to the gain medium has been made in all previous works pertaining to the SL SASER. However as pointed out in the conclusions section, the SASER device with the higher doping concentration gain medium, showed a clear build-up effect of the phonon oscillations; suggesting an improved SASER device. Other possible improvements to the gain medium may include changes to the SL parameters to achieve a wider region of the Wannier Stark ladder of states. By increasing the widths of the wells and/or barriers, the tunnelling of electrons giving rise to the miniband may be

reduced. Hence, vertical electron transport via hopping conduction may commence from a much lower bias.

The influence of disorder in improving SASER action is described in [38]. The authors postulated possibilities of a robust SASER device for a broad range of Stark splitting energies due to the presence of disorder. A redistribution of electrons among the quantum wells of the SL may provide mismatch of quasi-Fermi energies that reduces the population of the final states. This provides a larger quantity of empty states for phonon-assisted tunnelling and hence enhances the population inversion for some pairs of quantum wells. Furthermore, slight shifts in the Stark splitting energy, by the electrostatic fields due to the non-uniform electron distribution, may also increase the average total phonon increment. Hence, by deliberately creating a degree of disorder in the gain medium SL, a more enhanced SASER device may be created. This may be achieved either by gradiently increasing the carrier concentration in the gain medium SL and/or by varying the thickness of the SL layers.

#### 7.2.4 Silicon Based SLs as Potential SASER Devices

Theoretical and experimental evidence of phononic bandgap and folded acoustic phonons in porous silicon was reported by [104, 105], providing a new perspective in terms of using silicon for a SASER device other than GaAs and AlAs SLs. Even more favourable is the widespread of Si technology and the compatibility of Si-based devices with modern microelectronic devices [106].

The porous Silicon SL structure forms an acoustic Bragg mirror which reflects phonons at the stop bands and therefore has similar acoustic properties to the SL mirrors in the current SASER device. Preliminary pump probe experiments conducted on porous Silicon

SLs revealed frequency at the stop band of the associated dispersion curve. However, this evidence needs clarification and further investigations are needed to understand the underlying mechanisms in detecting phonons in porous Silicon SLs and other effects that may need to be accounted for in porous structures. For example, if a large portion of the laser light used in pump-probe reflectivity measurements is absorbed in a sample with modulated porosity then pump-probe reflectivity measurements on the sample may be difficult.

## References

1. Hamaguchi, C., *Basic semiconductor physics*. 2010: Springer Berlin Heidelberg.
2. Hook, J.R. and H.E. Hall, *Solid state physics*. 1991: Wiley.
3. Bardeen, J. and W. Shockley, *Deformation Potentials and Mobilities in Non-Polar Crystals*. *Physical Review*, 1950. **80**(1): p. 72-80.
4. Glavin, B.A., V.A. Kochelap, and T.L. Linnik, *Generation of high-frequency coherent acoustic phonons in a weakly coupled superlattice*. *Applied Physics Letters*, 1999. **74**(23): p. 3525-3527.
5. Daly, B.C. and T.B. Norris, *Ultrafast acoustics for imaging at the nanoscale*. *Journal of Physics: Conference Series*, 2007. **92**(1): p. 012094.
6. Armstrong, M.R., et al., *Observation of terahertz radiation coherently generated by acoustic waves*. *Nat Phys*, 2009. **5**(4): p. 285-288.
7. Ferguson, B. and X.-C. Zhang, *Materials for terahertz science and technology*. *Nat Mater*, 2002. **1**(1): p. 26-33.
8. Beard, M.C., G.M. Turner, and C.A. Schmuttenmaer, *Terahertz Spectroscopy*. *The Journal of Physical Chemistry B*, 2002. **106**(29): p. 7146-7159.
9. Wai Lam, C., D. Jason, and M.M. Daniel, *Imaging with terahertz radiation*. *Reports on Progress in Physics*, 2007. **70**(8): p. 1325.
10. Kim, K.Y., et al., *Measurements of Terahertz Electrical Conductivity of Intense Laser-Heated Dense Aluminum Plasmas*. *Physical Review Letters*, 2008. **100**(13): p. 135002.
11. Maiman, T.H., *Stimulated Optical Radiation in Ruby*. *Nature*, 1960. **187**(4736): p. 493-494.

12. Tucker, E.B., *Amplification of 9.3-kMc/sec Ultrasonic Pulses by Maser Action in Ruby*. Physical Review Letters, 1961. **6**(10): p. 547-548.
13. Tucker, E.B., *Attenuation of Longitudinal Ultrasonic Vibrations by Spin-Phonon Coupling in Ruby*. Physical Review Letters, 1961. **6**(4): p. 183-185.
14. Kikuchi, C., et al., *Ruby as a Maser Material*. Journal of Applied Physics, 1959. **30**(7): p. 1061-1067.
15. Tilstra, L.G., A.F.M. Arts, and H.W. de Wijn, *Coherence of phonon avalanches in ruby*. Physical Review B, 2003. **68**(14): p. 144302.
16. Tilstra, L.G., A.F.M. Arts, and H.W.d. Wijn, *SASER action in optically excited ruby: Angular and spectral distribution*. Journal of Physics: Conference Series, 2007. **92**(1): p. 012011.
17. Bron, W.E. and W. Grill, *Stimulated Phonon Emission*. Physical Review Letters, 1978. **40**(22): p. 1459-1463.
18. Prieur, J.Y., et al., *Sound amplification by stimulated emission of phonons using two-level systems in glasses*. Physica B: Condensed Matter, 1996. **219–220**(0): p. 235-238.
19. Zhu, T.C., H.J. Maris, and J. Tauc, *Attenuation of longitudinal-acoustic phonons in amorphous SiO<sub>2</sub> at frequencies up to 440 GHz*. Physical Review B, 1991. **44**(9): p. 4281-4289.
20. Vahala, K., et al., *A phonon laser*. Nat Phys, 2009. **5**(9): p. 682-686.
21. Knünz, S., et al., *Injection Locking of a Trapped-Ion Phonon Laser*. Physical Review Letters, 2010. **105**(1): p. 013004.
22. Grudin, I.S., et al., *Phonon Laser Action in a Tunable Two-Level System*. Physical Review Letters, 2010. **104**(8): p. 083901.
23. Cho, A.Y. and J.R. Arthur, *Molecular beam epitaxy*. Progress in Solid State Chemistry, 1975. **10**, Part 3(0): p. 157-191.

24. Makler, S.S., et al., *Ultra-high-frequency coherent sound generation in resonant tunneling*. Surface Science, 1996. **361–362**(0): p. 239-242.
25. Camps, I., et al., *GaAs-Al<sub>x</sub>Ga<sub>1-x</sub>As double-barrier heterostructure phonon laser: A full quantum treatment*. Physical Review B, 2001. **64**(12): p. 125311.
26. Sergio, S.M., et al., *A source of terahertz coherent phonons*. Journal of Physics: Condensed Matter, 1998. **10**(26): p. 5905.
27. Camps, I. and S.S. Makler, *The operation threshold of a double barrier phonon laser*. Solid State Communications, 2000. **116**(4): p. 191-196.
28. Giltrow, M., et al., *Observation of Plasmon-Optic Phonon Coupled Modes in GaAs/AlGaAs Resonant Tunneling Structures via Acoustic Phonon Decay Products*. Physical Review Letters, 1995. **75**(9): p. 1827-1830.
29. Komirenko, S.M., et al., *Generation and amplification of sub-THz coherent acoustic phonons under the drift of two-dimensional electrons*. Physical Review B, 2000. **62**(11): p. 7459-7469.
30. Mensah, S.Y., et al., *Amplification of acoustic phonons in a degenerate semiconductor superlattice*. Physica E: Low-dimensional Systems and Nanostructures, 2003. **19**(3): p. 257-262.
31. Glavin, B.A., et al., *Generation of high-frequency coherent acoustic phonons in superlattices under hopping transport. II. Steady-state phonon population and electric current in generation regime*. Physical Review B, 2002. **65**(8): p. 085304.
32. Glavin, B.A., et al., *Generation of high-frequency coherent acoustic phonons in superlattices under hopping transport. I. Linear theory of phonon instability*. Physical Review B, 2002. **65**(8): p. 085303.
33. Esaki, L. and R. Tsu, *Superlattice and Negative Differential Conductivity in Semiconductors*. IBM Journal of Research and Development, 1970. **14**(1): p. 61-65.

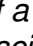


34. Tamura, S., D.C. Hurley, and J.P. Wolfe, *Acoustic-phonon propagation in superlattices*. Physical Review B, 1988. **38**(2): p. 1427-1449.
35. Tsu, R. and G. Döhler, *Hopping conduction in a "superlattice"*. Physical Review B, 1975. **12**(2): p. 680-686.
36. Kent, A.J., et al., *Acoustic Phonon Emission from a Weakly Coupled Superlattice under Vertical Electron Transport: Observation of Phonon Resonance*. Physical Review Letters, 2006. **96**(21): p. 215504.
37. Beardsley, R.P., et al., *Coherent Terahertz Sound Amplification and Spectral Line Narrowing in a Stark Ladder Superlattice*. Physical Review Letters, 2010. **104**(8): p. 085501.
38. Beardsley, R.P., et al., *A GaAs/AlAs superlattice as an electrically pumped THz acoustic phonon amplifier*. New Journal of Physics, 2011. **13**(7): p. 073007.
39. Kent, A.J., et al., *Generation and propagation of monochromatic acoustic phonons in gallium arsenide*. Applied Physics Letters, 2002. **81**(18): p. 3497-3499.
40. Fainstein, A., et al., *Strong Optical-Mechanical Coupling in a Vertical GaAs/AlAs Microcavity for Subterahertz Phonons and Near-Infrared Light*. Physical Review Letters, 2013. **110**(3): p. 037403.
41. Huynh, A., et al., *Subterahertz Phonon Dynamics in Acoustic Nanocavities*. Physical Review Letters, 2006. **97**(11): p. 115502.
42. Siegman, A.E., *Lasers*. 1986: University Science Books.
43. Pascual Winter, M.F., et al., *Selective Optical Generation of Coherent Acoustic Nanocavity Modes*. Physical Review Letters, 2007. **98**(26): p. 265501.
44. Rozas, G., et al., *Lifetime of THz Acoustic Nanocavity Modes*. Physical Review Letters, 2009. **102**(1): p. 015502.

45. Trigo, M., et al., *Confinement of Acoustical Vibrations in a Semiconductor Planar Phonon Cavity*. Physical Review Letters, 2002. **89**(22): p. 227402.
46. Colvard, C., et al., *Observation of Folded Acoustic Phonons in a Semiconductor Superlattice*. Physical Review Letters, 1980. **45**(4): p. 298-301.
47. Rytov, S., *Acoustical properties of a thinly laminated medium*. Soviet Physics Acoustics, 1956. **2**: p. 68-80.
48. Hooker, S. and C. Webb, *Laser Physics*. 2010: OUP Oxford.
49. Wolfe, J.P., *Imaging Phonons: Acoustic Wave Propagation in Solids*. 2005: Cambridge University Press.
50. K. J. R. Rosman and P.D.P. Taylor, *Naturally occurring isotope abundances: Commission on Atomic Weights and Isotopic Abundances report for the International Union of Pure and Applied Chemistry in Isotopic Compositions of the Elements 1989*. Pure and Applied Chemistry, 1998. **70**(217).
51. Tamura, S.-i., *Isotope scattering of large-wave-vector phonons in GaAs and InSb: Deformation-dipole and overlap-shell models*. Physical Review B, 1984. **30**(2): p. 849-854.
52. Adachi, S., *GaAs and Related Materials: Bulk Semiconducting and Superlattice Properties*. 1994: World Scientific.
53. Steigmeier, E.F. and B. Abeles, *Scattering of Phonons by Electrons in Germanium-Silicon Alloys*. Physical Review, 1964. **136**(4A): p. A1149-A1155.
54. Ziman, J.M., *XVII. The effect of free electrons on lattice conduction*. Philosophical Magazine, 1956. **1**(2): p. 191-198.
55. Ziman, J.M., *The effect of free electrons on lattice conduction*. Philosophical Magazine, 1957. **2**(14): p. 292-292.
56. Cardona, M. and N.E. Christensen, *Acoustic deformation potentials and heterostructure band offsets in semiconductors*. Physical Review B, 1987. **35**(12): p. 6182-6194.

57. Shinde, S.L. and J. Goela, *High Thermal Conductivity Materials*. 2005: Springer.
58. Klemens, P.G., *Decay of High-Frequency Longitudinal Phonons*. Journal of Applied Physics, 1967. **38**(12): p. 4573-4576.
59. Herring, C., *Role of Low-Energy Phonons in Thermal Conduction*. Physical Review, 1954. **95**(4): p. 954-965.
60. Tamura, S.-i., *Spontaneous decay rates of LA phonons in quasi-isotropic solids*. Physical Review B, 1985. **31**(4): p. 2574-2577.
61. Sakaki, H., et al., *Interface roughness scattering in GaAs/AlAs quantum wells*. Applied Physics Letters, 1987. **51**(23): p. 1934-1936.
62. Ruf, T., et al., *Interface roughness and homogeneous linewidths in quantum wells and superlattices studied by resonant acoustic-phonon Raman scattering*. Physical Review B, 1994. **50**(3): p. 1792-1806.
63. Jusserand, B., et al., *Raman scattering characterization of interface broadening in GaAs/AlAs short period superlattices grown by molecular beam epitaxy*. Applied Physics Letters, 1985. **47**(3): p. 301-303.
64. Jusserand, B., et al., *Atomic-scale roughness of GaAs/AlAs interfaces: A Raman scattering study of asymmetrical short-period superlattices*. Applied Physics Letters, 1990. **57**(6): p. 560-562.
65. Milonni, P.W. and J.H. Eberly, *Laser Physics*. 2010: John Wiley & Sons.
66. Joyce, B.A., *Molecular beam epitaxy*. Reports on Progress in Physics, 1985. **48**(12): p. 1637.
67. Rong, Z., et al., *A Comparison of the Selective Etching Characteristics of Conventional and Low-Temperature-Grown GaAs over AlAs by Various Etching Solutions*. Japanese Journal of Applied Physics, 1996. **35**(part 1, No. 1A): p. 3.

68. Tsu, R. and L. Esaki, *Tunneling in a finite superlattice*. Applied Physics Letters, 1973. **22**(11): p. 562-564.
69. Mishina, T., et al., *Real time-space dynamics of zone-folded phonons in GaAsAlAs superlattices*. Solid State Communications, 1998. **107**(6): p. 281-284.
70. Lanzillotti-Kimura, N.D., et al., *Coherent Generation of Acoustic Phonons in an Optical Microcavity*. Physical Review Letters, 2007. **99**(21): p. 217405.
71. Beardsley, R.P., et al., *Coherent phonons in a doped GaAs/AlAs superlattice*. Journal of Physics: Conference Series, 2007. **92**(1): p. 012014.
72. Shapiro, S.L. and D.H. Auston, *Ultrashort light pulses: picosecond techniques and applications*. 1984: Springer-Verlag.
73. Eisenmenger, W., et al., *Intrinsic and experimental quasiparticle recombination times in superconducting films*. Applied physics, 1977. **12**(2): p. 163-171.
74. Voliotis, V., et al., *Absorption coefficient in type-II GaAs/AlAs short-period superlattices*. Physical Review B, 1994. **49**(4): p. 2576-2584.
75. Dingle, R. and J.K.F. Rodgers, *RADIATIVE LIFETIMES IN n-TYPE GALLIUM ARSENIDE*. Applied Physics Letters, 1969. **14**(6): p. 183-184.
76. Rossi, J.A., C.M. Wolfe, and J.O. Dimmock, *Acceptor Luminescence in High-Purity n-Type GaAs*. Physical Review Letters, 1970. **25**(23): p. 1614-1617.
77. Bartels, A., et al., *Coherent Zone-Folded Longitudinal Acoustic Phonons in Semiconductor Superlattices: Excitation and Detection*. Physical Review Letters, 1999. **82**(5): p. 1044-1047.
78. Yamamoto, A., et al., *Coherent Oscillation of Zone-Folded Phonon Modes in GaAs-AlAs Superlattices*. Physical Review Letters, 1994. **73**(5): p. 740-743.

79. Pascual-Winter, M.F., et al., *Spectral responses of phonon optical generation and detection in superlattices*. Physical Review B, 2012. **85**(23): p. 235443.
80. Bruchhausen, A., et al., *Investigation of coherent acoustic phonons in terahertz quantum cascade laser structures using femtosecond pump-probe spectroscopy*. Journal of Applied Physics, 2012. **112**(3): p. 033517-8.
81. Beardsley, R., et al., *Optical detection of folded mini-zone-edge coherent acoustic modes in a doped GaAs/AlAs superlattice*. Physical Review B, 2010. **82**(4): p. 041302.
82. Grahn, H.T., *Semiconductor Superlattices: Growth and Electronic Properties*. 1995: World Scientific.
83. Beardsley, R., *Coherent Phonon Processes in Semiconductor Superlattices*. 2011.
84. Bugg, D.V., *Electronics: Circuits, Amplifiers and Gates, Second Edition*. 2010: Taylor & Francis.
85. Hess, K. and J.D. Dow, *Deformation potentials of bulk semiconductors*. Solid State Communications, 1981. **40**(4): p. 371-373.
86. Weaver, L.A., I. Liberman, and C.H. Church, *Changes in Sidelight Fluorescence in Nd:Cr:YAG due to Lasering at 1.06  $\mu$* . Journal of Applied Physics, 1967. **38**(13): p. 5405-5406.
87. Park, Y.K., G. Giuliani, and R.L. Byer, *Stable single-axial-mode operation of an unstable-resonator Nd:YAG oscillator by injection locking*. Opt. Lett., 1980. **5**(3): p. 96-98.
88. Park, Y., G. Giuliani, and R. Byer, *Single axial mode operation of a -switched Nd:YAG oscillator by injection seeding*. Quantum Electronics, IEEE Journal of, 1984. **20**(2): p. 117-125.
89. Bondarenko A. N., F.K.G., Smirnov V. A., Antsiferov V. V. , *Generation Induced in a Q-switched Ruby Laser by an External Signal*. JETP Letters, 1967. **6**(6): p. 178-180.

90. Bruesselbach, H.W., et al., *Low-heat high-power scaling using InGaAs-diode-pumped Yb:YAG lasers*. Selected Topics in Quantum Electronics, IEEE Journal of, 1997. **3**(1): p. 105-116.
91. Barnes, N.P. and J.C. Barnes, *Injection seeding. I. Theory*. Quantum Electronics, IEEE Journal of, 1993. **29**(10): p. 2670-2683.
92. Cassard, P. and J.M. Lourtioz, *Injection locking of high-power pulsed lasers. I. Monochromatic injection*. Quantum Electronics, IEEE Journal of, 1988. **24**(11): p. 2321-2337.
93. Robert W. Byren, R.A.R., *MULTI-MODE LASER OSCILLATOR WITH LARGE INTERMODE SPACING*. 1999, Raytheon Company.
94. Langbein, W., H. Kalt, and J.M. Hvam, *Luminescence dynamics in type-II GaAs/AlAs superlattices near the type-I to type-II crossover*. Physical Review B, 1996. **54**(20): p. 14589-14594.
95. Merlin, R., *Generating coherent THz phonons with light pulses*. Solid State Communications, 1997. **102**(2-3): p. 207-220.
96. Challis, L.J., *Electron-Phonon Interaction in Low-Dimensional Structures*. 2003: Oxford University Press.
97. Kastrup, J., et al., *Self-oscillations of domains in doped GaAs-AlAs superlattices*. Physical Review B, 1995. **52**(19): p. 13761-13764.
98. Hofbeck, K., et al., *High-frequency self-sustained current oscillation in an Esaki-Tsu superlattice monitored via microwave emission*. Physics Letters A, 1996. **218**(3-6): p. 349-353.
99. Greenaway, M.T., et al., *Using acoustic waves to induce high-frequency current oscillations in superlattices*. Physical Review B, 2010. **81**(23): p. 235313.
100. Brown, R.H. and R.Q. Twiss, *Correlation between Photons in two Coherent Beams of Light*. Nature, 1956. **177**(4497): p. 27-29.

101. Brown, R.H. and R.Q. Twiss, *Interferometry of the Intensity Fluctuations in Light. I. Basic Theory: The Correlation between Photons in Coherent Beams of Radiation*. Proceedings of the Royal Society of London. Series A. Mathematical and Physical Sciences, 1957. **242**(1230): p. 300-324.
102. Moss, D., et al., *Ultrafast acoustical gating of the photocurrent in a p-i-n tunneling diode incorporating a quantum well*. Physical Review B, 2009. **80**(11): p. 113306.
103. Moss, D., et al., *Picosecond strain pulses probed by the photocurrent in semiconductor devices with quantum wells*. Physical Review B, 2011. **83**(24): p. 245303.
104. Reinhardt, A. and P.A. Snow, *Theoretical study of acoustic band-gap structures made of porous silicon*. physica status solidi (a), 2007. **204**(5): p. 1528-1535.
105. Thomas, L., G.N. Aliev, and P.A. Snow, *Hypersonic rugate filters based on porous silicon*. Applied Physics Letters, 2010. **97**(17): p. 173503-3.
106. Hirschman, K.D., et al., *Silicon-based visible light-emitting devices integrated into microelectronic circuits*. Nature, 1996. **384**(6607): p. 338-341.